

AN ANALYTIC MODEL OF ENVIRONMENTAL EFFECTS
ON COSMIC STRUCTURE FORMATION
AND AN APPLICATION TO COSMIC ACCRETION SHOCKS

BY

VASILIKI PAVLIDOU

B.S., Aristotle University of Thesaloniki, 1999
M.S., University of Illinois at Urbana-Champaign, 2001

DISSERTATION

Submitted in partial fulfillment of the requirements
for the degree of Doctor of Philosophy in Astronomy
in the Graduate College of the
University of Illinois at Urbana-Champaign, 2005

Urbana, Illinois

AN ANALYTIC MODEL OF ENVIRONMENTAL EFFECTS
ON COSMIC STRUCTURE FORMATION
AND AN APPLICATION TO COSMIC ACCRETION SHOCKS

Vasiliki Pavlidou, Ph.D.

Department of Astronomy

University of Illinois at Urbana-Champaign, 2005

Brian D. Fields, Advisor

We present a new analytic tool for the study of cosmic structure formation, a *double distribution* of the number density of dark matter halos with respect to both halo mass and local over- (or under-) density. The double distribution provides a statistical treatment of the properties of matter *surrounding* collapsed objects, and can be used to provide analytical insight into environmental effects on hierarchical structure formation.

We apply this new tool to the case of cosmic accretion shocks. We investigate and quantify the effect of environmental factors on the statistical properties of these shocks. For this purpose, we explore two different models. The first “control” model uses a Press-Schechter mass function to describe the population of collapsed structures, and assumes that all objects accrete gas of the same density and temperature. The second model treats the accreted material as a multi-temperature, multi-density medium with densities and temperatures derived from the double distribution. We find that the shock environment significantly alters the physical impact of cosmic accretion shocks on the intergalactic medium, as well as the cosmic history of their properties.

Acknowledgements

I thank my advisor, Brian Fields, for his guidance and support throughout my graduate studies, and especially during the necessary, long, and not visibly productive period of development of the analytical tools used in this work. I thank the members of my doctoral committee, Icko Iben, Telemachos Mouschovias, Laird Thompson, and Ben Wandelt, for all their help and continued interest in my work.

I gratefully acknowledge enlightening scientific discussions which enhanced the content of this dissertation with Rich Cyburt, Dimitris Galanakis, Francesco Miniati, Telemachos Mouschovias, Tijana Prodanović, Kostas Tassis, and Ben Wandelt.

Parts of this work received support from: the Greek State Scholarships Foundation in the form of an Award for Graduate Studies Abroad; Zonta International in the form of an Amelia Earhart Fellowship; the University of Illinois in the form a Graduate College Fellowship; and the National Science Foundation grant AST-0092939.

Table of Contents

List of Tables.....	vii
List of Figures.....	viii
1 Introduction.....	1
1.1 The Double Distribution	1
1.2 Cosmic Accretion Shocks	4
2 The Double Distribution Of Cosmic Structures	7
2.1 Overview	7
2.2 Random Walks and the Press-Schechter Mass Function	10
2.3 Derivation of the Double Distribution	15
2.4 Converting Between Linear And Spherical Density Contrasts	19
2.4.1 Exact Conversion in an Einstein-de Sitter Universe	19
2.4.2 Exact Conversion in an $\Omega_m + \Omega_\Lambda = 1$ Universe	24
2.4.3 An Approximate Conversion Relation	40
2.4.4 Clustering Scale Lengths and Correction for Central Object Contamination	41
2.5 Derivative Quantities of the Double Distribution	43
2.6 Results	44
3 Cosmic Accretion Shocks.....	56
3.1 Overview	56
3.2 Properties of a single shock	58
3.3 Properties of the population of Cosmic Accretion Shocks	60
3.3.1 Accreted Material of a Single Temperature	63
3.3.2 Accreted Material of Varying Temperature	65
3.4 Results	69
3.4.1 Distribution of Environmental Sound Speeds	69
3.4.2 Properties of Accretion Shocks: Effects of the Local Environment	70
3.4.3 Comparison with Cosmological Simulations	81
4 Discussion.....	84

A Limits of the Double Distribution	88
A.1 Behavior of the Double Distribution in the limit $\beta \rightarrow \infty$	88
A.2 Behavior of the Double Distribution in the limit $\beta \rightarrow 1$	89
B Derivation of the Press-Schechter Mass Function From the Double Distribution.....	91
C Vacuum Integrals.....	93
C.1 The incomplete vacuum integral of the first kind \mathcal{V}_1	93
C.1.1 Definition	93
C.1.2 Properties	93
C.2 The hyperbolic vacuum integral of the first kind \mathcal{H}_1	94
C.2.1 Definition	94
C.2.2 Properties	94
C.3 The incomplete vacuum integral of the second kind \mathcal{V}_2	95
C.3.1 Definition	95
C.3.2 Properties	95
C.4 The hyperbolic vacuum integral of the second kind \mathcal{H}_2	96
C.4.1 Definition	96
C.4.2 Properties	96
D Comparison to Bertschinger Similarity Solution.....	98
References	100
Biographical Note.....	103

List of Tables

2.1	Characteristic times of the spherical evolution model in an $\Omega_m + \Omega_\Lambda = 1$ universe.	30
2.2	Applicability limits for different branches of the spherical evolution solution, where: $\delta_{\text{Ed}}(a)$ is the density contrast of the Eddington over-density; $\delta_{\text{ta}}(a)$ is the density contrast of an overdensity turning around at a ; $\delta_v(a)$ is the density contrast of overdensity reaching its virial size at a ; and $\delta_c(a)$ is the density contrast of virialized overdensity formally collapsing to a point at a	35
2.3	Different branches of conversion relation $\tilde{\delta}_0(a, \delta)$ for an $\Omega_m + \Omega_\Lambda = 1$ universe, where: branch I is $-1 < \delta \leq \delta_{\text{Ed}}$; branch II is $\delta_{\text{Ed}} < \delta \leq \delta_{\text{ta}}$; branch III is $\delta_{\text{ta}} < \delta \leq \delta_v$; and branch IV is $\delta_v < \delta \leq \delta_c$	38
2.4	Different branches of derivative $\partial\tilde{\delta}_0/\partial\delta _a$ for an $\Omega_m + \Omega_\Lambda = 1$ universe. The roman numerals correspond to different branches as in Table 2.3	39

List of Figures

2.1	Surface plots of the double distribution for $z = 0$ and $\beta = 2$ in $\Omega_m + \Omega_\Lambda = 1$ (left panel) and Einstein-deSitter (right panel) universes. The mass is measured in M_\odot . The vertical axis is linear, with the $m - \delta$ axes level corresponding to $dn/dmd\delta_\ell = 0$ and the highest point corresponding to $dn/dmd\delta_\ell = 2.72 \times 10^{-2}$ (left panel) and $dn/dmd\delta_\ell = 1.89 \times 10^{-1}$ (right panel) objects per Mpc^3 per $10^{15}M_\odot$	45
2.2	Slices of the double distribution function at various fixed values of the mass for $\Omega_m + \Omega_\Lambda = 1$ (left panel) and Einstein-deSitter (right panel) universes. The units of the double distribution are number of objects per Mpc^3 per $10^{15}M_\odot$	47
2.3	Slices of the double distribution function at $m = 5.5 \times 10^{14} M_\odot$ and for various values of redshift z , for $\Omega_m + \Omega_\Lambda = 1$ (left panel) and Einstein-deSitter (right panel) universes. The units of the double distribution are number of objects per Mpc^3 per $10^{15}M_\odot$	47
2.4	Slices of the double distribution function at constant values of δ for $z = 0$, $\beta = 2$ and for $\Omega_m + \Omega_\Lambda = 1$ (left panel) and Einstein-deSitter (right panel) universes. Solid line: $\delta = -0.5$; dashed line: $\delta = 0$; dot-dashed line: $\delta = 0.5$; double-dot-dashed line: $\delta = 3$. The units of the double distribution are number of objects per Mpc^3 per $10^{15}M_\odot$	48
2.5	Slices of the double distribution function at constant values of δ for $z = 0$, $\beta = 2$, and for $\Omega_m + \Omega_\Lambda = 1$ (left panel) and Einstein-deSitter (right panel) universes. Solid line: $\delta = 10$; dashed line: $\delta = 20$; dot-dashed line: $\delta = 30$. The units of the double distribution are number of objects per Mpc^3 per $10^{15}M_\odot$	49
2.6	Distribution of structures with respect to local density contrast, $dn/d\delta (> 10^{12} M_\odot)$, for $\beta = 2$ and for $\Omega_m + \Omega_\Lambda = 1$ (left panel) and Einstein-deSitter (right panel) universes. Solid line: $z = 0$; dashed line: $z = 1$; dot-dashed line: $z = 2$; double-dot-dashed line: $z = 3$. The units of $dn/d\delta$ are number of objects per Mpc^3	49
2.7	Distribution of density of matter inside collapsed structures with respect to local density contrast, $d\rho/d\delta (> 10^{12} M_\odot)$, for $\beta = 2$ and for $\Omega_m + \Omega_\Lambda = 1$ (left panel) and Einstein-deSitter (right panel) universes. Solid line: $z = 0$; dashed line: $z = 1$; dot-dashed line: $z = 2$; double-dot-dashed line: $z = 3$. The units of $d\rho/d\delta$ are M_\odot per Mpc^3	51

2.8	Fraction by number $f_{n,\text{un}}$ (solid line) and my mass $f_{\rho,\text{un}}$ (dashed line) of objects of mass $> 10^{12} M_{\odot}$ living in underdense regions, as a function of redshift, for $\Omega_m + \Omega_{\Lambda} = 1$ (left panel) and Einstein-deSitter (right panel) universes.	51
2.9	Slices of the double distribution function at $m = 5.5 \times 10^{14}, M_{\odot}$ and for different values of the clustering scale parameter β , for $\Omega_m + \Omega_{\Lambda} = 1$ (left panel) and Einstein-deSitter (right panel) universes, plotted in linear scale. Solid line: $\beta = 1.5$; dashed line: $\beta = 2$; dot-dashed line: $\beta = 3$; double-dot-dashed line: $\beta = 10$. The units of the double distribution are number of objects per Mpc^3 per $10^{15} M_{\odot}$	53
2.10	Distribution of structures of mass larger than $10^{12} M_{\odot}$ with respect to local density contrast, $dn/d\delta$, for $\Omega_m + \Omega_{\Lambda} = 1$ (left panel) and Einstein-deSitter (right panel) universes, at $z = 0$, and for $\beta = 1.5$ (solid line), $\beta = 2$ (dashed line) and $\beta = 10$ (dot-dashed line). The units of $dn/d\delta$ are number of objects per Mpc^3	54
3.1	Distribution of number of objects (left panel, in units of objects per comoving Mpc^3) and mass density (right panel, in units of $M_{\odot} \text{Mpc}^{-3}$) per C_s interval, for objects with mass $> 10^{12} M_{\odot}$, in a WMAP concordance universe. Solid line: $z = 0$; dashed line: $z = 1$; dot-dashed line: $z = 2$	69
3.2	Number distribution of shocks per logarithmic Mach number interval for the Press-Schechter-based model (left panel) and the double-distribution-based models (middle and left panels). The middle panel models implement a halo mass cutoff identical to that of the Press-Schechter case, while the right panel model assumes no mass cutoff. The units of the vertical axes are number of objects per comoving Mpc^3 . Solid line: $z = 0$; dashed line: $z = 1$; dot-dashed line: $z = 2$	70
3.3	Distribution of number density of objects per logarithmic Mach number interval for the double-distribution-based model without a mass cutoff, plotted in logarithmic scale. The units of the vertical axes are number of objects per comoving Mpc^3 . Solid line: $z = 0$; dashed line: $z = 1$; dot-dashed line: $z = 2$	74
3.4	Distribution of spatial density of shock surface per logarithmic Mach number interval ($dS/s \ln \mathcal{M}$) for the Press-Schechter-based (left panel) and the double-distribution-based (right panel) models. The units of the vertical axes are comoving Mpc^{-1} . Solid line: $z = 0$; dashed line: $z = 1$; dot-dashed line: $z = 2$	75
3.5	Accretor mass distribution (mass density in accretors per logarithmic Mach number interval of associated accretion shock, $d\rho/d \ln \mathcal{M}$) for the Press-Schechter-based (left panel) and the double-distribution-based models, with a Press-Schechter like mass cutoff (middle panel) and without an explicit mass cutoff (right panel). The units of the vertical axes are M_{\odot} comoving Mpc^{-3} . Solid line: $z = 0$; dashed line: $z = 1$; dot-dashed line: $z = 2$	76

3.6	Mass current distribution (spatial density of mass current per logarithmic Mach number interval ($dJ/d \ln \mathcal{M}$)) for the Press-Schechter-based (left panel) and the double-distribution-based (right panel) models. The units of the vertical axes are M_{\odot} comoving Mpc^{-3} yr. Solid line: $z = 0$; dashed line: $z = 1$; dot-dashed line: $z = 2$	77
3.7	Kinetic power distribution (spatial density of kinetic power processed by accretion shocks per logarithmic Mach number interval, $dP/d \ln \mathcal{M}$) for the Press-Schechter-based (left panel) and the double-distribution-based (right panel) models. The units of the vertical axes are 10^{40} ergs s^{-1} comoving Mpc^{-3} (left axis) and 10^{51} ergs per century per comoving Mpc^3 (right axis). Solid line: $z = 0$; dashed line: $z = 1$; dot-dashed line: $z = 2$	78
3.8	Distribution of spatial density of kinetic power per logarithmic Mach number interval ($dP/s \ln \mathcal{M}$) the double-distribution-based model without a mass cutoff. Left panel: $z = 2$; middle panel: $z = 1$; right panel: $z = 0$. Solid line: overall distribution; dot-dashed line: contribution from structures with environmental overdensities between δ_{ta} and δ_{v} (between turnaround and virialization overdensities); dashed line: contribution from structures with environmental overdensities $\delta < \delta_{\text{ta}}$	79
3.9	Integrated kinetic power over shocks of any Mach number, P , for the Double-Distribution (solid line) and the Press-Schechter (dashed line) models. Left panel: redshift history of P for $z < 10$. Right panel: $\int P dt$ in units of eV per baryon. The horizontal line in the right-panel plot corresponds to 13.6 eV per baryon.	80
3.10	Integrated mass current over shocks of any Mach number, J , for the Double-Distribution (solid line) and the Press-Schechter (dashed line) models. Left panel: redshift history of J for $z < 10$. Right panel: $\int J dt$ expressed as the fraction of baryons in the universe which have been processed by accretion shocks.	81

AN ANALYTIC MODEL OF ENVIRONMENTAL EFFECTS
ON COSMIC STRUCTURE FORMATION
AND AN APPLICATION TO COSMIC ACCRETION SHOCKS

Vasiliki Pavlidou, Ph.D.

Department of Astronomy

University of Illinois at Urbana-Champaign, 2005

Brian D. Fields, Advisor

We present a new analytic tool for the study of cosmic structure formation, a *double distribution* function of dark matter halos, with respect to both object mass and local over- (or under-) density. The double distribution provides a statistical treatment of the properties of matter *surrounding* collapsed objects, and can be used to study environmental effects on hierarchical structure formation.

We apply this new tool to the case of cosmic accretion shocks. We investigate and quantify the effect of environmental factors on the statistical properties of these shocks. For this purpose, we explore two different models. The first “control” model uses a Press-Schechter mass function to describe the population of collapsed structures, and assumes that all objects accrete gas of the same density and temperature. The second model treats the accreted material as a multi-temperature, multi-density medium with densities and temperatures derived from the double distribution. We find that the shock environment significantly alters the physical impact of cosmic accretion shocks on the intergalactic medium, as well as the cosmic history of their properties.

Chapter 1

Introduction

The large-scale structure of the universe has been investigated with increasing intensity for almost a century. Cosmologists have been using multi-wavelength observations, analytical models, and massive numerical simulations to study the properties of galaxies, galaxy clusters, and superclusters, their formation, and their evolution.

Structure in the universe is believed to be seeded by small, random density fluctuations in the early universe, which grow gravitationally in a process further complicated by the interplay between baryons, radiation, dark matter, and dark energy. In this context, the observationally relevant predictions of any theory of structure formation are the *statistical properties* of the resulting, observable population of cosmic structures.

1.1 The Double Distribution

Cosmological distributions have long been used for the study of cosmic structure formation with great success as an analytical tool complementary to numerical simulations. They have been used to constrain the cosmological parameters; interpret results of cosmological simulations; study regions of the parameter space which cannot be approached by simulations due to prohibitive computational cost; explore the

effects of various physical processes in an efficient if approximate way. The analytical tool used most widely in cosmology is the mass function of dark matter halos (distribution of the number density of halos with respect to halo mass). Analytical descriptions of dark matter halos are usually based on the Press-Schechter formalism ([1; 2]) and its extensions (e.g., [3; 4; 5; 6]). The Press-Schechter mass function has been shown to agree well with results of N-body simulations (e.g., [7; 8; 9]). More sophisticated approaches taking into account deviations from spherical symmetry (e.g., [10; 11; 12]) have improved this agreement even further.

To derive the Press-Schechter mass function, one begins with a density perturbation field still in its linear regime. Regions in space are then smoothed on successively smaller scales. The mass of a collapsed object is then taken to be the largest smoothing mass scale for which the average linear overdensity exceeds some threshold. In this way, matter in the universe is distributed among collapsed structures of different masses, which all share the same value of average overdensity (the threshold value). Information about the local environment of collapsed objects (whether they live in underdensities or overdensities) is thus erased.

For this reason, and despite its wide applicability, the expression for the mass function cannot be used to address environment-related questions: Does the mass function of structures in superclusters differ from the mass function inside voids? Are structures of some particular mass more likely to reside inside underdense or overdense regions in space? How does such a preference evolve with redshift, and how sensitively does it depend on the cosmological parameters? How does the state of the material surrounding and accreted by a collapsed object depend on the mass of the object and the cosmic epoch?

To address such questions, we seek a *double distribution* of the number density of structures with respect to mass but also to local overdensity (or underdensity). In order to extract information about the surroundings of collapsed structures, we

use the same random walk formalism which rigorously yields the Press-Schechter mass function ([2; 3]). Integration of this distribution over density contrast should return the Press-Schechter mass function so that the successes of the Press-Schechter formalism be retained.

Two complications arise in the effort to expand the Press-Schechter mass function to incorporate a description of the local overdensity. First, the concept of the “local environment” is somewhat vague and needs to be defined in a more rigorous way. The size of the “local environment” cannot be the same for all structures. If this was the case, very small structures would represent only a tiny fraction of the “environment”, while very large structures could even exceed the size of the “environment”, which would be an unphysical situation. This problem is not exclusive to analytical tools, but also needs to be addressed when analyzing the results of numerical simulations. Second, the Press-Schechter treatment of the density field uses linear theory, and ways of converting this information to a more physical non-linear result need to be determined.

We address the first problem by introducing a *clustering scale parameter*, β , which allows us to define the size of the “environment” of each structure as a function of its mass. We address the second concern by calculating conversion relations between the linear-theory overdensities (or underdensities) and those predicted by the spherical-evolution model.

Environment-related questions in cosmological structure formation have also been addressed using analytical models for the clustering properties of dark halos which evaluate quantities such as the cross-correlation function between dark halos and matter, and the biasing factor (e.g. [13; 14; 15; 16; 17; 18; 19], also see review by [20] and references therein). These analyses are based on the same random walk formalism which we use here to derive our double distribution (also see [21] for fitting formulae from N-body simulation results). However, the information content of the

double distribution, which treats the “environment” in a mass-dependent fashion, is complementary to that of correlation functions, which describe the clustering properties of the dark halo population at some *fixed spatial scale*. The double distribution is ideally fitted for population studies of cosmological objects. If the properties of a single object can be parametrized as a function of its mass and its environment, then the double distribution can be used to predict the statistical properties of such objects, as well as their evolution with time, for any cosmological model.

We present such an application of the double distribution for the case of cosmic accretion shocks. The properties of cosmic accretion shocks depend sensitively on their environment, and for this reason the double distribution is the tool of choice to study this population of cosmic structures.

1.2 Cosmic Accretion Shocks

The formation of shocks in the baryonic component of matter in the universe is an inevitable and integral part of the process of cosmological structure formation. The longstanding question of the dark baryons¹ [22; 23; 24; 25] is likely on its way to resolution with the first evidence [26; 27; 28; 29] for a large component of diffuse, low-density intergalactic gas distributed in the filaments that comprise the “cosmic web,” and detected in the X-ray forest [30; 31; 32] via absorption lines from highly-ionized metals. This warm-hot intergalactic medium is thought to arise in structure formation shocks [30; 33; 34; 35; 36]. Moreover, structure formation shocks heat the intergalactic medium and are likely to act as acceleration sites for nonthermal particles, the “structure formation cosmic rays” (e.g. [37; 38; 39; 40; 41; 42; 43] and references therein). Such a cosmic-ray population would have distinct γ -ray

¹a fraction of the baryonic content of the universe which, until recently, has eluded detection, presumably because its temperature ($10^5 - 10^7$ K) is too high to produce Ly α absorption while its density is too low to be detected in emission with currently available equipment

and light-element signatures, which are currently subjects of intense investigation [40; 44; 45; 46; 47; 48; 49; 50; 51; 52; 53; 54; 55; 56; 57; 58].

Cosmic shocks occur during different facets of structure formation and in a variety of environments, hence there are two possible ways to categorize them: according to the physical processes causing them, and according to the state of the medium in which they form.

There are three principal processes associated with cosmic structure formation which result in the formation of large-scale shocks.

1. Accretion of intergalactic gas by a collapsed, virialized structure. In this case, an *accretion shock* is formed at the interface between virialized and diffuse gas [59; 60; 61]. The shock is driven by the gravitational attraction exerted on the diffuse gas by the accretor.
2. Merger of two collapsed structures. In this case, a *merger shock* is formed at the interface between the gas components of the merging objects [41; 61]. The shock is driven by the mutual gravitational attraction between the objects.
3. Blast-like expansion of a void (an underdensity in its non-linear regime). The regions compressed between expanding voids form large-scale filaments, and *filament shocks* are formed at the interface between the expanding void and the compressed gas [62]. In this case, the shocks are driven by the expansion of the void rather than the gravity of the filaments.

Shocks can also be divided according to the state of the gas passing through them, into *external* and *internal* shocks [63]. External shocks process pristine material, which has never been shocked before by any of the processes described above. External shocks are mostly filament shocks, since the process of formation of individual virialized structures (associated with the other two types of shocks) occurs principally within filaments, and therefore in most cases involves gas which has al-

ready been processed at least by filament shocks. Internal shocks process gas which has already been shock-heated in the past. All merger shocks, as well as many accretion shocks, are internal shocks.

Since external shocks process colder material of lower sound speed, their Mach numbers are generally higher than those of internal shocks. However, because the gas passing through internal shocks has already been compressed, internal shocks process more mass and kinetic energy than external shocks.

In the second part of this thesis, we present an analytical study of the population of accretion shocks, in a concordance $\Omega_m + \Omega_\Lambda = 1$ universe. We use the double distribution of cosmic structures to describe the accreting structures as well as their environment at a given redshift. Other Press-Schechter extensions have been used to model different “families” of large-scale cosmic shocks by [41] and [64], who model merger shocks, and by [35], who describe large-scale shocks that may appear when overdense perturbations reach and exceed their turnaround point. Here, we present the first analytic model for *accretion* shocks, and we include, for the first time, a detailed treatment of the environment in which accreting structures reside.

This thesis is organized as follows. In chapter 2 we derive the double distribution of cosmic structures, and we explore its information content by plotting the distribution itself as well as interesting derivative quantities for different cosmological models. In chapter 3 we apply the double distribution to study the effect of environment on the statistical properties of the population of cosmic accretion shocks around collapsed structures. We discuss our findings in chapter 4.

Chapter 2

The Double Distribution Of Cosmic Structures

2.1 Overview

The double distribution of cosmic structures with respect to mass and local over-density is a cosmological statistical distribution which describes how the number density of collapsed and virialized dark matter objects is distributed among different masses and among different local density contrasts with respect to the cosmic mean density. In this chapter we derive the double distribution of cosmic structures and we explore its information content.

The derivation of the double distribution is based on the “random walk” formalism, which was introduced for the derivation of cosmological mass functions from an early (linear) field of density fluctuations by [2] and by [3]. The basic simplifying assumptions behind building a mass function starting from a linear overdensity field are:

1. All matter in the universe can be distributed among collapsed objects, and there is no diffuse matter in the universe.

2. At any given cosmic epoch, all structures can be viewed as though they have just virialized.
3. All collapsed objects at a given cosmic epoch have the same mean matter density.
4. All collapsed objects at a given cosmic epoch are spherically symmetric.
5. The mean density of a certain region at a very early cosmic epoch (while all density perturbations are still growing linearly) contains adequate information to predict the mean density of the same region at much later times.

The conceptual idea behind the process necessary to produce a mass function is the following.

- We focus at a infinitesimal mass element centered on a fixed point in space.
- Starting at an infinite mass scale and gradually proceeding to smaller mass scales, we smooth the linear density field and evaluate the mean overdensity at the scale under consideration (note that at an infinite mass scale the mean overdensity is always zero, since the smoothing identically returns the mean cosmic density).
- We convert the smoothed linear overdensity to a nonlinear overdensity using the spherical evolution model. If the result is equal to the mean nonlinear overdensity of virialized objects, then the mass scale at which the smoothing took place is the mass of the collapsed object which hosts the infinitesimal mass under consideration. If not, we repeat the smoothing at a smaller mass scale, until the desired mean overdensity is reached.
- We then repeat the process for all points in space, and thus calculate how much mass corresponds to every *collapsed object mass* interval.

The random walk formalism now recognizes that the smoothed overdensity executes a “random walk” with changing smoothing mass scale, and uses this fact to calculate the probability that any given point in space belongs to a collapsed object with mass in a specific interval. This probability can then be manipulated to give us the mass function. The mathematical details of this process are briefly reviewed in section 2.2.

In our case, we would like to additionally retain information about the density of the region within which a collapsed structure is embedded. For this reason, we need to keep track of the mean density evaluated at a random walk “step” (a smoothing mass scale) preceding the final step which returns the virial density of the collapsed object. The “distance” in mass between the two “steps” of interest will determine how far from the collapsed object the “local environment” extends. In our derivation of the double distribution the ratio of the mass scale representing the environment of an object (including the object itself) over the mass of the object is defined as β , the “clustering scale parameter”. It is a free parameter in our model, and, for every realization of our model, it is the same for all structures. In section 2.3 we present the details of the derivation of the double distribution through this extension of the random walk formalism.

As we discussed above, a critical step in deriving both the Press-Schechter mass function as well as the double distribution of cosmic structures is the conversion of a density contrast evaluated using linear theory to a density contrast evaluated using an exact (if idealized) model. Since we have assumed that all structures are spherically symmetric, we will consider the “true” density contrast to be the one given by the spherical evolution model. In section 2.4 we derive such conversion relations between the linear and the spherical evolution models, by expanding the spherical model around zero overdensity and demanding that at early times the growth of density perturbations according to both models agree to first order. We derive exact conversion relations for both Einstein-de Sitter (flat, matter-only) and Λ CDM (flat,

matter + cosmological constant) universes. In addition, we present a useful and simple approximate conversion relation, which exhibits the correct asymptotic behavior at early as well as late times, and has an accuracy better than 2% throughout its domain.

In section 2.5 we define several interesting integral moments of the double distribution, describing the statistical properties of the population of collapsed cosmic structures and their distribution among different (overdense or underdense) environments. Finally, in section 2.6 we explore the information content of the double distribution by plotting both the double distribution itself as well as several of its integral moments, for different redshifts and different cosmologies. Our principal finding is that for every cosmic epoch and every collapsed object mass, there is a pronounced peak in the double distribution, corresponding to a “most probable” overdensity (or underdensity) for the local environment of the structure. The location of this peak

- moves towards higher overdensities with increasing redshift;
- moves towards higher overdensities with increasing object mass;
- depends only very mildly on the value of β for low β (while it eventually moves towards zero overdensity as $\beta \rightarrow \infty$)
- has a qualitatively similar behavior for both cosmological models we examined.

At the present cosmic epoch, most structures are located inside underdensities.

2.2 Random Walks and the Press-Schechter Mass Function

The Press-Schechter mass function of collapsed structures is the comoving number density of virialized objects per differential mass interval, dn/dm , for every cosmic

epoch a ¹. A related quantity is the mass fraction, $P(>m, a)$, which is the fraction of matter in the universe belonging to collapsed structures with mass $>m$. If $P(>m, a)$ is known, then dn/dm can be calculated from

$$\frac{dn}{dm}(m, a) = \frac{\rho_{m,0}}{m} \left| \frac{d}{dm} P(>m, a) \right|, \quad (2.1)$$

where $\rho_{m,0}$ is the present-day matter density of the universe.

$P(>m, a)$ is in turn calculated by assigning, at each epoch a , every infinitesimal element dm in the universe to a collapsed structure of some mass m . A structure is considered “collapsed” if its mean overdensity

$$\langle \delta \rangle = \frac{\langle \rho_{\text{structure}} \rangle - \rho_{m,a}}{\rho_{m,a}} \quad (2.2)$$

exceeds a certain critical value, $\delta_c(a)$. In Eq. (2.2), $\rho_{m,a}$ is the mean matter density of the universe at epoch a . The critical overdensity $\delta_c(a)$ is the mean overdensity predicted by the spherical evolution model for a structure virializing at epoch a . For each point in space, one calculates the mean local overdensity by smoothing the overdensity field $\delta(\vec{x}, a)$ with a spherically symmetric filter function of varying mass scale, starting from $m \rightarrow \infty$, where one averages over the whole universe and finds identically $\langle \delta \rangle = 0$, and proceeding to successively smaller scales. When a mass scale is found for which the mean overdensity becomes equal to $\delta_c(a)$, it is taken to be the mass m of the parent object of the infinitesimal mass at the point under consideration. This way of assigning object masses circumvents the structure-in-structure problem, since the mass of the parent object is always the *largest possible mass* satisfying the criterion for collapse. All information on substructure within collapsed structures is thus erased from the resulting mass function.

The way the average overdensity $\langle \delta \rangle$ changes when the smoothing mass scale is

¹The *proper* mass function, i.e. the number of collapsed structures per unit proper volume per differential mass interval is simply related to the comoving mass function via $dn/dm|_{\text{proper}} = a^{-3}dn/dm|_{\text{comoving}}$

varied resembles, under certain conditions, a 1D random walk [2]. For all “particles” (points in space in our case), the walk begins at the “spatial origin” ($\langle \delta \rangle = 0$), at “time zero” ($m \rightarrow \infty$). As “time progresses” (m decreases), each “particle” may move either to the “left” (negative $\langle \delta \rangle$) or to the “right” (positive $\langle \delta \rangle$). An “absorbing wall” exists at $\delta_c(a)$. If this “wall” is reached, the “particle” is “removed” from the walk (the point is assigned its parent object mass and removed from further consideration at smaller values of m). $P(> m, a)$ is then the fraction of “particles” which have been “lost” by “time” m , and it can be calculated using random-walk theory.

However, we must first ensure that simple random-walk theory is indeed applicable. First, each “step” of the “walk” should be completely independent from the previous step. This requires that the k -modes producing an increase $\Delta \langle \delta \rangle$ in the space-like variable not appear in any of the previous steps in $\langle \delta \rangle$. A smoothing window function sharp in k -space,

$$\hat{W}_m(k) = \begin{cases} 1 & k < k_c(m) \\ 0 & k > k_c(m) \end{cases} . \quad (2.3)$$

(see [2] and [3] for more extended discussions on the consequences of such a choice) enforces this condition, since

$$\langle \delta \rangle_{m, \vec{x}_0} = \int W_m(|\vec{x}_0 - \vec{x}|) \delta(\vec{x}) d^3 \vec{x} = \int_{k \leq k_c(m)} \delta_k e^{i \vec{x}_0 \cdot \vec{k}} d^3 \vec{k} \quad (2.4)$$

and

$$\Delta \langle \delta \rangle_{\vec{x}_0} = \int_{k_c(m) \leq k \leq k_c(m-dm)} \delta_k e^{i \vec{x}_0 \cdot \vec{k}} d^3 \vec{k} \quad (2.5)$$

which only involves new k -modes corresponding to scales from m to $m - dm$.

Second, there must be an equal probability for the system to “move” towards any one of the two available “directions”. A Gaussian overdensity field (which is the usual assumption for deriving analytic mass functions and which we adopt here) guarantees that this condition is satisfied.

Finally, the appropriate “time-like” variable (which should depend on m) needs to be selected, given that the “space-like” variable is $\langle \delta \rangle$. By direct analogy to the 1D random walk theory result $\langle x^2 \rangle = 2Dt$, and from the definition of the variance of the overdensity field $S(m)$,

$$S(m) = \sigma^2(m) = \langle |\delta(m, \vec{x})|^2 \rangle \propto \int_{k=0}^{k(m)} k^2 dk |\delta_k|^2 \quad (2.6)$$

we can immediately identify $Dt \rightarrow S(m)/2$.

Three further complications need to be addressed. First, our knowledge of δ_k and subsequently $S(m)$ is limited at late times. In the early universe, right after matter-radiation equality, $\langle |\delta_k|^2 \rangle$ can be simply described in terms of a power-law in k modified by a transfer function, $\langle |\delta_k|^2 \rangle \propto T^2(k)k^n$. While all δ are still in their linear regime, they simply grow by the linear growth factor (independent of k). However, at later times, when certain structures start departing from the linear regime, we cannot use our simple early-universe expressions for δ_k . Second, $\langle \delta \rangle$ is limited to be ≥ -1 , which introduces a second, reflecting “wall” at a value of $\langle \delta \rangle = -1$, further complicating the random-walk calculations. Finally, the true overdensity field loses its Gaussianity as it evolves past the linear regime.

To circumvent these problems, we define the *linearly extrapolated overdensity field*, $\tilde{\delta}(\vec{x}, a)$, as the overdensity field that would result if all structures continued to grow according to the linear theory until time a . Now $\tilde{\delta}(\vec{x}, a)$ is not limited to be ≥ -1 , since it does not represent real overdensities. In addition, we can always calculate $S(m)$ for $\tilde{\delta}(\vec{x}, a)$, since $\tilde{\delta}_k$ is modified from its simple early-universe expression only by the linear growth factor. Finally, the extrapolated field remains Gaussian at all times.

The linearly extrapolated overdensity $\tilde{\delta}(\vec{x}, a)$ and the associated variance $S(m)$, are time-varying, but the time dependence is well-known (see chapter 3), and the same for both S and $\tilde{\delta}^2$ ². Thus, the time dependence drops out of ratios $\tilde{\delta}/\sqrt{S}$ which

² as seen by Eq. (2.6) re-written for the extrapolated rather than the true overdensity field

appear in the mass function. For this reason we may, without loss of generality, choose any single epoch to evaluate these quantities, with the stipulation that $\tilde{\delta}$ and $S(m)$ must refer to the same epoch. Given that $\sigma(m)$ is often normalized to the present value of σ_8 , a convenient choice of epoch is the present. Then, Eq. (2.6) gives for $S(m)$

$$S(m) = \sigma_8^2 \frac{\int_{k=0}^{k(m)} T^2(k) k^{n+2} dk}{\int_{k=0}^{k(m_8)} T^2(k) k^{n+2} dk}. \quad (2.7)$$

Thus we only consider $\tilde{\delta}(\vec{x}, a_0)$ (the overdensity field linearly extrapolated to the present epoch), which we use instead of the true field $\delta(\vec{x}, a)$ in our random walk formalism³. To find the mass function at a particular cosmic epoch a , we calculate the location of the “absorbing wall”, $\tilde{\delta}_c(a)$. If a structure is predicted to collapse at epoch a according to the spherical evolution model, then $\tilde{\delta}_{0,c}(a)$ is the overdensity this same structure would have had if, instead of turning around and collapsing, it had continued its linear evolution until the present. This $\tilde{\delta}_{0,c}(a)$ is then our “absorbing wall”.

We can now derive the mass fraction and mass function using random walk theory. If a particle executes a one-dimensional random walk with an absorbing boundary at a point x_1 , then its probability $\mathcal{W}(x, t)$ to be between x and $x + dx$ at time t is [65]

$$\mathcal{W}(x, t, x_1) dx = \frac{\exp\left[-\frac{x^2}{4Dt}\right] - \exp\left[-\frac{(2x_1-x)^2}{4Dt}\right]}{2\sqrt{\pi Dt}} dx, \quad (2.8)$$

where $x \leq x_1$. In our case, the probability that a point in space will be assigned an average extrapolated overdensity between $\tilde{\delta}$ and $\tilde{\delta} + d\tilde{\delta}$ when filtered at a scale m

³Physically, the substitution of the true field by the extrapolated field in the “random walk” corresponds to smoothing the extrapolated overdensity field, and then mapping the mean extrapolated overdensity value to a true overdensity value. That true overdensity value is then assumed to accurately represent the result of a smoothing of the true field, which implies $\delta(\langle \tilde{\delta} \rangle) = \langle \delta(\tilde{\delta}) \rangle$. This would be exactly true only if $\delta(\tilde{\delta})$ was linear in $\tilde{\delta}$, which is not the case (see chapter 3). This assumption introduces an inaccuracy inherent to all calculations which employ it, including the Press-Schechter mass function as well as the double distribution.

corresponding to a variance of $S(m)$ is

$$\mathcal{W}(\tilde{\delta}, S, \tilde{\delta}_{0,c}) d\tilde{\delta} = \frac{\exp\left[-\frac{\tilde{\delta}^2}{2S}\right] - \exp\left[-\frac{(2\tilde{\delta}_{0,c} - \tilde{\delta})^2}{2S}\right]}{\sqrt{2\pi S}} d\tilde{\delta}, \quad (2.9)$$

with $\tilde{\delta} \leq \tilde{\delta}_{0,c}$. The mass fraction $P(> m, a)$ is then the fraction of points already “lost” from the walk when filtering at higher mass scales, which is one minus the fraction of points remaining in the walk,

$$\begin{aligned} P(> m, a) &= P(> \tilde{\delta}_{0,c}) = 1 - \int_{-\infty}^{\tilde{\delta}_{0,c}} \mathcal{W}(\tilde{\delta}, S, \tilde{\delta}_{0,c}) d\tilde{\delta} \\ &= \text{erfc}\left(\frac{\tilde{\delta}_{0,c}(a)}{\sqrt{2S(m)}}\right). \end{aligned} \quad (2.10)$$

Then,

$$\frac{dP(> m, a)}{dm} = \frac{1}{\sqrt{2\pi}} \frac{\tilde{\delta}_{0,c}(a)}{S(m)^{3/2}} \frac{dS}{dm} \exp\left[-\frac{\tilde{\delta}_{0,c}(a)^2}{2S(m)}\right], \quad (2.11)$$

and the Press-Schechter mass function can be found using Eq. (2.1),

$$\frac{dn}{dm}(m, a) = \sqrt{\frac{2}{\pi}} \frac{\rho_{m,0}}{m^2} \frac{\tilde{\delta}_{0,c}(a)}{\sqrt{S(m)}} \left| \frac{d \ln \sqrt{S}}{d \ln m} \right| \exp\left[-\frac{\tilde{\delta}_{0,c}(a)^2}{2S(m)}\right]. \quad (2.12)$$

2.3 Derivation of the Double Distribution

We now use the random walk formalism described in the previous section to derive the double distribution of the comoving number density of collapsed structures with respect to object mass m and local environment overdensity δ_ℓ , $dn/(dm d\delta_\ell)$.

For the reasons described in the previous section, we replace the true overdensity field, $\delta(\vec{x}, a)$, with its linear extrapolation to the present time, $\tilde{\delta}(\vec{x}, a_0)$. Thus, we derive the double distribution of comoving n with respect to object mass m and *extrapolated* local environment overdensity $\tilde{\delta}_\ell$, $dn/(dm d\tilde{\delta}_\ell)$. We then use linear theory and the spherical evolution model to establish a conversion relation $\delta(\tilde{\delta}, a)$ and calculate $dn/(dm d\delta_\ell)$ as

$$\frac{dn}{dm d\delta_\ell}(\delta_\ell, m, a) dm d\delta_\ell = \frac{dn}{dm d\tilde{\delta}_\ell} \left[\tilde{\delta}_\ell(\delta_\ell, a), m, a \right] dm \frac{\partial \tilde{\delta}}{\partial \delta_\ell} d\delta_\ell. \quad (2.13)$$

First of all, we need to define the local environment extrapolated overdensity $\tilde{\delta}_\ell$ in a precise way. We would like $\tilde{\delta}_\ell$ to be a measure of the density contrast of the medium in which a collapsed structure is embedded. Clearly, the value of $\tilde{\delta}_\ell$ depends on how far from the structure itself its “environment” extends. We quantify this notion by introducing the *clustering scale parameter*, β , which is defined in the following way: the “environment” of an object of mass m is a surrounding region in space which encompasses mass βm (including the mass of the object). Hence, the local environment extrapolated overdensity $\tilde{\delta}_\ell$ is the result of a filtering of $\tilde{\delta}(\vec{x}, a_0)$ with a filter of scale βm centered on the object.

Formally, the above definition translates as follows. Consider the sharp in k -space filtering function $\hat{W}_m(k)$ discussed previously (Eq. 2.3). The relation between the cutoff wavenumber and the filter mass, $k_c(m)$, is found by considering the form of the filter function in configuration space,

$$W_m(r) = \frac{\sin [k_c(m)r] - k_c(m)r \cos [k_c(m)r]}{2\pi^2 r^3}, \quad (2.14)$$

and multiplying by $\rho_{m,0}$ and integrating over all space, which yields [3],

$$k_c(m) = \left(\frac{6\pi^2 \rho_{m,0}}{m} \right)^{1/3}. \quad (2.15)$$

For a collapsed structure at an epoch a which has mass m and is centered at a point \vec{x}_0 , we can write

$$\tilde{\delta}(m, \vec{x}_0) = \int W_m(|\vec{x}_0 - \vec{x}|) \tilde{\delta}(\vec{x}, a_0) d^3 \vec{x} = \tilde{\delta}_{0,c}(a), \quad (2.16)$$

since the mean extrapolated overdensity of the collapsed structure itself is always the critical value for collapse, $\tilde{\delta}_{0,c}(a)$. For that same object, the *local environment extrapolated overdensity*, $\tilde{\delta}_\ell$, is

$$\tilde{\delta}_\ell(m, \vec{x}_0) = \int W_{\beta m}(|\vec{x}_0 - \vec{x}|) \tilde{\delta}(\vec{x}, a_0) d^3 \vec{x}. \quad (2.17)$$

Equation (2.17) is then the definition of $\tilde{\delta}_\ell$ for a given β . In our double distribution, β is free parameter, which is however constrained to be between 1 and a few on

physical grounds. It cannot be < 1 since the mass of the object's environment always includes the mass of the object itself. In fact, as β approaches 1, the averaging which produces $\tilde{\delta}_\ell$ is taken *only* over the collapsed object itself, and inevitably returns the critical overdensity for collapse, $\tilde{\delta}_{0,c}$, for all objects. In the other extreme, $\beta \gg 1$, the average $\tilde{\delta}$ on a scale βm is no longer a local quantity with respect to the central object. When β grows without bound, $\tilde{\delta}_\ell$ approaches 0 for all collapsed structures, since averaging over the whole universe identically returns the background matter density, which corresponds to a vanishing density contrast. In appendix A we show that our double distribution becomes proportional to a Dirac delta-function around $\tilde{\delta}_\ell = 0$ in the limit $\beta \rightarrow \infty$ and proportional to a Dirac delta-function around $\tilde{\delta}_\ell = \tilde{\delta}_{0,c}$ in the limit $\beta \rightarrow 1$.

We are now ready to use random walk theory results to calculate the double distribution. We first find the fraction of points in space which belong to structures of mass between m and $m + dm$, which in turn are embedded in a medium of mean linearly extrapolated overdensity between $\tilde{\delta}_\ell$ and $\tilde{\delta}_\ell + d\tilde{\delta}_\ell$, $f(m, \tilde{\delta}_\ell, \beta) d\tilde{\delta}_\ell dm$. The double distribution then is

$$\frac{dn}{dmd\tilde{\delta}_\ell} = \frac{\rho_{m,0}}{m} f(m, \tilde{\delta}_\ell, \beta) dmd\tilde{\delta}_\ell. \quad (2.18)$$

The quantity f can be written as

$$fdm d\tilde{\delta}_\ell = (f_1 d\tilde{\delta}_\ell)(f_2 dm) \quad (2.19)$$

where $f_1 d\tilde{\delta}_\ell$ is the fraction of points in space which have an average overdensity between $\tilde{\delta}_\ell$ and $\tilde{\delta}_\ell + d\tilde{\delta}_\ell$ on a smoothing scale βm , and $f_2 dm$ is the fraction of points satisfying the previous condition which belong to collapsed structures of mass between m and $m + dm$.

The first of the two factors above is the fraction of points still in the walk which are found between $\tilde{\delta}$ and $\tilde{\delta} + d\tilde{\delta}$ at a “time” βm . This is the solution of the 1D random walk problem of $\tilde{\delta}_\ell$ as a function of S , with an absorbing boundary at the

critical collapse threshold $\tilde{\delta}_{0,c}$, as given by Eq. (2.9) but for a smoothing scale βm ,

$$f_1 d\tilde{\delta}_\ell = \frac{\exp\left[-\frac{\tilde{\delta}_\ell^2}{2S(\beta m)}\right] - \exp\left[-\frac{(\tilde{\delta}_\ell - 2\tilde{\delta}_{0,c}(a))^2}{2S(\beta m)}\right]}{\sqrt{2\pi S(\beta m)}} d\tilde{\delta}_\ell. \quad (2.20)$$

The second factor (f_2) is the *conditional probability* that a point in space originating from $(\beta m, \tilde{\delta})$ in the mass - overdensity plane, will reach the “wall” for the first time for a smoothing scale between m and $m + dm$. This is then the probability that a particular point in space is absorbed by the “wall” $\tilde{\delta}_{0,c}(a)$ at a particular “time” $S(m)$, provided that the origin of the walk is transferred from $(0, 0)$ to $(S(\beta m), \tilde{\delta}_\ell)$. This probability can then be found if, in the expression for $dP(> m, a)/dm$ (Eq. 2.11), we perform the substitutions $\tilde{\delta}_{0,c} \rightarrow \tilde{\delta}_{0,c} - \tilde{\delta}_\ell$ and $S(m) \rightarrow S(m) - S(\beta m)$. Similar conditional probabilities were originally calculated by [2] and [3] in the context of rates of mergers between halos. In our case, it is

$$f_2 dm = \frac{\left[\tilde{\delta}_{0,c}(a) - \tilde{\delta}_\ell\right] \exp\left[-\frac{(\tilde{\delta}_{0,c}(a) - \tilde{\delta}_\ell)^2}{2[S(m) - S(\beta m)]}\right]}{\sqrt{2\pi} [S(m) - S(\beta m)]^{3/2}} \left|\frac{dS}{dm}\right|_m dm. \quad (2.21)$$

Equations (2.18) and (2.19) then give

$$\begin{aligned} \frac{dn}{dmd\tilde{\delta}_\ell}(m, \tilde{\delta}_\ell, \beta, a) &= \frac{\rho_{m,0}}{m} \frac{\tilde{\delta}_{0,c}(a) - \tilde{\delta}_\ell}{2\pi} \frac{\exp\left[-\frac{\tilde{\delta}_\ell^2}{2S(\beta m)}\right] - \exp\left[-\frac{(\tilde{\delta}_\ell - 2\tilde{\delta}_{0,c}(a))^2}{2S(\beta m)}\right]}{[S(\beta m)]^{1/2} [S(m) - S(\beta m)]^{3/2}} \left|\frac{dS}{dm}\right|_m \\ &\quad \times \exp\left[-\frac{\left(\tilde{\delta}_{0,c}(a) - \tilde{\delta}_\ell\right)^2}{2[S(m) - S(\beta m)]}\right] \end{aligned} \quad (2.22)$$

with $\tilde{\delta}_\ell \leq \tilde{\delta}_{0,c}(a)$ and $\beta > 1$ so $S(m) > S(\beta m)$ ⁴. Equation (2.22) is the double distribution we have sought and is the central result of this chapter. Integrating $dn/(dmd\tilde{\delta}_\ell)$ over $\tilde{\delta}_\ell$ yields the Press-Schechter mass function, as it should. The result is independent of the value of β . We explicitly perform this integration in appendix B.

Note that the functional form of our double distribution is similar with that of the integrand used by [13] in their calculation of the cross-correlation between dark

⁴since $S(m)$ monotonically decreases with m for all physically interesting power spectra

halos and mass using random walk theory, however the second variance of the field (corresponding to our $S(\beta m)$) in their case refers to a fixed clustering radius and is independent of object mass.

2.4 Converting Between Linear And Spherical Density Contrasts

In this chapter, we derive and discuss conversion relations between the linearly extrapolated density contrast entering the double distribution as we derived it using random walk theory, and the more physical density contrast predicted by the spherical evolution theory. In §2.4.1 and 2.4.2 we derive exact expressions for $\tilde{\delta}_\ell(\delta_\ell, a)$ in the case of the spherical evolution model, for an $\Omega_m = 1$ (§2.4.1) and an $\Omega_m + \Omega_\Lambda = 1$ (§2.4.2) universe (note however that all of the equations we have presented up to this point are cosmology-independent, and can therefore be adapted for any cosmological model). In §2.4.3 we present a useful approximation, valid for both types of cosmological models.

2.4.1 Exact Conversion in an Einstein-de Sitter Universe

In this section we derive a conversion relation $\tilde{\delta}_0(a, \delta)$ for an $\Omega_m = 1$ cosmology (here, δ is the density contrast predicted for a density perturbation at cosmic epoch a by the spherical evolution model and $\tilde{\delta}_0$ is the extrapolation of the density contrast to the present cosmic epoch using linear theory). In order to do so, we first calculate $\delta(a)$ from the spherical evolution solution, then calculate $\tilde{\delta}_0$ using linear theory, and finally require that $\delta(a)$ and $\tilde{\delta}_a$ (the linear-theory density contrast at epoch a) should agree at early times.

Spherical Evolution Model in an $\Omega_m = 1$ Universe

The evolution of a spherically symmetric, overdense perturbation in an otherwise homogeneous $\Omega_m = 1$ universe is described by the parametric equations

$$a_p = \frac{2a_{\text{coll}}}{(12\pi)^{2/3}}(1 - \cos \theta), \text{ and } a = a_{\text{coll}} \left(\frac{\theta - \sin \theta}{2\pi} \right)^{2/3}, \quad (2.23)$$

where a_{coll} is the scale factor of the universe when the perturbation formally collapses to a point, a_p is the scale factor of the perturbation, and θ is the development angle. Note that the perturbation will turn around (reach its maximum size, $a_{p,\text{max}} = 4a_{\text{coll}}(12\pi)^{-2/3}$) when $\theta = \pi$, at a time $a = a_{\text{coll}}/2^{2/3}$.

The normalization of Eq. (2.23) is such that the density contrast δ can be expressed as

$$\delta = \left(\frac{a}{a_p} \right)^3 - 1. \quad (2.24)$$

Hence, for any density contrast δ , Eqs. (2.23) and (2.24) can be combined to give a unique development angle $\theta(\delta)$ which is the solution to the transcendental equation

$$\frac{6^{2/3}(\theta - \sin \theta)^{2/3}}{2(1 - \cos \theta)} - (1 + \delta)^{1/3} = 0. \quad (2.25)$$

Similarly, the spherical evolution solution for an underdensity is given by the parametric equations

$$a_p = A_p(\cosh \eta - 1), \text{ and } a = A_p \frac{6^{2/3}}{2}(\sinh \eta - \eta)^{2/3}. \quad (2.26)$$

where η is the development angle in this case. Equation (2.26) together with Eq. (2.24) can be combined as before to give $\eta(\delta)$ as the solution to the transcendental equation

$$\frac{6^{2/3}(\sinh \eta - \eta)^{2/3}}{2(\cosh \eta - 1)} - (1 + \delta)^{1/3} = 0. \quad (2.27)$$

$\tilde{\delta}_0(a, \delta)$ according to the spherical evolution model

The behavior of δ in the linear regime in this cosmology is

$$\tilde{\delta} = \tilde{\delta}_0 a. \quad (2.28)$$

This result should coincide with the linear expansion of the spherical evolution result at early times. Expanding the parametric solution to second nonvanishing order in θ and eliminating θ , we obtain

$$a_p(a) = a \left[1 - \frac{(12\pi)^{2/3}}{20} \frac{a}{a_{\text{coll}}} \right]. \quad (2.29)$$

We then substitute Eq. (2.29) in the definition of δ (Eq. 2.24) to get

$$\tilde{\delta} = \frac{3(12\pi)^{2/3}}{20a_{\text{coll}}} a \quad (2.30)$$

which, by comparison to Eq. (2.28) gives

$$\tilde{\delta}_0 = \frac{3(12\pi)^{2/3}}{20a_{\text{coll}}}. \quad (2.31)$$

Then, the conversion relation we seek is

$$\tilde{\delta}_0(a, \delta) = \frac{6^{2/3} 3}{20a} [\theta(\delta) - \sin \theta(\delta)]^{2/3} \quad (2.32)$$

where $\theta(\delta)$ is given by Eq. (2.25).

Equation (2.32) has the undesirable property that it diverges as θ approaches 2π . This is of course a consequence of the perturbation formally collapsing to a singularity in the spherical evolution model instead of reaching virial equilibrium. If we make the usual assumption that at virialization the radius of the perturbation is $a_{\text{max}}/2$ and we additionally require that

- $\tilde{\delta}_0(a, \delta)$ is continuous and smooth at $\theta = 3\pi/2$
- $a_p = a_{p,\text{max}}$ for all $a \geq a_{\text{coll}}$

then for $\theta > 3\pi/2$ (which corresponds to $\delta > 9(3\pi + 2)^2/8$) we can replace Eq. (2.32) with

$$\begin{aligned} \tilde{\delta}_0(a, \delta) &= \tilde{\delta}_{0,v} + \tilde{\delta}'_{0,v}(\delta - \delta_v) \\ &+ \frac{3(\tilde{\delta}_{0,c} - \tilde{\delta}_{0,v}) - (\delta_c - \delta_v)(2\tilde{\delta}'_{0,v} + \tilde{\delta}'_{0,c})}{(\delta_c - \delta_v)^2} (\delta - \delta_v)^2 \\ &+ \frac{(\tilde{\delta}'_{0,c} + \tilde{\delta}'_{0,v})(\delta_c - \delta_v) - 2(\tilde{\delta}_{0,c} - \tilde{\delta}_{0,v})}{(\delta_c - \delta_v)^3} (\delta - \delta_v)^3 \end{aligned} \quad (2.33)$$

(see §2.4.2 for a discussion of the reasons for employing this particular functional form, and §2.6 for a discussion on why the effect of such a choice on the double distribution is negligible). In Eq. (2.33),

$$\begin{aligned}
\delta_v &= \left(\frac{a|_{\theta=3\pi/2}}{a_p|_{\theta=3\pi/2}} \right)^3 - 1 = \frac{9(3\pi+2)^2}{8} - 1 \\
\delta_c &= \left(\frac{a|_{\theta=2\pi}}{a_p|_{\theta=3\pi/2}} \right)^3 - 1 = 18\pi^2 - 1 \\
\tilde{\delta}_{0,v} &= \tilde{\delta}_0(a, \delta_v) = \frac{3^{5/3}}{20a} (3\pi+2)^{2/3} \\
\tilde{\delta}'_{0,c} &= \left. \frac{\partial \tilde{\delta}_0}{\partial \delta} \right|_{\delta=\delta_c} = \frac{1}{10a(1+\delta_c)^{2/3}}, \tag{2.34}
\end{aligned}$$

the last equality coming from the fact that after a_{coll} the radius of a perturbation remains constant and equal to $a_{p,\text{max}}/2$, while its density contrast δ changes only due to the expansion of the background universe, $\delta = (2a/a_{p,\text{max}})^3 - 1$ or $\delta = (10a\tilde{\delta}_0/3)^3 - 1$. Finally, $\tilde{\delta}_{0,c}$ is given by Eq. (2.39) while $\tilde{\delta}'_{0,v}$ is given by Eq. (2.40) for $\delta = \delta_v$ and $\theta = 3\pi/2$.

To get the linear behavior of δ for an underdensity we expand the parametric solution 2.26 to second nonvanishing order in η and we eliminate η to get

$$a_p = A_p \frac{6^{2/3}}{2} \left[1 + \frac{1}{10} \frac{a}{A_p} \right]. \tag{2.35}$$

Substituting Eq. (2.35) in the definition of δ (Eq. 2.24), we get for the time dependence of δ at early times,

$$\tilde{\delta} = -\frac{3}{10A_p} a \tag{2.36}$$

from which, by comparison to Eq. (2.28), we get

$$\tilde{\delta}_0 = -\frac{3}{10A_p}. \tag{2.37}$$

Then, $\tilde{\delta}_0(a, \delta)$ will be

$$\tilde{\delta}_0(a, \delta) = -\frac{6^{2/3} 3}{20a} [\sinh \eta(\delta) - \eta(\delta)]^{2/3} \tag{2.38}$$

where $\eta(\delta)$ is given by Eq. (2.27).

Equation (2.38) is valid for all η and its limit as $\tilde{\delta} \rightarrow -\infty$ is $\delta(\tilde{\delta}) \rightarrow -1$. Thus, although the linearly extrapolated field can become < -1 , the corresponding value of the actual δ is always ≥ -1 , as the physical requirement $\rho_p \geq 0$ demands.

Critical extrapolated overdensity for collapse, $\tilde{\delta}_{0,c}(a)$

The critical extrapolated overdensity for collapse can be found from Eq. (2.31)

$$\tilde{\delta}_{0,c}(a_{\text{coll}}) = \frac{3(12\pi)^{2/3}}{20} a_{\text{coll}}^{-1} \approx 1.69 a_{\text{coll}}^{-1}. \quad (2.39)$$

Note that the above equation has the functional form $\tilde{\delta}_{0,c}(a_{\text{coll}}) \propto 1/D(a_{\text{coll}})$, where $D(a)$ is the linear growth factor for this cosmology. This is also true in the $\Omega_m + \Omega_\Lambda = 1$ case.

$$\partial \tilde{\delta}_0 / \partial \delta|_a$$

In addition to the relation between δ and $\tilde{\delta}_0$, we will also need the derivative $\partial \tilde{\delta}_0 / \partial \delta|_a$ in order to convert between true and extrapolated overdensity differentials in Eq. (2.13). In the case of an overdense structure, $\delta > 0$, Eq. (2.32) gives

$$\left. \frac{\partial \tilde{\delta}_0}{\partial \delta} \right|_a = \frac{6^{2/3}}{10a} \frac{1 - \cos \theta(\delta)}{[\theta(\delta) - \sin \theta(\delta)]^{1/3}} \frac{d\theta}{d\delta}. \quad (2.40)$$

To evaluate $d\theta/d\delta$ we define the auxiliary function

$$F_a(\theta, \delta) = 6^{2/3}(\theta - \sin \theta)^{2/3} - 2(1 - \cos \theta)(1 + \delta)^{1/3}. \quad (2.41)$$

From Eq. (2.25) we get immediately $F_a(\theta, \delta) = 0$, and differentiating we get $dF_a = 0 = \frac{\partial F_a}{\partial \theta} d\theta + \frac{\partial F_a}{\partial \delta} d\delta$. Hence,

$$\frac{d\theta}{d\delta} = -\frac{\partial F_a}{\partial \delta} \left(\frac{\partial F_a}{\partial \theta} \right)^{-1}, \quad (2.42)$$

where

$$\frac{\partial F_a}{\partial \delta} = -\frac{2}{3} \frac{1 - \cos \theta}{(1 + \delta)^{2/3}} \quad (2.43)$$

and

$$\frac{\partial F_a}{\partial \theta} = \frac{6^{2/3} 2}{3} \frac{1 - \cos \theta}{(\theta - \sin \theta)^{1/3}} - 2(1 + \delta)^{1/3} \sin \theta. \quad (2.44)$$

Equation (2.40) is valid only for $0 < \delta < \delta_v$. For $\delta > \delta_v$ Eq. (2.33) gives

$$\begin{aligned} \left. \frac{\partial \tilde{\delta}_0}{\partial \delta} \right|_a &= \tilde{\delta}'_{0,v} \\ &+ 2 \frac{3(\tilde{\delta}_{0,c} - \tilde{\delta}_{0,v}) - (\delta_c - \delta_v)(2\tilde{\delta}'_{0,v} + \tilde{\delta}'_{0,c})}{(\delta_c - \delta_v)^2} (\delta - \delta_v) \\ &+ 3 \frac{(\tilde{\delta}'_{0,c} + \tilde{\delta}'_{0,v})(\delta_c - \delta_v) - 2(\tilde{\delta}_{0,c} - \tilde{\delta}_{0,v})}{(\delta_c - \delta_v)^3} (\delta - \delta_v)^2. \end{aligned} \quad (2.45)$$

In the case of an underdense structure, $\delta < 0$, Eq. (2.38) gives

$$\left. \frac{\partial \tilde{\delta}_0}{\partial \delta} \right|_a = -\frac{6^{2/3}}{10a} \frac{\cosh \eta(\delta) - 1}{[\sinh \eta(\delta) - \eta(\delta)]^{1/3}} \frac{d\eta}{d\delta}. \quad (2.46)$$

As before, in order to evaluate $d\eta/d\delta$ we define the auxiliary function

$$G_a(\eta, \delta) = 6^{2/3}(\sinh \eta - \eta)^{2/3} - 2(\cosh \eta - 1)(1 + \delta)^{1/3}. \quad (2.47)$$

Equation (2.27) implies $G_a(\eta, \delta) = 0$ so

$$\frac{d\eta}{d\delta} = -\frac{\partial G_a}{\partial \delta} \left(\frac{\partial G_a}{\partial \eta} \right)^{-1}, \quad (2.48)$$

where

$$\frac{\partial G_a}{\partial \delta} = -\frac{2}{3} \frac{\cosh \eta - 1}{(1 + \delta)^{2/3}}, \quad (2.49)$$

and

$$\frac{\partial G_a}{\partial \eta} = \frac{6^{2/3} 2}{3} \frac{\cosh \eta - 1}{(\sinh \eta - \eta)^{1/3}} - 2(1 + \delta)^{1/3} \sinh \eta. \quad (2.50)$$

2.4.2 Exact Conversion in an $\Omega_m + \Omega_\Lambda = 1$ Universe

In this section we will derive a conversion between true and extrapolated overdensity, $\delta(\tilde{\delta}_0, a)$ for an $\Omega_m + \Omega_\Lambda = 1$ cosmological model. We will do so by first calculating the true density contrast $\delta(a)$ of a density perturbation at cosmic epoch a as predicted

by the spherical evolution model, then calculating $\tilde{\delta}_0$, which is the overdensity of the same spherical perturbation if extrapolated according to the linear theory until the present cosmic epoch, and finally requiring that at early times linear theory and the linear expansion of the spherical evolution model should give the same result.

Spherical Evolution Model in an $\Omega_m + \Omega_\Lambda = 1$ Cosmology: The Evolution Equation

In the spherical evolution model, the spherical density perturbation under consideration behaves as an independent non-flat sub-universe. Its evolution is dictated by a Friedmann equation,

$$\left(\frac{da_p}{dt} \right)^2 = H_0^2 \Omega_m a_p^2 (a_p^{-3} + \omega - \kappa a_p^{-2}) \quad (2.51)$$

where a_p is the radius of such a spherical density perturbation in an otherwise homogeneous universe, $\omega = \Omega_\Lambda/\Omega_m = \Omega_m^{-1} - 1$ (where Ω_m and Ω_Λ are the matter and vacuum density parameters of the background universe) and κ is a constant characteristic of the amplitude and sign of the perturbation: the larger the $|\kappa|$, the larger the deviation from homogeneity at a given time, while a positive κ corresponds to an overdensity and a negative κ to an underdensity. Clearly then in Eq. (2.51), the first term in parentheses on the RHS is the matter term, the second is the vacuum term and the third is the curvature term, which can have a positive or negative sign depending on whether we are studying an “open” (underdensity) or “closed” (overdensity) perturbation. The normalization of a_p is such that, had the specific spherical region begun its evolution with no curvature ($\kappa = 0$), a_p at the present cosmic epoch would have been $a_{p(\kappa=0),0} = 1$. For this reason, the density contrast δ of the perturbation at epoch a is given by Eq. (2.24)

The behavior of the perturbation radius a_p as a function of the universe scale factor a can be found by taking the ratio of the Friedmann equations of the perturbation

and the background universe, thus obtaining [66]

$$\left(\frac{da_p}{da}\right)^2 = \frac{a_p^{-1} + \omega a_p^2 - \kappa}{a^{-1} + \omega a^2} = \frac{a}{a_p} \frac{\omega a_p^2 - \kappa a_p + 1}{\omega a^3 + 1}. \quad (2.52)$$

Equation (2.52) implies that the smallest positive perturbation which will turn around and collapse corresponds to the smallest positive κ for which the equation

$$\omega a_p^3 - \kappa a_p + 1 = 0 \quad (2.53)$$

has a real positive solution [9]. This gives

$$\kappa_{\min, \text{coll}} = 3\omega^{1/3}/2^{2/3}. \quad (2.54)$$

Equation (2.52) can then be re-written as

$$\frac{da_p}{da} = \begin{cases} \left(\frac{a_p^{-1} + \omega a_p^2 - \kappa}{a^{-1} + \omega a^2}\right)^{1/2}, & \kappa < \kappa_{\min, \text{coll}} \quad \text{or} \\ & \kappa \geq \kappa_{\min, \text{coll}}, \quad a < a_{\text{ta}} \\ -\left(\frac{a_p^{-1} + \omega a_p^2 - \kappa}{a^{-1} + \omega a^2}\right)^{1/2}, & \kappa \geq \kappa_{\min, \text{coll}}, \quad a > a_{\text{ta}} \end{cases} \quad (2.55)$$

where a_{ta} is the scale factor of the universe when the perturbation reaches its maximum (or *turnaround*) radius. The turnaround radius is the smallest of the two positive solutions of Eq. (2.53),

$$a_{p, \text{ta}} = \omega^{-1/3} \sqrt{\frac{4}{3} \frac{\kappa}{\omega^{1/3}}} \cos \frac{1}{3} \left(\cos^{-1} \sqrt{\frac{27}{4} \left(\frac{\kappa}{\omega^{1/3}}\right)^{-3}} + \pi \right). \quad (2.56)$$

Equation (2.56) has an asymptotic behavior $a_{p, \text{ta}} \approx 1/\kappa$ when $\kappa/\omega^{1/3} \gg 1$, as expected from Eq. (2.53). The maximum possible turnaround radius, $a_{p, \text{ta}, \text{max}}$ is achieved for $\kappa = \kappa_{\min, \text{coll}}$ and is $a_{p, \text{ta}, \text{max}} = (2\omega)^{-1/3}$. All other collapsing overdensities will have $a_{p, \text{ta}} < a_{p, \text{ta}, \text{max}}$.

Qualitative Description of the Evolution of Structures

The introduction of the additional vacuum term in the Friedmann equation considerably complicates the simple classification of density perturbations to overdensities (all of which turn around and collapse in an $\Omega_m = 1$ cosmology) and underdensities (all of which expand forever). In the $\Omega_m + \Omega_\Lambda = 1$ universe there exist overdensities which will continue to expand forever. The behavior of a perturbation in such a cosmology is parametrized by the quantity $\kappa/\omega^{1/3}$, and we can identify the following cases.

Case I, $\kappa/\omega^{1/3} \leq -1$: large underdensities, expanding forever. The table below shows the relative magnitude of the three terms in the Friedmann equation (matter, curvature and vacuum term) for different values of the scale factor of the perturbation. The first line in the table indicates the hierarchy of the three terms, from largest to smaller, for each range of the scale factor. The second line indicates the dominant term in each scale factor range. The third line shows the approximate dependence of the radius of the perturbation, a_p , on time, assuming that only the dominant term contributes to the Friedmann equation in each range.

$a_p < \frac{1}{ \kappa }$	$\frac{1}{ \kappa } < a_p < \frac{1}{\sqrt[3]{\omega}}$	$\frac{1}{\sqrt[3]{\omega}} < a_p < \sqrt{\frac{ \kappa }{\omega}}$	$a_p > \sqrt{\frac{ \kappa }{\omega}}$
MCV	CMV	CVM	VCM
matter	curvature	curvature	vacuum
$a_p \sim t^{2/3}$	$a_p \sim t$	$a_p \sim t$	$a_p \sim e^t$

Case II, $-1 < \kappa/\omega^{1/3} \leq 1$: small perturbations, expanding forever.

These can be either underdensities ($\kappa < 0$) or overdensities ($\kappa > 0$). In both cases the curvature term never becomes dominant. The following table shows their different evolutionary stages (as in Case I).

$a_p < \sqrt{\frac{ \kappa }{\omega}}$	$\sqrt{\frac{ \kappa }{\omega}} < a_p < \frac{1}{\sqrt[3]{\omega}}$	$\frac{1}{\sqrt[3]{\omega}} < a_p < \frac{1}{ \kappa }$	$a_p > \frac{1}{ \kappa }$
MCV	MVC	VMC	VCM
matter	matter	vacuum	vacuum
$a_p \sim t^{2/3}$	$a_p \sim t^{2/3}$	$a_p \sim e^t$	$a_p \sim e^t$

Case III, $1 < \kappa/\omega^{1/3} < 3/2^{2/3}$: “coasting” overdensities, expanding forever. These overdensities continue to expand forever despite the fact that they go through a phase in their evolution when the curvature term becomes dominant and their expansion slows down. During this phase, the contributions of the matter and vacuum terms, which are the ones driving the expansion, add up to a value always higher than the curvature term, although the curvature term is larger than each one of them. When the perturbation enters the curvature-dominated phase, the expansion rate decreases and the perturbation grows much more mildly than $t^{2/3}$. The expansion rate reaches a minimum at $a_p = (2\omega)^{-1/3}$, after which it increases again as the perturbation approaches the phase of exponential expansion. This phase between the matter-like expansion and the exponential expansion is denoted by (*) in the table below.

$a_p < \frac{1}{\kappa}$	$\frac{1}{\kappa} < a_p < \frac{1}{\sqrt[3]{\omega}}$	$\frac{1}{\sqrt[3]{\omega}} < a_p < \sqrt{\frac{\kappa}{\omega}}$	$a_p > \sqrt{\frac{\kappa}{\omega}}$
MCV	CMV	CVM	VCM
matter	curvature	curvature	vacuum
$a_p \sim t^{2/3}$	(*)	(*)	$a_p \sim e^t$

Cases I-III are all sub-cases of the Lemaître model ([67], [68]), which features an inflection point at $a_{p,e} = (2\omega)^{-1/3}$ where $\ddot{a}_p = 0$ while $\dot{a}_p > 0$. The rate of expansion initially decreases to achieve its minimum (positive) value when $a_p = a_{p,e}$, after which point the expansion accelerates again.

Special Case, $\kappa/\omega^{1/3} = 3/2^{2/3}$: Eddington Overdensity. This overdensity is the lowest κ overdensity which does not expand to an infinite radius. However, it

does not turn around and collapse, but it approaches its (finite) turnaround radius, $a_{p,\max} = (2\omega)^{-1/3}$ (from Eq. 2.56) as $t \rightarrow \infty$. As seen by an observer inside this overdensity, as $t \rightarrow \infty$ the part of the universe outside $a_{p,\max}$ will accelerate away and eventually exit the horizon, and the observable universe (“local Eddington bubble”) will asymptotically approach the Einstein static universe (as in the Eddington model with a cosmological constant).

Case IV, $\kappa/\omega^{1/3} > 3/2^{2/3}$: large overdensities, eventually collapsing.

When such a structure enters the dominant-curvature-term phase, its expansion rate starts to decrease ($a_p \sim t^\epsilon$ with $\epsilon = \epsilon(t)$ monotonically decreasing from $2/3$ to 0), until the expansion halts, at $a_p = a_{p,ta}$ which occurs at a time t_{ta} , given in table 2.1. After t_{ta} the perturbation turns around and contracts, its evolution being symmetrical in time about t_{ta} , i.e. $a_p(t) = a_p(2t_{ta} - t)$ for $t > t_{ta}$ (this is a consequence of Eq. (2.51) and holds for any cosmological model as long as the RHS of the Friedmann equation involves no explicit time-dependence). Eventually, the perturbation will formally collapse to a singularity at time $t_{coll} = 2t_{ta}$.

$a_p < \frac{1}{\kappa}$	$\frac{1}{\kappa} < a_p < a_{p,ta}$	$a_{p,ta} > a_p > \frac{1}{\kappa}$	$\frac{1}{\kappa} > a_p$
MCV	CMV	CMV	MCV
matter	curvature	curvature	matter
$a_p \sim t^{2/3}$	$a_p \sim t^\epsilon$	$a_p \sim (2t_{ta} - t)^\epsilon$	$a_p \sim (2t_{ta} - t)^{2/3}$
expansion	expansion	contraction	contraction

In all of the cases discussed above, the transitions between different phases of their evolution occur at characteristic times, those of matter-vacuum equality t_{MV} , matter-curvature equality t_{MC} and curvature-vacuum equality t_{CV} . At these times (shown in table 2.1), the corresponding terms in the Friedmann equation become equally important. Note that in the case of the Eddington overdensity and of case IV collapsing overdensities, matter-vacuum equality and curvature-vacuum equality are never reached, and the vacuum term never dominates over any of the other terms.

Table 2.1: Characteristic times of the spherical evolution model in an $\Omega_m + \Omega_\Lambda = 1$ universe.

event	time
turnaround	$t_{ta} = \frac{1}{H_0\sqrt{\Omega_m}} \int_0^{a_{p,ta}} da_p \sqrt{\frac{a_p}{\omega a_p^3 - \kappa a_p + 1}}$
matter-vacuum equality	$t_{MV} = \frac{1}{H_0\sqrt{\Omega_m}} \int_0^{\omega^{-1/3}} da_p \sqrt{\frac{a_p}{\omega a_p^3 - \kappa a_p + 1}}$
matter-curvature equality	$t_{MC} = \frac{1}{H_0\sqrt{\Omega_m}} \int_0^{ \kappa ^{-1}} da_p \sqrt{\frac{a_p}{\omega a_p^3 - \kappa a_p + 1}}$
curvature-vacuum equality	$t_{CV} = \frac{1}{H_0\sqrt{\Omega_m}} \int_0^{\sqrt{\frac{ \kappa }{\omega}}} da_p \sqrt{\frac{a_p}{\omega a_p^3 - \kappa a_p + 1}}$

In the next section we derive exact solutions for the time-evolution of a_p for perturbations of different curvature. However, surprisingly accurate approximate solutions can be derived using only linear theory and Eq. (2.81). Solving for the spherical collapse density contrast we get

$$\delta_a \approx \left(1 - \frac{\tilde{\delta}_a}{\tilde{\delta}_c} \right)^{-\tilde{\delta}_c} - 1. \quad (2.57)$$

Since $a_p = a(1 + \delta_a)^{-1/3}$, we can write for collapsing overdensities

$$\begin{aligned} a_p &\approx a \left[1 - \frac{\tilde{\delta}_c D(a)/D(a_c)}{\tilde{\delta}_c} \right]^{\tilde{\delta}_c/3} \\ &= a \left[1 - \frac{D(a)}{D(a_{coll})} \right]^{\tilde{\delta}_c/3}. \end{aligned} \quad (2.58)$$

where the initial conditions (curvature) of the perturbation are parametrized by its collapse epoch, a_{coll} , while the cosmology enters through the functional form of the linear growth factor and the linear collapse overdensity, $\tilde{\delta}_c$. Similarly, for perturbations

which expand forever we can write

$$\begin{aligned} a_p &\approx a \left[1 - \frac{\tilde{\delta}_0 D(a)/D(a_0)}{\tilde{\delta}_c} \right]^{\tilde{\delta}_c/3} \\ &= a \left[1 - \frac{\tilde{\delta}_0}{\tilde{\delta}_c} \frac{D(a)}{D(a_0)} \right]^{\tilde{\delta}_c/3}. \end{aligned} \quad (2.59)$$

where the curvature of the perturbation is parametrized by its extrapolated linear density contrast at the present epoch, $\tilde{\delta}_0$. Note that for overdensities which expand forever, $\tilde{\delta}_0 > 0$ and $a_p < a$, while for underdensities $\tilde{\delta}_0 < 0$ and $a_p > a$. Also, because $D(a)$ asymptotes to a constant value for $a \rightarrow \infty$ (as we will see in the next sections), a_p grows proportionally to a at late times. This is the exponential expansion phase, described in our analysis above.

Solutions of the Evolution Equation

For eventually collapsing structures ($\kappa \geq \kappa_{\min, \text{coll}}$), separation of variables in Eq. (2.55) and integration yields,

$$\int_0^a \frac{\sqrt{y} dy}{\sqrt{\omega y^3 + 1}} = \begin{cases} \int_0^{a_p} \frac{\sqrt{x} dx}{\sqrt{\omega x^3 - \kappa x + 1}} & a < a_{\text{ta}} \\ 2 \int_0^{a_{\text{p,ta}}} \frac{\sqrt{x} dx}{\sqrt{\omega x^3 - \kappa x + 1}} - \int_0^{a_p} \frac{\sqrt{x} dx}{\sqrt{\omega x^3 - \kappa x + 1}} & a \geq a_{\text{ta}} \end{cases}, \quad (2.60)$$

where a_{ta} is the cosmic epoch when $a_p = a_{\text{p,ta}}$. Now the integral on the LHS of Eq. (2.60) can be calculated using [9]

$$\int \frac{\sqrt{y} dy}{\sqrt{\omega y^3 + 1}} = \frac{2}{3} \omega^{-1/2} \sinh^{-1} \sqrt{\omega y^3}. \quad (2.61)$$

The integral of the RHS can be re-written as

$$\int_0^{a_p} \frac{\sqrt{x} dx}{\sqrt{\omega x^3 - \kappa x + 1}} = \frac{2}{3} \omega^{-1/2} \mathcal{V}_1(r, \mu) \quad (2.62)$$

where \mathcal{V}_1 is the *incomplete vacuum integral of the first kind*, defined in appendix C, and

$$r = a_p/a_{\text{p,ta}}, \quad \mu = (\omega a_{\text{p,ta}}^3)^{-1}. \quad (2.63)$$

Note that for this range of curvature values, $\kappa/\omega^{1/3}$ (which is the quantity which parametrizes the behavior of the perturbation with time) is a function of μ alone, with

$$\kappa/\omega^{1/3} = (1 + \mu)/\mu^{2/3}. \quad (2.64)$$

Using Eqs. (2.61) and (2.62), Eq. (2.60) can be rewritten as,

$$a = \begin{cases} \omega^{-1/3} \{ \sinh [\mathcal{V}_1(r, \mu)] \}^{2/3}, & a \leq a_{\text{ta}} \\ \omega^{-1/3} \{ \sinh [2\mathcal{V}_1(1, \mu) - \mathcal{V}_1(r, \mu)] \}^{2/3}, & a > a_{\text{ta}} \end{cases}. \quad (2.65)$$

Equation (2.65) is the spherical evolution solution for a collapsing perturbation with amplitude κ (parametrized above by μ) in an $\Omega_\Lambda + \Omega_m = 1$, $\Omega_\Lambda/\Omega_m = \omega$ universe, and gives r (and hence a_p) as a function of a for this model. Note that $\mathcal{V}_1(r, \mu)$ is the development angle for this cosmology.

The scale factor of the universe at turnaround for a given collapsing overdensity can be found immediately from Eq. (2.65),

$$a_{\text{ta}} = \omega^{-1/3} [\sinh \mathcal{V}_1(1, \mu)]^{2/3}. \quad (2.66)$$

The scale factor of the universe at collapse, a_{coll} (when the scale factor of the perturbation becomes formally zero, $a_{p,c} = r_c = 0$) is, from Eq. (2.65) and since $\mathcal{V}_1(0, \mu) = 0$,

$$a_{\text{coll}} = \omega^{-1/3} [\sinh 2\mathcal{V}_1(1, \mu)]^{2/3}. \quad (2.67)$$

Equation (2.65) should not be applied "literally" until the final collapse of the perturbation to a singularity, since the physical picture for the late stages of the evolution of a perturbation involves virialization at a finite radius. It has been shown by [69] that the analogous arguments which give $a_{p,v} = a_{p,ta}/2$ for the $\Omega_m = 1$ cosmology give, for an $\Omega_m + \Omega_\Lambda = 1$ universe,

$$4\omega a_{p,v}^3 - \frac{2 + 2\omega a_{p,ta}^3}{a_{p,ta}} a_{p,v} + 1 = 0. \quad (2.68)$$

The physically meaningful solution of 2.68 which gives the correct behavior for $\omega \rightarrow 0$ is (using Eq. 2.63)

$$a_{p,v} = a_{p,ta} \sqrt{\frac{2\mu+2}{3}} \cos \frac{1}{3} \left(\cos^{-1} \sqrt{\frac{27\mu^2}{(2\mu+2)^3}} + \pi \right). \quad (2.69)$$

The scale factor a_v of the universe when the scale factor of the perturbation *past its turnaround* becomes equal to $a_{p,v}$, will be given by the second branch of Eq. (2.65), for $a_p = a_{p,v}$. Then, the validity range for the second branch of Eq. (2.65) is $a_{ta} < a < a_v$.

For $a > a_v$, we can no longer use the spherical evolution solution to describe the physical picture of interest (virialization). In the next section we will present a simple recipe we will use to follow the late stages of evolution of the perturbation which satisfies the desired boundary conditions ($a_p = a_{p,v}$ at a_{coll} and constant thereafter).

For perpetually expanding structures ($\kappa < \kappa_{min,coll}$), Eq. (2.55) gives

$$\int_0^a \frac{\sqrt{y}dy}{\sqrt{\omega y^3 + 1}} = \int_0^{a_p} \frac{\sqrt{x}dx}{\sqrt{\omega x^3 - \kappa x + 1}}. \quad (2.70)$$

In this case, the integral on the RHS can be rewritten as

$$\int_0^{a_p} \frac{\sqrt{x}dx}{\sqrt{\omega x^3 - \kappa x + 1}} = \frac{2}{3} \omega^{-1/2} \mathcal{H}_1(r, \varpi) \quad (2.71)$$

where \mathcal{H}_1 is the *hyperbolic vacuum integral of the first kind*, defined in appendix C, and

$$r = a_p/|a_{p,R}|, \quad \varpi = (\omega|a_{p,R}|^3)^{-1}, \quad (2.72)$$

where $a_{p,R}$ is the only real (and always negative) root of Eq. (2.53) when $\kappa < \kappa_{min,coll}$,

$$a_{p,R} = \sqrt[3]{\left(\frac{1}{2} - \sqrt{\frac{1}{4} - \frac{\kappa^3}{27\omega}} \right)^2} + \sqrt[3]{\left(\frac{1}{2} + \sqrt{\frac{1}{4} - \frac{\kappa^3}{27\omega}} \right)^2} - \frac{\kappa}{3\omega^{\frac{1}{3}}} \quad (2.73)$$

As in the case of collapsing perturbations, $\kappa/\omega^{1/3}$ is a function of ϖ alone, with

$$\kappa/\omega^{1/3} = (1 - \varpi)/\varpi^{2/3}. \quad (2.74)$$

Then, $\varpi = 1$ is a flat subuniverse (not perturbed with respect to the background), and perturbations with $\varpi > 1$ are underdensities while $1/4 < \varpi < 1$ correspond to non-collapsing overdensities.

Then, Eq. (2.70) becomes

$$a = \omega^{-1/3} \{ \sinh [\mathcal{H}_1(r, \varpi)] \}^{2/3} \quad (2.75)$$

which is the spherical evolution solution for a non-collapsing perturbation with amplitude κ (parametrized above by ϖ) in an $\Omega_\Lambda + \Omega_m = 1$, $\Omega_\Lambda/\Omega_m = \omega$ universe. As for collapsing perturbations, $\mathcal{H}_1(r, \varpi)$ is the development angle.

$\tilde{\delta}_0(\delta)$ according to the spherical evolution model

The linear theory result for a growing-mode perturbation in an $\Omega_m + \Omega_\Lambda = 1$ cosmology is [70]

$$\tilde{\delta} = \tilde{\delta}_0 \frac{D(a)}{D(a_0)} \quad (2.76)$$

where D , the linear growth factor, is given by $D(a) = A[(2\omega)^{1/3}a]$ with

$$A(x) = \frac{(x^3 + 2)^{1/2}}{x^{3/2}} \int_0^x \left(\frac{u}{u^3 + 2} \right)^{3/2} du. \quad (2.77)$$

To find the relation between $\tilde{\delta}_0$ and κ , we expand the exact ($\delta = a^3/a_p^3 - 1$) and linear relations for the overdensity to first order in a and demand that the coefficients be equal. Thus we get [9]

$$\kappa = \frac{(2\omega)^{1/3}}{3A[(2\omega)^{1/3}a_0]} \tilde{\delta}_0 = \frac{(2\omega)^{1/3}}{3A[(2\omega)^{1/3}]} \tilde{\delta}_0, \quad (2.78)$$

since $a_0 = 1$. This is the value of the constant κ for a perturbation which at a cosmic epoch $a_0 = 1$ has a linearly extrapolated overdensity $\tilde{\delta}_0$. Note that since the linear theory result is the same for both underdensities and overdensities, Eq. (2.78) holds for both cases. For underdensities, both κ and $\tilde{\delta}$ will be negative, while for overdensities both will be positive.

Table 2.2: Applicability limits for different branches of the spherical evolution solution, where: $\delta_{\text{Ed}}(a)$ is the density contrast of the Eddington overdensity; $\delta_{\text{ta}}(a)$ is the density contrast of an overdensity turning around at a ; $\delta_{\text{v}}(a)$ is the density contrast of overdensity reaching its virial size at a ; and $\delta_{\text{c}}(a)$ is the density contrast of virialized overdensity formally collapsing to a point at a .

Limit	Expression	Auxiliary Relations
$\delta_{\text{Ed}}(a)$	$\delta_{\text{Ed}}(a) = 2\omega \left(\frac{a}{r_{\text{Ed}}(a)} \right)^3 - 1$	$\sinh^{-1} \sqrt{\omega a^3} - \mathcal{V}_1(r_{\text{Ed}}, 2) = 0$
$\delta_{\text{ta}}(a)$	$\delta_{\text{ta}}(a) = \omega a^3 \mu_{\text{ta}}(a) - 1$	$\sinh^{-1} \sqrt{\omega a^3} - \mathcal{V}_1(1, \mu_{\text{ta}}) = 0$
$\delta_{\text{v}}(a)$	$\delta_{\text{v}}(a) = \left(\frac{a}{a_{\text{p,v}}[\mu_{\text{v}}(a)]} \right)^3 - 1$	$\sinh^{-1} \sqrt{\omega a^3} - 2\mathcal{V}_1(1, \mu_{\text{v}}) + \mathcal{V}_1[r_{\text{v}}(\mu_{\text{v}}), \mu_{\text{v}}] = 0$ $r_{\text{v}}(\mu) = a_{\text{p,v}}(\mu)/a_{\text{p,ta}}(\mu)$
$\delta_{\text{c}}(a)$	$\delta_{\text{c}}(a) = \left[\frac{a}{a_{\text{p,v}}[\mu_{\text{c}}(a)]} \right]^3 - 1$	$\sinh^{-1} \sqrt{\omega a^3} - 2\mathcal{V}_1(1, \mu_{\text{c}}) = 0$

At any given epoch a , there is a unique perturbation (parametrized by κ or, equivalently, by μ or ϖ) which will have achieved a true density contrast δ at that time. Therefore, to calculate the desired conversion relation $\tilde{\delta}_0(a, \delta)$ we first calculate κ (or, equivalently, μ or ϖ) from the given a and δ and the appropriate solution of the evolution equation (2.65 or 2.75). Then, we use Eq. (2.78) to evaluate $\tilde{\delta}_0$.

To determine which is the appropriate solution of the evolution equation we need to use for each δ , we calculate the limits of applicability of each equation in terms of δ .

- Equation (2.75) is applicable for all forever expanding perturbations. For any given epoch a , the maximum density contrast of such perturbations is achieved by the Eddington perturbation and is equal to $\delta_{\text{Ed}}(a)$, given in line 1 of Table 2.2. Then, the applicability domain of Eq. (2.75) is $-1 < \delta \leq \delta_{\text{Ed}}(a)$, and the conversion relation in this case takes the form shown in the 1st line of Table 2.3.
- The first branch of Eq. (2.65) is applicable for eventually collapsing perturbations which, however, have not reached their turnaround radius yet. The maximum δ of all such perturbations at a given a is achieved by the pertur-

bation which is turning around at a , and is equal to $\delta_{\text{ta}}(a)$, given in line 2 of Table 2.2. The applicability domain of the first branch of Eq. (2.65) is then $\delta_{\text{Ed}}(a) < \delta \leq \delta_{\text{ta}}(a)$ and the conversion relation in this case is shown in the 2nd line of table 2.3.

- The second branch of Eq. (2.65) is applicable for eventually collapsing perturbations which are past their turnaround but which have not yet reached their virial radius. The maximum δ of such perturbations at a given a is achieved by the perturbation which is reaching its virial size at a , and is equal to $\delta_{\text{v}}(a)$, given in line 3 of Table 2.2. The applicability domain of the second branch of Eq. (2.65) is then $\delta_{\text{ta}}(a) < \delta \leq \delta_{\text{v}}(a)$ and the conversion relation in this case is shown in the 3rd line of table 2.3.
- Perturbations which have reached their virial size but have not yet reached their designated collapse time, $a_{\text{coll}}(\mu)$, need to be treated separately, since the spherical collapse model fails (does not agree with the physical picture we would like to describe, although it is still formally applicable) for radii smaller than the virial radius. Since a realistic description of the microphysical dissipation processes which lead to virialization is far beyond the scope of this analytical calculation, we will adopt a prescription which is driven by mathematical simplicity. We will assume that for $\delta_{\text{v}}(a) < \delta \leq \delta_{\text{c}}(a)$ the conversion relation $\tilde{\delta}_0(a, \delta)$ has the simplest polynomial form which satisfies the following physically motivated boundary conditions:
 - The extrapolated overdensity is continuous and smooth at δ_{v} , so $\tilde{\delta}_0(a, \delta_{\text{v}}) = \tilde{\delta}_{0,\text{v}}$ and $\partial \tilde{\delta}_0 / \partial \delta \Big|_{\delta_{\text{v}}} = \tilde{\delta}'_{0,\text{v}}$ as given by the appropriate relations of the previous branch (3rd line of tables 2.3 and 2.4 correspondingly).
 - After time $a_{\text{coll}}(\mu)$ the radius of the perturbation remains constant and equal to the virial radius so changes in the (true) overdensity are only

due to the increase of the scale factor of the background universe. This then implies that $\tilde{\delta}_0(a, \delta_c) = \tilde{\delta}_{0,c}$ given by Eq. (2.79) and $\partial\tilde{\delta}_0/\partial\delta|_{\delta_c} = (\partial\tilde{\delta}_0/\partial\mu|_{\mu_c})(\partial\mu/\partial\delta|_{\delta_c}) = \tilde{\delta}'_{0,c}$ given in Table 2.3 line 4.

The conversion relation in this case is shown in Table 2.3 line 4, while its applicability domain is $\delta_v(a) < \delta \leq \delta_c(a)$, with $\delta_c(a)$ given in Table 2.2 line 4. Past their collapse time, perturbations are treated as virialized objects without substructure and are not relevant as “local environment” of other objects for the purposes of our double distribution calculation, hence it is not necessary to have a conversion relation of $\delta > \delta_c(a)$. The calculation would be simplified (this last branch would be unnecessary) if we chose to regard perturbations as virialized objects after the moment they reached their virial size after turnaround, at time a_v . However, we will retain the usual assumption that objects virialize at time a_{coll} for consistency with existing Press-Schechter calculations.

Critical extrapolated overdensity for collapse, $\tilde{\delta}_{0,c}(a)$

We need to find the critical $\tilde{\delta}_{0,c}(a)$ for collapse if the field is linearly extrapolated to the present epoch, i.e. the value the linearly extrapolated to the present overdensity must have, for a structure to have collapsed at universe scale factor a . This, from Eq. (2.78), will be

$$\tilde{\delta}_{0,c}(a) = \frac{3A}{(2)^{1/3}} \frac{[(2\omega)^{1/3}]}{[\mu_c(a)]^{2/3}} \frac{1 + \mu_c(a)}{[\mu_c(a)]^{2/3}} \quad (2.79)$$

where again $\mu_c(a)$ is given by Table 2.2 line 4.

The dependence of $\tilde{\delta}_{0,c}$ on a can also be expressed in terms of the linear growth factor, $D(a)$, as was the case for the $\Omega_m = 1$ universe. The conversion relation between $\delta(a)$ and $\tilde{\delta}_a$ (the linear-theory result for the density contrast at time a) is independent of a . In other words, as long as δ and $\tilde{\delta}$ both refer to the same time, knowledge of the one uniquely defines the other, independently of the actual time at which they are

Table 2.3: Different branches of conversion relation $\tilde{\delta}_0(a, \delta)$ for an $\Omega_m + \Omega_\Lambda = 1$ universe, where: branch I is $-1 < \delta \leq \delta_{\text{Ed}}$; branch II is $\delta_{\text{Ed}} < \delta \leq \delta_{\text{ta}}$; branch III is $\delta_{\text{ta}} < \delta \leq \delta_v$; and branch IV is $\delta_v < \delta \leq \delta_c$.

Branch	$\tilde{\delta}_0(\delta, a) =$	Auxiliary relations
I	$\frac{3A[(2\omega)^{1/3}]}{2^{1/3}} \frac{1-\varpi(a, \delta)}{[\varpi(a, \delta)]^{2/3}}$	$\sinh^{-1} \sqrt{\omega a^3} - \mathcal{H}_1 \left[a \left(\frac{\varpi \omega}{1+\delta} \right)^{1/3}, \varpi \right] = 0$
II	$\frac{3A[(2\omega)^{1/3}]}{2^{1/3}} \frac{1+\mu(a, \delta)}{[\mu(a, \delta)]^{2/3}}$	$\sinh^{-1} \sqrt{\omega a^3} - \mathcal{V}_1 \left[a \left(\frac{\mu \omega}{1+\delta} \right)^{1/3}, \mu \right] = 0$
III	$\frac{3A[(2\omega)^{1/3}]}{2^{1/3}} \frac{1+\mu(a, \delta)}{[\mu(a, \delta)]^{2/3}}$	$\sinh^{-1} \sqrt{\omega a^3} - 2\mathcal{V}_1(1, \mu)$ $+ \mathcal{V}_1 \left[a \left(\frac{\mu \omega}{1+\delta} \right)^{1/3}, \mu \right] = 0$
IV	$\tilde{\delta}_{0,v} + \tilde{\delta}'_{0,v}(\delta - \delta_v)$ $+ \frac{3(\tilde{\delta}_{0,c} - \tilde{\delta}_{0,v}) - (\delta_c - \delta_v)(2\tilde{\delta}'_{0,v} + \tilde{\delta}'_{0,c})}{(\delta_c - \delta_v)^2}$ $\times (\delta - \delta_v)^2$ $+ \frac{(\tilde{\delta}'_{0,c} + \tilde{\delta}'_{0,v})(\delta_c - \delta_v) - 2(\tilde{\delta}_{0,c} - \tilde{\delta}_{0,v})}{(\delta_c - \delta_v)^3}$ $\times (\delta - \delta_v)^3$	$\tilde{\delta}_{0,v} = \tilde{\delta}_0(a, \delta_v)$ (this Table line 3) $\tilde{\delta}'_{0,v} = \frac{\partial \tilde{\delta}_0}{\partial \delta} \Big _{\delta_v}$ (Table 2.4 line 3) $\tilde{\delta}_{0,c} = \tilde{\delta}_0(a, \delta_c)$ (Eq. 2.79) $\begin{aligned} \tilde{\delta}'_{0,c} &= \frac{\partial \tilde{\delta}_0}{\partial \delta} \Big _{\delta_c} \\ &= - \frac{A[(2\omega)^{1/3}](6\omega^{2/3}a_{p,v}^2\mu_c^{2/3} - 1 - \mu_c)}{(2\mu_c^2)^{1/3}(\delta_c + 1)} \end{aligned}$ $\mu_c(a)$ in Table 2.2 line 4

both evaluated. As $\delta(a) \rightarrow \infty$, $\tilde{\delta}_a \rightarrow \tilde{\delta}_c$, the linear-theory density contrast at the time of collapse (given by Eq. 2.79 for $a = 1$). Therefore $\tilde{\delta}_c$ is the same for perturbations of all curvatures, and, using Eq. (2.76), we can write

$$\tilde{\delta}_{0,c}(a_{\text{coll}}) = \tilde{\delta}_c \frac{D(a_0)}{D(a_{\text{coll}})}. \quad (2.80)$$

$$\partial \tilde{\delta}_0 / \partial \delta|_a$$

In addition to the relation between δ and $\tilde{\delta}_0$, we will also need the derivative $\partial \tilde{\delta}_0 / \partial \delta|_a$ in order to convert between true and extrapolated overdensity differentials in Eq. (2.13). The calculation is similar as in the case of an $\Omega_m = 1$ universe, and the results are summarized in table 2.4.

In table 2.4, $\mathcal{H}_2(r, \varpi)$ is the *hyperbolic vacuum integral of the second kind*, and $\mathcal{V}_2(r, \mu)$ is the *incomplete vacuum integral of the second kind*, defined in appendix C.

Table 2.4: Different branches of derivative $\partial\tilde{\delta}_0/\partial\delta|_a$ for an $\Omega_m + \Omega_\Lambda = 1$ universe. The roman numerals correspond to different branches as in Table 2.3

Aux. Function	$\frac{\partial\tilde{\delta}_0}{\partial\delta} _a(a, \delta) =$	Additional Functions
I	$\Phi_1 = \sinh^{-1} \sqrt{\omega a^3} - \frac{\partial\Phi_1}{\partial\delta} \left(\frac{\partial\Phi_1}{\partial\tilde{\delta}_0} \right)^{-1} - \mathcal{H}_1(r, \varpi)$	$\frac{\partial\Phi_1}{\partial\delta} = \frac{a^{3/2}}{2(1+\delta)^{3/2} \sqrt{\frac{a^3}{(1+\delta)} - \frac{a(\varpi-1)}{\varpi^{2/3}(1+\delta)^{1/3}} + \frac{1}{\omega}}}$ $\frac{\partial\Phi_1}{\partial\tilde{\delta}_0} = -\frac{(2\varpi^2)^{1/3}}{3A[(2\omega)^{1/3}]} \mathcal{H}_2 \left[a \left(\frac{\varpi\omega}{1+\delta} \right)^{1/3}, \varpi \right]$ $\sinh^{-1} \sqrt{\omega a^3} - \mathcal{H}_1 \left[a \left(\frac{\varpi\omega}{1+\delta} \right)^{1/3}, \varpi \right] = 0$
II	$\Phi_2 = \sinh^{-1} \sqrt{\omega a^3} - \frac{\partial\Phi_2}{\partial\delta} \left(\frac{\partial\Phi_2}{\partial\tilde{\delta}_0} \right)^{-1} - \mathcal{V}_1(r, \mu)$	$\frac{\partial\Phi_2}{\partial\delta} = \frac{a^{3/2}}{2(1+\delta)^{3/2} \sqrt{\frac{a^3}{(1+\delta)} - \frac{a(\mu+1)}{\mu^{2/3}(1+\delta)^{1/3}} + \frac{1}{\omega}}}$ $\frac{\partial\Phi_2}{\partial\tilde{\delta}_0} = -\frac{(2\mu^2)^{1/3}}{3A[(2\omega)^{1/3}]} \mathcal{V}_2 \left[a \left(\frac{\mu\omega}{1+\delta} \right)^{1/3}, \mu \right]$ $\sinh^{-1} \sqrt{\omega a^3} - \mathcal{V}_1 \left[a \left(\frac{\mu\omega}{1+\delta} \right)^{1/3}, \mu \right] = 0$
III	$\Phi_3 = \sinh^{-1} \sqrt{\omega a^3} - 2\mathcal{V}_1(1, \mu) - \frac{\partial\Phi_3}{\partial\delta} \left(\frac{\partial\Phi_3}{\partial\tilde{\delta}_0} \right)^{-1} + \mathcal{V}(r, \mu)$	$\frac{\partial\Phi_3}{\partial\delta} = -\frac{[a/(1+\delta)]^{3/2}}{2\sqrt{\frac{a^3}{(1+\delta)} - \frac{a(\mu+1)}{\mu^{2/3}(1+\delta)^{1/3}} + \frac{1}{\omega}}}$ $\frac{\partial\Phi_3}{\partial\tilde{\delta}_0} = \frac{(2\mu^2)^{1/3}}{3A[(2\omega)^{1/3}]} \left\{ \mathcal{V}_2 \left[a \left(\frac{\mu\omega}{1+\delta} \right)^{1/3}, \mu \right] - \frac{6\mu}{\mu-2} \frac{d\mathcal{V}_1(1, \mu)}{d\mu} \right\}$ $\sinh^{-1} \sqrt{\omega a^3} - 2\mathcal{V}_1(1, \mu) + \mathcal{V}_1 \left[a \left(\frac{\mu\omega}{1+\delta} \right)^{1/3}, \mu \right] = 0$
IV	—	$\tilde{\delta}'_{0,v} + 2 \frac{3(\tilde{\delta}_{0,c} - \tilde{\delta}_{0,v}) - (\delta_c - \delta_v)(2\tilde{\delta}'_{0,v} + \tilde{\delta}'_{0,c})}{(\delta_c - \delta_v)^2} (\delta - \delta_v)$ $+ 3 \frac{(\tilde{\delta}'_{0,c} + \tilde{\delta}'_{0,v})(\delta_c - \delta_v) - 2(\tilde{\delta}_{0,c} - \tilde{\delta}_{0,v})}{(\delta_c - \delta_v)^3} (\delta - \delta_v)^2$ with $\tilde{\delta}_{0,c}, \tilde{\delta}_{0,v}, \tilde{\delta}'_{0,c}, \tilde{\delta}'_{0,v}$, as in Table 2.3 line 4

2.4.3 An Approximate Conversion Relation

An excellent approximation to these conversion relations can be derived from the expression

$$\tilde{\delta}_a \approx \tilde{\delta}_c \left[1 - (1 + \delta_a)^{-1/\tilde{\delta}_c} \right]. \quad (2.81)$$

Similar approximations were suggested by [71] and [15]. Equation (2.81) relates the linear overdensity at a time a to the true overdensity at the same time, and its accuracy is *better than 2% throughout its domain* for both $\Omega_m = 1$ and $\Omega_m + \Omega_\Lambda = 1$ cosmologies. Its functional form is much simpler and more intuitive than the more accurate fit of [13]. The cosmological model enters only through $\tilde{\delta}_c$. For the Einstein-deSitter universe, $\tilde{\delta}_c$ is given by Eq. (2.39) for $a_{\text{coll}} = 1$, while for the $\Omega_m + \Omega_\Lambda = 1$ universe it is given by Eq. (2.79) for $a = 1$. Note that $\tilde{\delta}_c$ is related to the quantity $\tilde{\delta}_{0,c}(a)$ (which appears explicitly in our double distribution expression) through

$$\tilde{\delta}_{0,c}(a) = \tilde{\delta}_c \frac{D(a_0)}{D(a)} \quad (2.82)$$

where $D(a)$ is the linear growth factor in the relevant cosmology.

The limits of Eq. (2.81) are the same as the ones required for the exact conversion relation. When $|\delta_a| \ll 1$, $\tilde{\delta}_a \approx \delta_a$. In addition, $\tilde{\delta}_a \rightarrow -\infty$ as $\delta_a \rightarrow -1$, and $\delta_a \rightarrow \infty$ as $\tilde{\delta}_a \rightarrow \tilde{\delta}_c$.

Using Eq. (2.81),

$$\tilde{\delta}_\ell \approx \frac{D(a_0)}{D(a)} \tilde{\delta}_c \left[1 - (1 + \delta_\ell)^{-1/\tilde{\delta}_c} \right], \quad (2.83)$$

where a is the time at which we want to evaluate the double distribution. Note that close to virialization, Eq. (2.83) loses its applicability (as does the spherical collapse model), and has to be replaced by a recipe which does not diverge in δ_ℓ . We have presented such recipes in §2.4.1 and 2.4.2, however the exact functional form of the conversion relation in this regime cannot affect any of the physically interesting results as the amplitude of the double distribution decreases rapidly enough with δ_ℓ that the contribution of the high-delta tail to the integrated mass function is negligible. We

have verified this fact by comparing the integral of our double distribution over δ_ℓ with the Press-Schechter mass function. When we extended the integration up to $\delta_{0,c}$, the results agreed to the accuracy of the numerical integration. When we extended our integration only up to $\delta_{0,v}$ (just below the application of our virialization recipe), the error relative to the Press-Schechter mass function was less than 0.02%.

2.4.4 Clustering Scale Lengths and Correction for Central Object Contamination

The definition of β and $\tilde{\delta}_\ell$ described above was sufficient for us to derive the double distribution from random walk theory. However, from a physical point of view, the presence of a collapsed structure at the center of the “environment sphere” contaminates the evaluation of the average “environmental” overdensity. If we want the double distribution to describe the properties of matter *surrounding* collapsed objects, we need to correct for the presence of the objects themselves.

We will employ a simple, “top-hat” physical picture to calculate an appropriate correction (see also [15]). Note however that our correction is approximate, since the filter we used to smooth the overdensity field was k –sharp rather than top-hat in space.

Let δ_c be the (true) overdensity of a collapsed object of mass m and radius R_v , and δ_ℓ be the overdensity of the “environment sphere” of radius R_e . The “environment sphere” encompasses a mass βm , including the central collapsed object. We want to find the average overdensity δ_{ext} of that part of the “environment sphere” which is *external* to the central object. For the collapsed object we can write

$$m = \frac{4}{3}\pi R_v^3(1 + \delta_c)\rho_m, \quad (2.84)$$

where ρ_m is the mean matter density of the universe at the epoch of interest. For the

environment sphere, including the central object, we can write

$$\beta m = \frac{4}{3}\pi R_e^3(1 + \delta_\ell)\rho_m. \quad (2.85)$$

From Eqs. (2.84) and (2.85) we get $R_v^3 = R_e^3(1 + \delta_\ell)/\beta(1 + \delta_c)$. It thus follows that the length scale R_e associated with the clustering parameter β is

$$\begin{aligned} R_e &= \left(\frac{\beta(1 + \delta_c)}{1 + \delta_\ell}\right)^{1/3} R_v \\ &= \left(\frac{3\beta m}{4\pi(1 + \delta_\ell)\rho_m}\right)^{1/3}. \end{aligned} \quad (2.86)$$

We see that for a fixed clustering parameter β , the length scale associated with an object of mass m is mass-dependent, scaling linearly with the virial radius but larger by a factor $[\beta(1 + \delta_c)/(1 + \delta_\ell)]^{1/3} > 1$. Thus, we can roughly think of the clustering scale parameter as a measure of how many virial radii we include as the local environment around each structure⁵.

Having identified the environmental length scale, we can now isolate the environmental overdensity from that of the collapsed object. The volume of the environment sphere external to the central object contains a mass

$$(\beta - 1)m = \frac{4}{3}\pi(R_e^3 - R_v^3)(1 + \delta_{\text{ext}})\rho_m. \quad (2.87)$$

Using Eq. (2.86) to eliminate R_v , and dividing by Eq. (2.85) we obtain

$$\delta_{\text{ext}} = \frac{(\beta - 1)(1 + \delta_\ell)(1 + \delta_c)}{\beta(1 + \delta_c) - (1 + \delta_\ell)} - 1, \quad (2.88)$$

which is the contamination-corrected overdensity for an environment sphere with uncorrected overdensity δ_ℓ . Then, the contamination-corrected double distribution will be given by

$$\frac{dn}{dmd\delta_{\text{ext}}}(\delta_{\text{ext}}, m, a) = \frac{dn}{dmd\delta_\ell}[\delta_\ell(\delta_{\text{ext}}, a), m, a] \frac{d\delta_\ell}{d\delta_{\text{ext}}}, \quad (2.89)$$

⁵Note however that for fixed β , the number of virial radii included in the environment depends on δ_ℓ and is larger for underdense environments.

where

$$\delta_\ell(\delta_{\text{ext}}) = \frac{\beta(1 + \delta_{\text{ext}})(1 + \delta_c)}{(\beta - 1)(1 + \delta_c) + (1 + \delta_{\text{ext}})} - 1 \quad (2.90)$$

and

$$\frac{d\delta_\ell}{d\delta_{\text{ext}}} = \frac{\beta(\beta - 1)(1 + \delta_c)^2}{[(\beta - 1)(1 + \delta_c) + (1 + \delta_{\text{ext}})]^2}. \quad (2.91)$$

2.5 Derivative Quantities of the Double Distribution

We now have enough tools to calculate derivative quantities of interest. The number density of collapsed objects of mass greater than some minimum m_{min} ⁶ embedded in a medium of local overdensity between δ_{ext} and $\delta_{\text{ext}} + d\delta_{\text{ext}}$ is

$$\frac{dn}{d\delta_{\text{ext}}}(> m_{\text{min}})d\delta_{\text{ext}} = d\delta_{\text{ext}} \frac{\partial \tilde{\delta}_\ell}{\partial \delta_\ell} \frac{d\delta_\ell}{d\delta_{\text{ext}}} \int_{m=m_{\text{min}}}^{\infty} \frac{dn}{dm} dm, \quad (2.92)$$

while the density of matter in collapsed objects of mass $> m_{\text{min}}$ embedded in a medium of local overdensity between δ_{ext} and $\delta_{\text{ext}} + d\delta_{\text{ext}}$ is

$$\frac{d\rho}{d\delta_{\text{ext}}}(> m_{\text{min}})d\delta_{\text{ext}} = d\delta_{\text{ext}} \frac{\partial \tilde{\delta}_\ell}{\partial \delta_\ell} \frac{d\delta_\ell}{d\delta_{\text{ext}}} \int_{m=m_{\text{min}}}^{\infty} m \frac{dn}{dm} dm. \quad (2.93)$$

Of all the matter in the universe which belongs to collapsed objects of mass $> m_{\text{min}}$, the fraction by mass which lives in underdense neighborhoods is

$$f_{\rho, \text{un}} = \frac{\int_{\delta_{\text{ext}}=-1}^0 \frac{d\rho}{d\delta_{\text{ext}}}(> m_{\text{min}})d\delta_{\text{ext}}}{\int_{\delta_{\text{ext}}=-1}^{\delta_c} \frac{d\rho}{d\delta_{\text{ext}}}(> m_{\text{min}})d\delta_{\text{ext}}}. \quad (2.94)$$

⁶The introduction of a finite minimum mass m_{min} is necessary for both physical and technical reasons. Physically, the mass of collapsed objects is strictly forced to have a lower bound, not only due to the finite mass of the dark matter particle, but also due to the existence of a dark matter Jeans mass, however small this may be. In addition, the dark matter perturbation transfer function imposes cutoffs at scales of order of an earth mass [? ? ? ?]. Practically, the Press-Schechter dn/dm diverges as $m \rightarrow 0$ and setting a minimum mass is required to extract interesting information. For the purposes of this thesis, the selected mass cutoff will generally be such that the population of interest will include super-galactic scales only.

Then, the mass fraction of the matter defined above which lives in overdensities will be $f_{\rho,ov} = 1 - f_{\rho,un}$.

Similarly, of all the objects with mass $m > m_{\min}$, a fraction by number which lives inside underdensities is

$$f_{n,un} = \frac{\int_{\delta_{\text{ext}}=-1}^0 \frac{dn}{d\delta_{\text{ext}}} (> m_{\min}) d\delta_{\text{ext}}}{\int_{\delta_{\text{ext}}=-1}^{\delta_c} \frac{dn}{d\delta_{\text{ext}}} (> m_{\min}) d\delta_{\text{ext}}}. \quad (2.95)$$

The complementary number fraction of such structures living inside overdensities will be $f_{n,ov} = 1 - f_{n,un}$.

The number-density-weighted mean δ_{ext} for structures of mass $> m_{\min}$ is

$$\langle \delta \rangle_n = \frac{\int_{\delta_{\text{ext}}=-1}^{\delta_c} \delta_{\text{ext}} \frac{dn}{d\delta_{\text{ext}}} (> m_{\min}) d\delta_{\text{ext}}}{\int_{\delta_{\text{ext}}=-1}^{\delta_c} \frac{dn}{d\delta_{\text{ext}}} (> m_{\min}) d\delta_{\text{ext}}} \quad (2.96)$$

with a variance

$$\sigma_{\delta,n}^2 = \frac{\int_{\delta_{\text{ext}}=-1}^{\delta_c} (\delta_{\text{ext}} - \langle \delta \rangle_n)^2 \frac{dn}{d\delta_{\text{ext}}} (> m_{\min}) d\delta_{\text{ext}}}{\int_{\delta_{\text{ext}}=-1}^{\delta_c} \frac{dn}{d\delta_{\text{ext}}} (> m_{\min}) d\delta_{\text{ext}}}. \quad (2.97)$$

Similarly, the matter-density-weighted mean δ for structures of mass $> m_{\min}$ is

$$\langle \delta \rangle_\rho = \frac{\int_{\delta_{\text{ext}}=-1}^{\delta_c} \delta_{\text{ext}} \frac{d\rho}{d\delta_{\text{ext}}} (> m_{\min}) d\delta_{\text{ext}}}{\int_{\delta_{\text{ext}}=-1}^{\delta_c} \frac{d\rho}{d\delta_{\text{ext}}} (> m_{\min}) d\delta_{\text{ext}}} \quad (2.98)$$

with a variance

$$\sigma_{\delta,\rho}^2 = \frac{\int_{\delta_{\text{ext}}=-1}^{\delta_c} (\delta_{\text{ext}} - \langle \delta \rangle_\rho)^2 \frac{d\rho}{d\delta_{\text{ext}}} (> m_{\min}) d\delta_{\text{ext}}}{\int_{\delta_{\text{ext}}=-1}^{\delta_c} \frac{d\rho}{d\delta_{\text{ext}}} (> m_{\min}) d\delta_{\text{ext}}}. \quad (2.99)$$

2.6 Results

In this section we present plots of the double distribution itself as well as of its various physically interesting derivative quantities. We compare results derived for a concordance, $\Omega_m + \Omega_\Lambda = 1$ universe with WMAP parameters ($\sigma_8 = 0.84$, $h = 0.71$, $\Omega_m = 0.27$, $\Omega_b = 0.04$, [24]), and for an Einstein-deSitter ($\Omega_m = 1$) universe with $h = 0.71$, $\Omega_b = 0.04$, but $\sigma_8 = 0.45$. The different power-spectrum

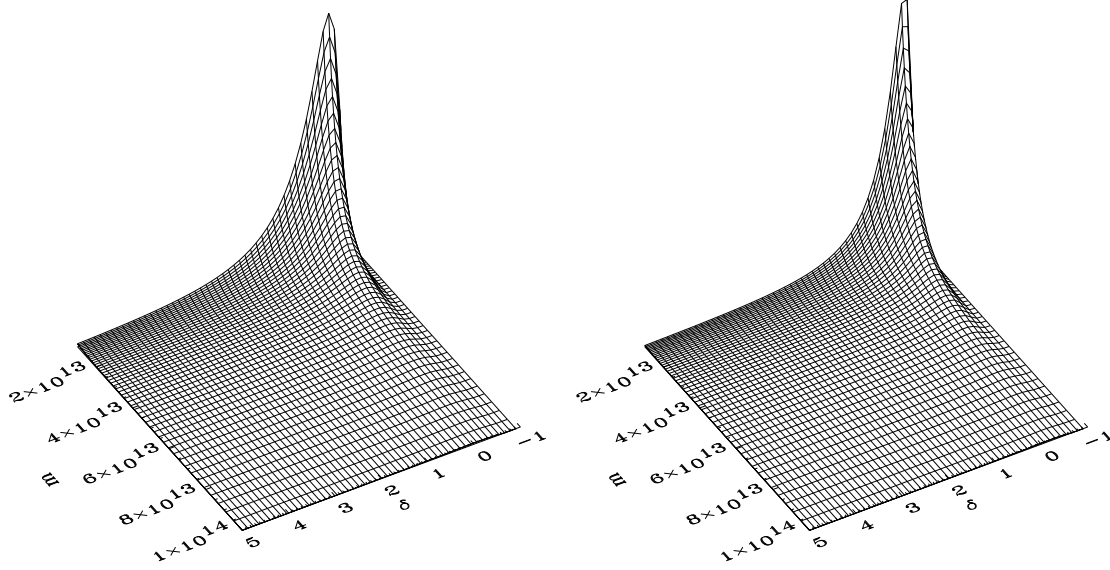


Figure 2.1: Surface plots of the double distribution for $z = 0$ and $\beta = 2$ in $\Omega_m + \Omega_\Lambda = 1$ (left panel) and Einstein-deSitter (right panel) universes. The mass is measured in M_\odot . The vertical axis is linear, with the $m - \delta$ axes level corresponding to $dn/dmd\delta_\ell = 0$ and the highest point corresponding to $dn/dmd\delta_\ell = 2.72 \times 10^{-2}$ (left panel) and $dn/dmd\delta_\ell = 1.89 \times 10^{-1}$ (right panel) objects per Mpc^3 per $10^{15} M_\odot$.

normalization in the Einstein-deSitter case was selected so that the Press-Schechter mass function in this case coincides with that of the concordance universe on a mass scale of $5.5 \times 10^{14} M_\odot$, which is between the values of m_8 (mass included in a sphere of comoving radius $8h^{-1}$ Mpc) for the two cosmologies ($m_8 = 2 \times 10^{14} M_\odot$ for the concordance universe while $m_8 = 8 \times 10^{14} M_\odot$ for the Einstein-de Sitter universe). This value of σ_8 is also consistent with the fits of [9] given the WMAP result for the concordance universe. Finally, we use fitting formulae of [72] for the adiabatic cold dark matter transfer function to calculate the density field variance $S(m)$. In this section, δ always refers to δ_{ext} , the true overdensity of that part of the “environment sphere” which is external to the central object.

Figure 2.1 shows a 3-dimensional rendering of our double distribution as a function of mass and overdensity for fixed $\beta = 2$ and $z = 0$. The left panel corresponds to the concordance universe while the right panel corresponds to the Einstein-deSitter

universe, and this arrangement is retained throughout this section.

The features of the double distribution are demonstrated in more quantitative detail in Figs. 2.2-2.5. Figures 2.2 and 2.3 show slices of the double distribution at constant values of mass. In Fig. 2.2, different curves correspond to different values of the central object mass. In Fig. 2.3, all curves are for an object mass $m = 5.5 \times 10^{15} M_{\odot}$, and different curves correspond to different redshifts. Their most prominent feature is the pronounced peak at a relatively low value of $|\delta|$, indicating that for each given pair of z and m , there is a preferred, “most probable” value of the local environment density contrast. As we can see in Fig. 2.2, the location of this peak moves to higher values of the density contrast as the mass of the object increases: small structures are preferentially located in relative isolation, while larger structures are more likely to be found in clustered environments. This result fits well in the picture of hierarchical structure formation, as smaller structures tend to be merged into higher-mass objects as time progresses. Lower-mass objects which are initially part of underdensities are less probable to undergo mergers, and hence are more likely to survive at late times than objects which are initially part of overdensities. Conversely, higher-mass structures are more likely to be parts of overdensities where they can accumulate mass more easily through mergers with smaller structures.

Note, however, that in the hierarchical structure formation picture, the mass scale where the exponential suppression of collapsed structures sets in increases with time. Thus, any given mass scale starts out as being a “high mass” at early times and eventually becomes a “lower mass” as it enters the power-law regime of the Press-Schechter mass function. Hence, according to the argument we used to explain Fig. 2.2, the double distribution for any given mass scale should peak at increasing δ values with increasing redshift. This is because a particular mass scale used to be closer to the high-mass end of the halo distribution in the past than it is today. Indeed, this is the trend seen in Fig. 2.3. As we would expect, the peak of the distribution moves

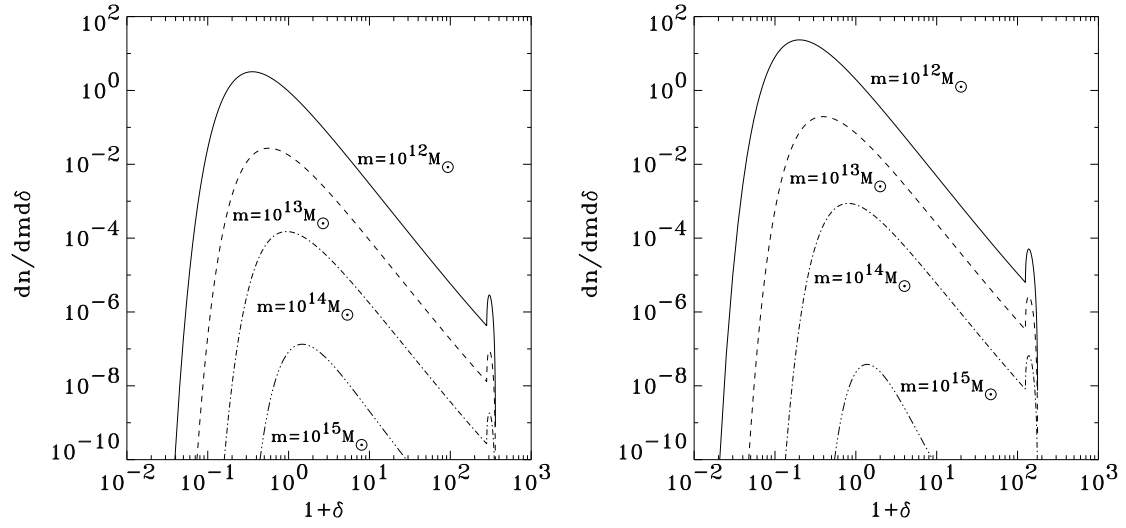


Figure 2.2: Slices of the double distribution function at various fixed values of the mass for $\Omega_m + \Omega_\Lambda = 1$ (left panel) and Einstein-deSitter (right panel) universes. The units of the double distribution are number of objects per Mpc^3 per $10^{15} M_\odot$.

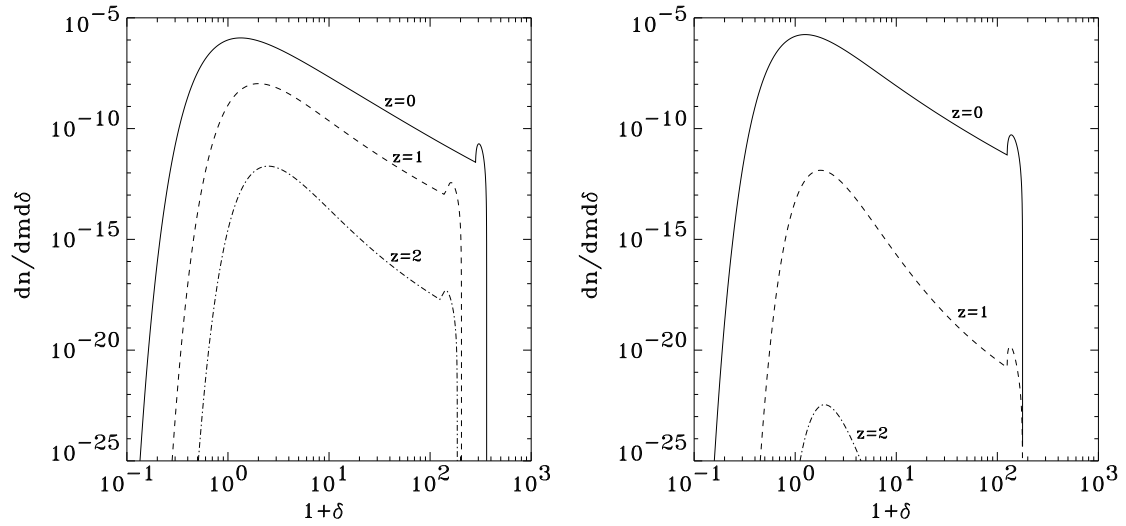


Figure 2.3: Slices of the double distribution function at $m = 5.5 \times 10^{14}, M_\odot$ and for various values of redshift z , for $\Omega_m + \Omega_\Lambda = 1$ (left panel) and Einstein-deSitter (right panel) universes. The units of the double distribution are number of objects per Mpc^3 per $10^{15} M_\odot$.

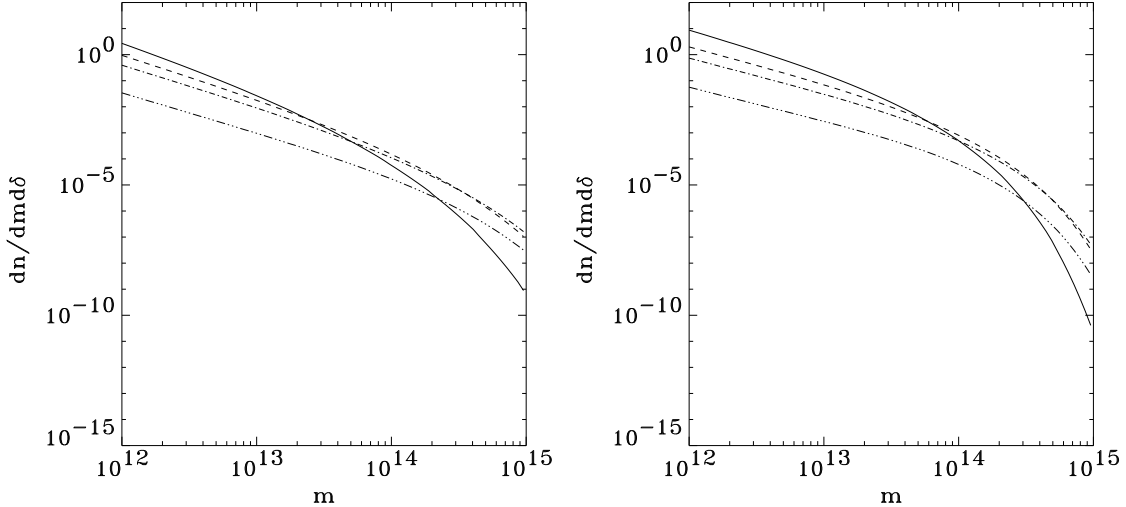


Figure 2.4: Slices of the double distribution function at constant values of δ for $z = 0$, $\beta = 2$ and for $\Omega_m + \Omega_\Lambda = 1$ (left panel) and Einstein-deSitter (right panel) universes. Solid line: $\delta = -0.5$; dashed line: $\delta = 0$; dot-dashed line: $\delta = 0.5$; double-dot-dashed line: $\delta = 3$. The units of the double distribution are number of objects per Mpc^3 per $10^{15} M_\odot$.

to higher δ values with increasing redshift. The significantly more pronounced suppression of this mass scale in high redshifts in the Einstein-deSitter universe is due to the different power-spectrum normalization in the two cosmological models. Because of our choice in the power-spectrum normalization, the exponential suppression in the number density of structures sets in at low masses in the Einstein-de Sitter case than in the concordance universe. Thus, there is a tendency to see more structures of higher mass in our concordance results than in the Einstein-de Sitter case, despite the intuitive expectation that a higher Ω_m universe should have more massive structures at late times due to its ability to continue to form structures even at the present epoch. This would indeed have been the case if the power-spectrum had been normalized in the same way.

That halos of a given mass are more strongly clustered with increasing redshift was also found by [73], who used $\Delta_8(m)$ (the rms overdensity in the number of haloes more massive than some mass scale after smoothing with a spherical top-hat filter of comoving radius $8h^{-1}$ Mpc) as a measure for halo clustering. A tendency of higher

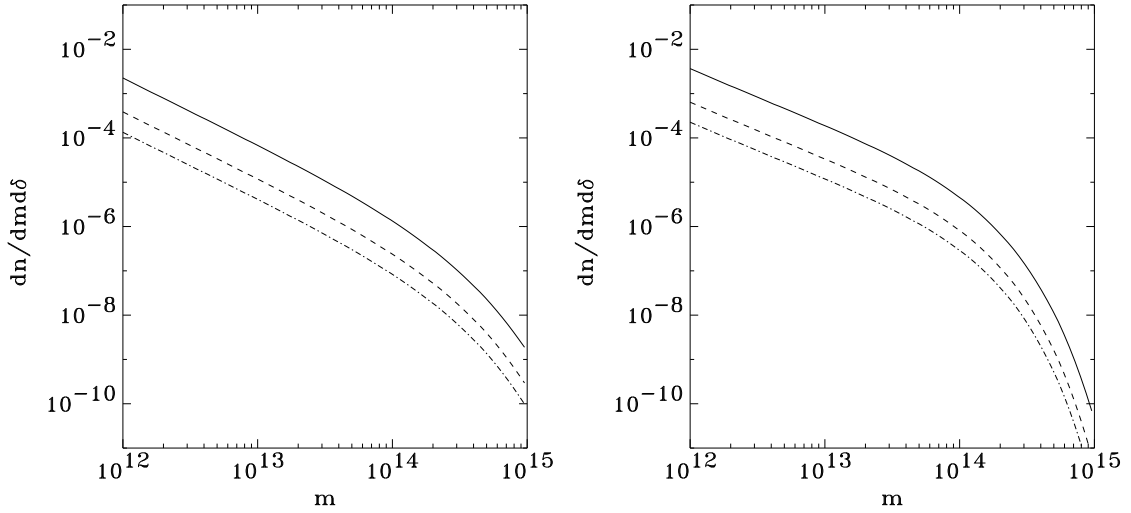


Figure 2.5: Slices of the double distribution function at constant values of δ for $z = 0$, $\beta = 2$, and for $\Omega_m + \Omega_\Lambda = 1$ (left panel) and Einstein-deSitter (right panel) universes. Solid line: $\delta = 10$; dashed line: $\delta = 20$; dot-dashed line: $\delta = 30$. The units of the double distribution are number of objects per Mpc^3 per $10^{15} M_\odot$.

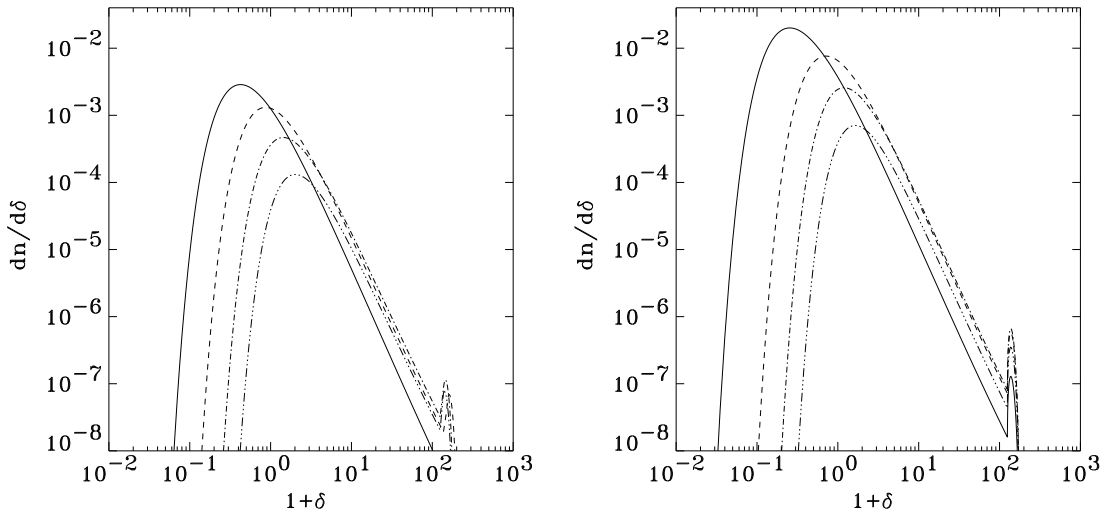


Figure 2.6: Distribution of structures with respect to local density contrast, $dn/d\delta (> 10^{12} M_\odot)$, for $\beta = 2$ and for $\Omega_m + \Omega_\Lambda = 1$ (left panel) and Einstein-deSitter (right panel) universes. Solid line: $z = 0$; dashed line: $z = 1$; dot-dashed line: $z = 2$; double-dot-dashed line: $z = 3$. The units of $dn/d\delta$ are number of objects per Mpc^3 .

mass objects to be found in overdense regions was discussed by [13] and [12], who interpreted it by viewing halos today as progenitors of future larger-scale structures viewed at “high” or “low” redshift.

In addition to the main peak at low $|\delta|$, an additional, much lower and sharper peak can be seen right before the critical overdensity cutoff. This peak is the result of the change of the functional form of the conversion relation between linearly extrapolated and true density contrast close to virialization, when application of the spherical collapse model would lead δ to diverge. The particular shape of the peak is an artifact of the recipe we adopted for dealing with the virialization regime, and carries no physical meaning (the shape of the peak is the shape of the high- δ end of $d\tilde{\delta}/d\delta$). However, since the boundary conditions we use for $\tilde{\delta}(\delta)$ and its derivative *are* physical, we do expect to have some form of local maximum at the high- δ end of the double distribution. Still, as discussed in the previous section, the effect of the details or even the existence of this local maximum on the physical quantities of interest is negligible.

The high- δ cutoff occurs at higher values of δ in the concordance universe than in the Einstein-deSitter universe. This is a result of the different density contrast achieved at virialization by structures in the two different cosmologies. In the Einstein-deSitter case this density contrast is always $18\pi^2$, while in the concordance universe it is always higher and increases with time. At high redshifts, before the effect of Λ becomes significant, δ_c is very close to $18\pi^2$ in the concordance universe as well, as can be seen in Fig. 2.3.

Figures 2.4 and 2.5 show slices of the double distribution at various fixed values of δ , with $z = 0$ and $\beta = 2$. Unlike the constant-mass slices, the constant- δ slices do not exhibit a peak (other than the global maximum imposed by the minimum-mass cutoff). Hence, there does not exist “most probable” mass at each given value of δ . Hence, the hierarchical behavior of the number density of structures seen in the Press-Schechter mass function (which also exhibits no global maximum but instead

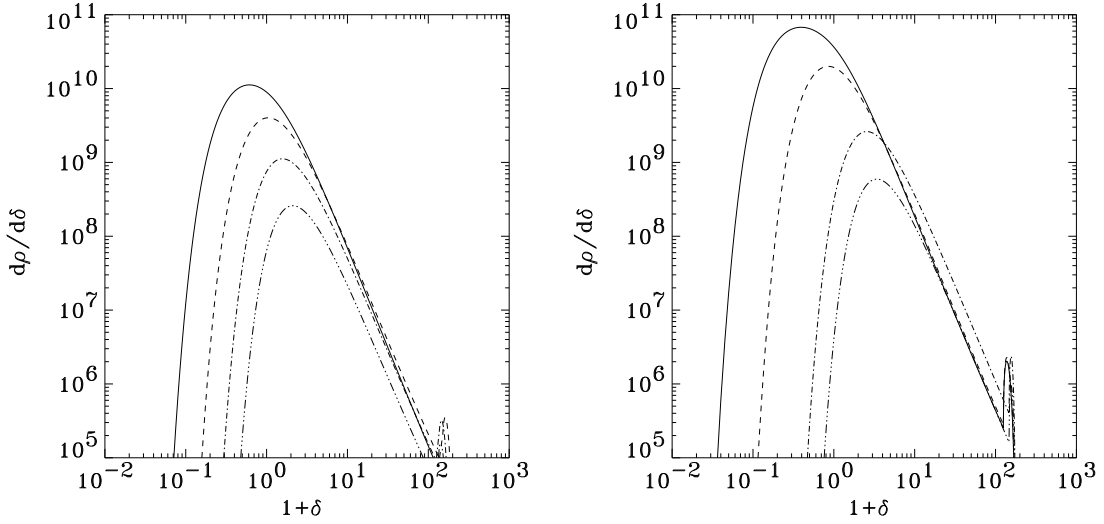


Figure 2.7: Distribution of density of matter inside collapsed structures with respect to local density contrast, $d\rho/d\delta (> 10^{12} M_\odot)$, for $\beta = 2$ and for $\Omega_m + \Omega_\Lambda = 1$ (left panel) and Einstein-deSitter (right panel) universes. Solid line: $z = 0$; dashed line: $z = 1$; dot-dashed line: $z = 2$; double-dot-dashed line: $z = 3$. The units of $d\rho/d\delta$ are M_\odot per Mpc^3 .

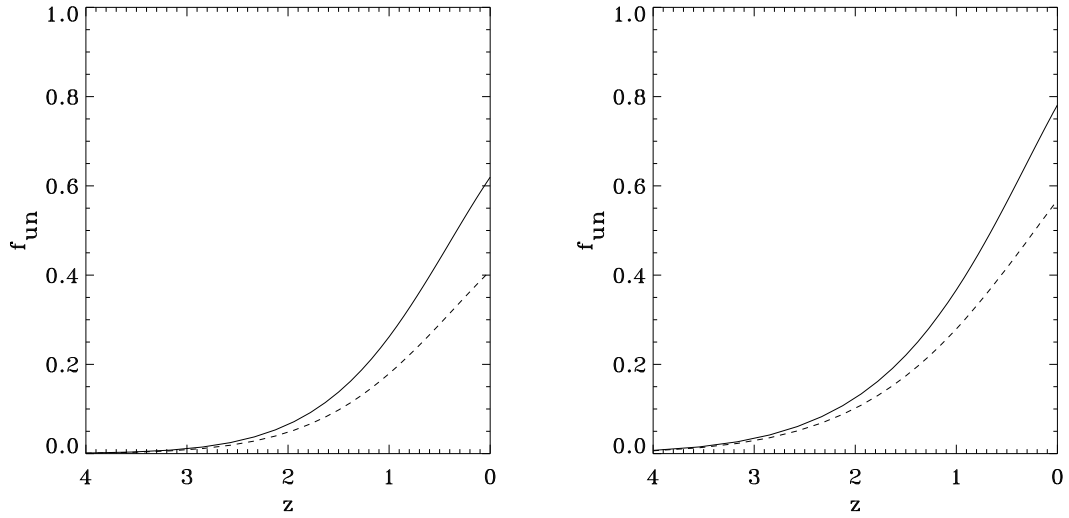


Figure 2.8: Fraction by number $f_{n,un}$ (solid line) and my mass $f_{\rho,un}$ (dashed line) of objects of mass $> 10^{12} M_\odot$ living in underdense regions, as a function of redshift, for $\Omega_m + \Omega_\Lambda = 1$ (left panel) and Einstein-deSitter (right panel) universes.

diverges at low masses) also extends to the constant- δ slices of the double distribution. Figure 2.4 shows slices corresponding to relatively low values of $|\delta|$ ($\delta = -0.5, 0, 0.5$ and 3, close to the distribution peak in δ). At the high-mass end of the distribution, the abundance of objects increases with increasing δ , while in the low mass end of the distribution the trend is reversed, and the object abundance increases with decreasing δ . This is in agreement with the behavior observed in the constant- m slices.

Figure 2.5 shows slices corresponding to high values of δ ($\delta = 10, 20$ and 30), farther from the distribution peak. In this case, the curves do not cross, and an increase of δ simply results in an overall suppression of object abundance: structures of all masses are unlikely to be found overly clustered. This is because the final stages of collapse proceed rather quickly compared to the time spent around turnaround. The likelihood of a region observed in its late stages of collapse but before virialization is then low because the lifetime of this phase is small.

In Fig. 2.6 we plot $dn/d\delta (> 10^{12} M_\odot)$ as a function of $1 + \delta$ for different values of redshift. It is striking that at $z = 0$, the distribution peaks at negative δ values (around $\delta = -0.6$ in the concordance and -0.7 in the Einstein-deSitter universe), indicating that the most probable location for a collapsed object of mass $> 10^{12} M_\odot$ is an *underdense* environment. For the specific mass range, this trend is reversed by $z = 1$, when the preferred location of these objects is close to the universe mean ($\delta = 0$). This time-evolution pattern is independent of cosmology, as it is present both in the concordance and the Einstein-deSitter universes, and appears rather to be a characteristic of the hierarchical nature of structure formation. Parameters of this distribution can be calculated using Eqs. (2.96) and (2.97) which, for the concordance cosmology and $z = 0$ give $\langle \delta \rangle_n = 0.43$ and $\sigma_{\delta,n} = 4.36$. The large value of the variance shows that the distribution is significantly broad. However, the positive value of the mean is an artifact of the asymmetric boundaries of the distribution and its long high- δ tail. This is demonstrated by the notably different locations of the mean and

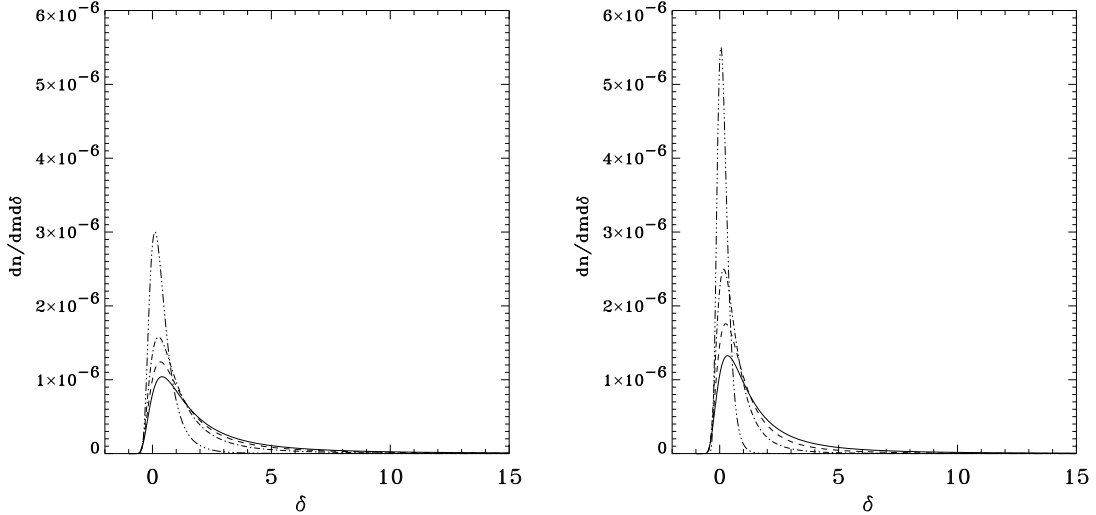


Figure 2.9: Slices of the double distribution function at $m = 5.5 \times 10^{14}, M_\odot$ and for different values of the clustering scale parameter β , for $\Omega_m + \Omega_\Lambda = 1$ (left panel) and Einstein-deSitter (right panel) universes, plotted in linear scale. Solid line: $\beta = 1.5$; dashed line: $\beta = 2$; dot-dashed line: $\beta = 3$; double-dot-dashed line: $\beta = 10$. The units of the double distribution are number of objects per Mpc^3 per $10^{15} M_\odot$.

the median. The value of the latter is $\delta = -0.22$, therefore more structures in this range reside inside underdensities.

Figure 2.7 is the matter-density counterpart of Fig. 2.6, as it shows $d\rho/d\delta (> 10^{12} M_\odot)$ as a function of $1 + \delta$ for the same values of redshift as in Figure 2.6. Again, at the current cosmic epoch, the distribution peaks at negative values of δ . Most of the virialized matter in the universe today appears to reside inside isolated objects rather than in clusters (note that decreasing the value of m_{min} will only enhance this result since the trend towards isolation is more pronounced for the lower-mass objects). The trend of the peak with time (towards larger δ for higher redshifts) is duplicated here as well. In particular, note that at present, a significant fraction of the mass lies in moderately underdense regions. Equations (2.98) and (2.99) give for this distribution (in the concordance cosmology and for $z = 0$), $\langle \delta \rangle_\rho = 1.20$ and $\sigma_{\delta, \rho} = 6.23$. The median of this distribution is at $\delta = 0.20$, a positive value.

Finally, Fig. 2.8 shows the evolution with redshift of the fractions by number and by mass, $f_{n,un}$ and $f_{\rho,un}$, of objects with $m > 10^{12} M_\odot$, living inside underdense

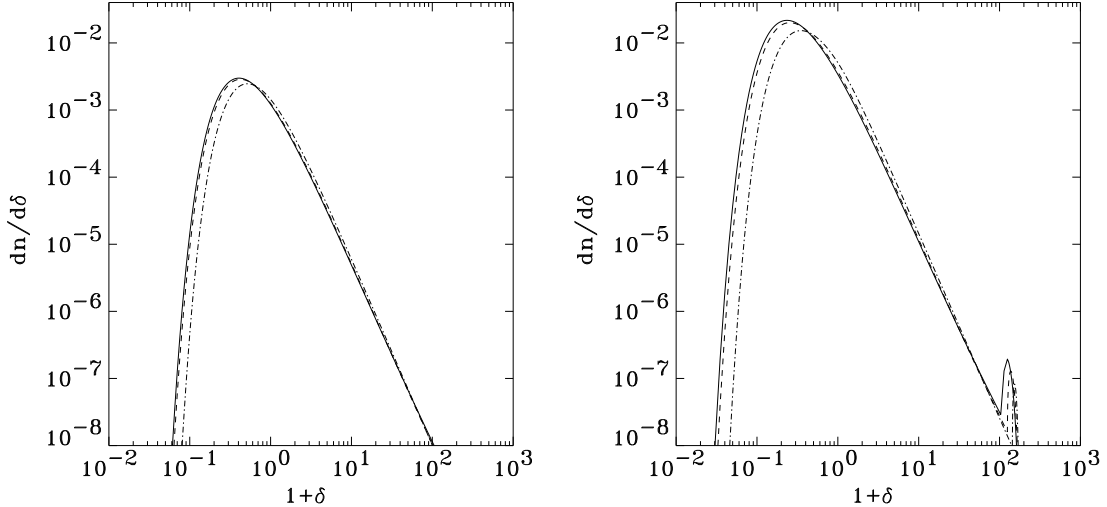


Figure 2.10: Distribution of structures of mass larger than $10^{12} M_\odot$ with respect to local density contrast, $dn/d\delta$, for $\Omega_m + \Omega_\Lambda = 1$ (left panel) and Einstein-deSitter (right panel) universes, at $z = 0$, and for $\beta = 1.5$ (solid line), $\beta = 2$ (dashed line) and $\beta = 10$ (dot-dashed line). The units of $dn/d\delta$ are number of objects per Mpc^3 .

regions. At high redshifts, when the mass of such objects is well above the exponential suppression cutoff, practically none of them are found inside underdensities. This trend is reversed as the redshift decreases. In the $\Omega_m + \Omega_\Lambda = 1$ universe, an equal number of these structures are located inside underdensities by redshift 0.3 and by the current cosmic epoch, about 60% by number (but only 40% by mass) of these structures are located inside underdensities.

Figure 2.9 demonstrates the effect of changing the clustering scale parameter on the double distribution. Slices of the double distribution along $m = 5.5 \times 10^{14} M_\odot$ are plotted (in linear axes) as a function of δ , and for $\beta = 1.5$ (solid line), 2 (dashed line), 3 (dot-dashed line) and 10 (double-dot-dashed line). The location of the peak appears to be extremely insensitive to the value of β for moderately low values. It very slowly moves towards $\delta = 0$ with increasing β , as it should (increasing β results in averaging the overdensity over increasingly large volumes). Note that even as β approaches 1, the peak will *not* move towards δ_c , as a result of our correction for the central-object contamination. This makes our formalism particularly suitable to

study the properties of matter very close but outside a virialized structure (e.g. the local density of accreted gas).

The effect of β on an integral quantity is shown in Fig. 2.10, which shows $dn/d\delta(>10^{12}M_{\odot})$ for $\beta = 1.5$ (solid line), $\beta = 2$ (dashed line) and $\beta = 10$ (dot-dashed line). Again, the results are extremely insensitive to the value of β , which gives us confidence about the robustness of the location of the peak of our distributions.

As we have seen in this section, the correlations between the mass of collapsed structures and their environmental conditions are not only non-trivial, but also evolve dramatically with cosmic epoch (for a wide range of masses, the most probable δ changes sign between redshifts of zero and a few). It would therefore be desirable and of high interest to use the double distribution to investigate the effect of the environment on systems and phenomena the properties of which depend sensitively on the state of their surrounding space and matter. In the next chapter, we will use the environmental information encoded in the double distribution to assess the effect of the environmental factor on an important aspect of cosmic structure formation: cosmic accretion shocks.

Chapter 3

Cosmic Accretion Shocks

3.1 Overview

In this chapter, we utilize the double distribution of dark matter halos which we derived and studied in the previous chapter, to study the effect of the environmental factor on the statistical properties of cosmic accretion shocks. In order to explicitly distinguish between effects of the environment and effects of the underlying distribution of accretor masses, we explore two variations of our model. In the first, all collapsed cosmic structures are assumed to live in a similar environment. The properties of the accretion shock surrounding each such structure is then simply determined by the mass of the structure and the redshift of interest. The mass function of collapsed structures is, in this case, the Press-Schechter mass function. In the context of the second model, the distribution of collapsed structures with respect to both mass and environment is described by the double distribution. The properties of the accretion shock around each structure depends both on the mass of the structure as well as the environment of the structure (whether the structure resides inside an underdensity or an overdensity).

The formalism describing the properties of a single accretion shock around a cosmic structure is presented in section 3.2. The Mach number of the accretion shock

surrounding each collapsed object is derived from the temperature jump across the shock. The temperature of the gas behind the shock is simply taken to be the virial temperature of the collapsed object. The temperature ahead of the shock depends on the model used each time. For the Press-Schechter-based model, it is simply the mean temperature of the intergalactic medium at the epoch under consideration¹. For the double-distribution-based model, the temperature also depends on the density of the environment of the collapsed structure. The deviation from the mean intergalactic medium temperature is calculated by assuming that it is only due to adiabatic heating (cooling) because of the relative local (de)compression with respect to the cosmic mean density. Once the Mach number of the accretion shock has been determined, the accretion velocity (in the shock frame) is then calculated from it, and used to derive properties of the structure such as the accreted mass current and the kinetic energy crossing the shock surface per unit time.

Combining the properties of a single shock with an underlying distribution of accretors (either the Press-Schechter mass function or the double distribution of cosmic structures), in section 3.3 we derive the statistical properties of the population accretion shocks. The calculated quantities include the distribution of accretor number density, accretor mass, shock surface, mass current, and kinetic power crossing the shocks, with respect to accretion shock Mach number. In addition, we calculate the cosmic history of the kinetic power and of the mass current integrated over shock Mach number, as well as the cumulative kinetic energy and number of baryons which have been processed through accretion shocks by each redshift.

Our results are presented in section 3.4. We find that the shock environment alters the physical impact of shocks on the intergalactic medium, as well as the

¹Although we include the effect of reionization (the cosmic epochs we consider are post-reionization and we take the temperature of the diffuse intergalactic gas at a density equal to the cosmic mean to be $\sim 10^4$ K), we do not include filament preheating in our models. Hence, we treat all accretion shocks as external shocks.

cosmic history of the shock population. The most prominent environmental effect is the development, at low redshifts, of a natural bi-modality in the distribution, with respect to shock Mach number, of the kinetic power crossing accretion shocks. Concerning the physical impact of shocks on the intergalactic medium, we find that the cumulative energy input of accretion shocks by redshift ~ 3 is comparable to the energy required to reionize the universe. In addition, more than a third of all baryons in the universe have been shocked in accretion processes by the present cosmic epoch. Finally, we comment on the components of the shock populations found in cosmological simulations [61; 63] with which our models are directly comparable.

3.2 Properties of a single shock

Throughout this chapter, we assume an adiabatic equation of state, and we consider all shocks to be non-radiative. We also assume that any individual collapsed object as well as its accretion shock are spherically symmetric. We will take the accretion shock position around each structure to coincide with the virial radius of each structure.

The Mach number of a shock, \mathcal{M} , is defined as the ratio of the velocity of the accreted material in the shock frame to the adiabatic sound speed of the accreted material. The Mach number is related to the temperature jump across the shock through [74]

$$\frac{T_2}{T_1} = \frac{[2\gamma\mathcal{M}^2 - \gamma + 1][(1/\gamma - 1)\mathcal{M}^2 + 2]}{(\gamma + 1)^2\mathcal{M}^2} \quad (3.1)$$

where T_1 and T_2 are the pre-shock and post-shock temperatures correspondingly, and γ is the ratio of specific heats (assuming that this remains constant across the shock). For a $\gamma = 5/3$ gas, Eq. (3.1) becomes

$$\frac{T_2}{T_1} = \frac{(5\mathcal{M}^2 - 1)(\mathcal{M}^2 + 3)}{16\mathcal{M}^2}. \quad (3.2)$$

In the limit $\mathcal{M} \gg 1$ this equation is further simplified,

$$\mathcal{M} = \sqrt{\frac{16}{5} \frac{T_2}{T_1}}. \quad (3.3)$$

The pre-shock temperature can be written in terms of the adiabatic sound speed of the pre-shock material c_{s1} ,

$$kT_1 = \frac{\mu m_p}{\gamma} c_{s1}^2, \quad (3.4)$$

where μ is the mean molecular weight of the accreted gas, and m_p is the proton mass.

If we also take T_2 to be the virial temperature of the accreting structure,

$$T_2 = T_{\text{vir}} = \frac{\mu m_p}{k} \frac{G m^{2/3} (4\pi f_c \rho_{m,0})^{1/3} (1+z)}{3^{1/3} 5}, \quad (3.5)$$

then the ratio T_2/T_1 becomes

$$\begin{aligned} \frac{T_2(m, z)}{T_1} &= \frac{T_{\text{vir}}(m, z)}{T_1} \\ &= 2.7 \times 10^3 \Omega_m \left(\frac{f_c}{18\pi^2} \right)^{1/3} (1+z) \\ &\quad \times \left(\frac{m}{m_8} \right)^{2/3} \left(\frac{15 \text{ km s}^{-1}}{c_{s1}} \right)^2, \end{aligned} \quad (3.6)$$

where m is the object mass, $f_c = \rho_{\text{vir}}/\rho_m$ is the compression factor for a virialized object (which may vary with virialization redshift, depending on the cosmological model), z is the virialization redshift, h is the dimensionless Hubble parameter, and $m_8 = 5.96 \times 10^{14} h^{-1} \Omega_m M_\odot$ is the mass included in a sphere of radius $r_8 = 8h^{-1} \text{ Mpc}$ assuming the mean matter density inside the sphere to be equal to the cosmic mean.

In Appendix D we compare this result with the Bertschinger similarity solution for an $\Omega_m = 1$ universe [59], and we find it to be in excellent agreement in the high- \mathcal{M} regime, where the Bertschinger solution is applicable.

The surface area of a spherical shock around a structure of mass m is

$$S_1(m) = 4\pi r_v(m, z)^2 \quad (3.7)$$

where r_v is the virial radius of the structure,

$$\begin{aligned} r_v &= 1.4h^{-1} \text{Mpc} \times \\ &\left(\frac{m}{m_8} \right)^{1/3} \left(\frac{f_c}{18\pi^2} \right)^{-1/3} (1+z)^{-1}. \end{aligned} \quad (3.8)$$

The mass current, defined as the rate at which mass crosses the surface of a single accretion shock around a structure of mass m at an epoch z , is

$$\begin{aligned} J_1 &= \frac{dm}{dt} = 4\pi r_v^2(m) v_1 \rho_b(z) (1 + \delta_s) \\ &= 4\pi r_v^2(m) \Omega_b \rho_c(z) (1 + \delta_s) \mathcal{M} c_{s,1} \end{aligned} \quad (3.9)$$

where ρ_b is the cosmic baryon density at the epoch of interest and $(1 + \delta_s)$ is the density enhancement (with respect to the cosmic mean) just outside the shock.

Finally, the kinetic power crossing the accretion shock around a single structure of mass m is

$$P_1 = \frac{dE}{dt} = \frac{1}{2} \frac{dm}{dt} v_1^2 = \frac{1}{2} J_1 v_1^2. \quad (3.10)$$

Hence,

$$P_1 = 2\pi r_v(m)^2 \Omega_b \rho_c(z) (1 + \delta_s) \mathcal{M}^3 c_{s,1}^3. \quad (3.11)$$

3.3 Properties of the population of Cosmic Accretion Shocks

The quantities we will use to describe the statistical properties of the population of cosmic accretion shocks are:

- The “number distribution” of shocks with respect to Mach number. This is defined as the distribution of the comoving number density of accreting structures per logarithmic Mach number interval of their respective accretion shocks,

$$\frac{dn}{d \ln \mathcal{M}} = \mathcal{M} \frac{dn}{d \mathcal{M}}, \quad (3.12)$$

with units number of structures per comoving Mpc^3 .

- The “surface distribution” with respect to Mach number. This is defined as the shock surface area per logarithmic Mach number interval per comoving volume under consideration,

$$\frac{dS}{d \ln \mathcal{M}} = \mathcal{M} \frac{dS}{d\mathcal{M}} \quad (3.13)$$

with units of Mpc^{-1} (since it represents a ratio of shock surface over space volume).

- The “accretor mass” distribution of shocks with respect to Mach number. This is defined as the distribution of the comoving mass density in accreting structures per logarithmic Mach number interval of their respective accretion shocks,

$$\frac{d\rho}{d \ln \mathcal{M}} = \mathcal{M} \frac{d\rho}{d\mathcal{M}}, \quad (3.14)$$

with units of M_\odot per comoving Mpc^3 .

- The “mass current distribution” with respect to Mach number. This is defined as the comoving mass current density crossing shock surfaces of logarithmic Mach number between $\ln \mathcal{M}$ and $\ln \mathcal{M} + d \ln \mathcal{M}$,

$$\frac{dJ}{d \ln \mathcal{M}} = \mathcal{M} \frac{dJ}{d\mathcal{M}} \quad (3.15)$$

with units of $\text{M}_\odot \text{yr}^{-1} \text{Mpc}^{-3}$.

- The “integrated mass current”, J , which is the comoving mass current density crossing shock surfaces of any Mach number at a given cosmic epoch, with units of $\text{M}_\odot \text{yr}^{-1} \text{Mpc}^{-3}$.
- the “cumulative processed mass”, $\int_{t_i}^t J dt$, which is the total mass density processed by shocks of any Mach number since some initial epoch t_i , expressed as a non-dimensional shocked baryon fraction.

- The “kinetic power distribution” with respect to Mach number. This is defined as the comoving kinetic power density crossing shock surfaces of logarithmic Mach number between $\ln \mathcal{M}$ and $\ln \mathcal{M} + d \ln \mathcal{M}$,

$$\frac{dP}{d \ln \mathcal{M}} = \mathcal{M} \frac{dP}{d \mathcal{M}} \quad (3.16)$$

with units $\text{erg s}^{-1} \text{ Mpc}^{-3}$.

- The “integrated kinetic power”, P , which is the comoving kinetic power density crossing shock surfaces of any Mach number at a given cosmic epoch, with units of $\text{erg s}^{-1} \text{ Mpc}^{-3}$.
- The “cumulative processed kinetic energy”, $\int_{t_i}^t P dt$, which is the total kinetic energy density processed by shocks of any Mach number since some initial cosmic epoch t_i , with units of eV per baryon in the universe.

In order to explicitly identify the environmental effects on the statistical properties of accretion shocks, we will use two different models to calculate these quantities. The first will assume that all structures are accreting gas of a single temperature, and that the population of accreting objects is well described by the Press-Schechter mass function. In this case, there exists a one-to-one correspondence between accretor mass and Mach number of the associated accretion shock.

The second model assumes that the accreted gas has a distribution of densities and hence temperatures (where adiabatic heating and cooling are assumed to calculate the relation between local density and temperature). The distribution of accretors with respect to both mass and local over-(or under-)density is described by the double distribution of cosmic structures. In this case, there is a distribution of possible Mach numbers for the accretion shock around a structure of a given mass, depending on the local overdensity of the accreted material.

Features of our results exclusive to the second model will then be an effect of the environment in which accreting structures reside.

3.3.1 Accreted Material of a Single Temperature

If we assume that all collapsed objects accrete baryons of a single temperature, then at a given redshift, all objects with an accretion shock of a given Mach number will have the same mass,

$$\begin{aligned}
m = m(\mathcal{M}, z) = & 4.2 \times 10^9 h^{-1} \text{M}_\odot \times \\
& \left(\frac{18\pi^2}{\Omega_m f_c} \right)^{1/2} \left(\frac{c_s}{15 \text{ km s}^{-1}} \right)^3 \times \\
& \left[\frac{(5\mathcal{M}^2 - 1)(\mathcal{M}^2 + 3)}{16\mathcal{M}^2} \right]^{3/2} (1 + z)^{-3/2}.
\end{aligned} \tag{3.17}$$

We will also assume that the mass distribution of collapsed objects can be described by the Press-Schechter mass function [1; 3]

$$\frac{dn}{dm}(m, z) = \sqrt{\frac{2}{\pi}} \frac{\rho_{m,0}}{m^2} \left| \frac{d \ln \sigma}{d \ln m} \right| \exp \left\{ -\frac{\left[\tilde{\delta}_c(z) \right]^2}{2 [\sigma(m)]^2} \right\} \tag{3.18}$$

where $\tilde{\delta}_c(z)$ is the linearly extrapolated overdensity of an object which collapses at redshift z , $\sigma(m)$ is the square root of the variance of the linearly extrapolated field smoothed at a mass scale m , and $\rho_{m,0}$ is the cosmic mean matter density at the present time.

In this case, the statistical quantities describing the population of accretion shocks can be derived in a straight forward way. The number distribution of shocks with respect to Mach number is

$$\frac{dn(\mathcal{M}, z)}{d \ln \mathcal{M}} = \mathcal{M} \frac{dn}{dm} [m(\mathcal{M}, z), z] \frac{\partial m}{\partial \mathcal{M}}(\mathcal{M}, z) \tag{3.19}$$

where $m = m(\mathcal{M}, z)$ is given by Eq. (3.17).

Similarly, the surface distribution with respect to Mach number is

$$\frac{dS}{d \ln \mathcal{M}} = \mathcal{M} \frac{dn}{dm} 4\pi r_v^2 \left. \frac{\partial m}{\partial \mathcal{M}} \right|_z \tag{3.20}$$

while the accretor mass distribution is

$$\frac{d\rho}{d\ln\mathcal{M}} = \mathcal{M} m \frac{dn}{dm} \frac{\partial m}{\partial\mathcal{M}} \Big|_z. \quad (3.21)$$

The mass current distribution in this model becomes

$$\frac{dJ}{d\ln\mathcal{M}}(\mathcal{M}, z) = \mathcal{M} \frac{dn}{dm} \frac{\partial m}{\partial\mathcal{M}} \Big|_z J_1, \quad (3.22)$$

where $J_1(\mathcal{M}, z)$ is given by Eq. (3.9) with $\delta_s = 3.13$ (the overdensity factor in the Bertschinger solution (see Appendix D) just outside the shock), while the integrated mass current is

$$J(z) = \int_{\mathcal{M}=1}^{\infty} \mathcal{M} \frac{dn}{dm} \frac{\partial m}{\partial\mathcal{M}} \Big|_z J_1 d\mathcal{M}, \quad (3.23)$$

and the cumulative processed mass is

$$\int_{t_i}^{t_0} J dt = \int_{t_i}^{t_0} \int_{\mathcal{M}=1}^{\infty} \mathcal{M} \frac{dn}{dm} \frac{\partial m}{\partial\mathcal{M}} \Big|_z J_1 d\mathcal{M} dt, \quad (3.24)$$

which, in a concordance cosmology becomes

$$\begin{aligned} & \int_{t_i}^{t_0} J dt = \\ & \frac{1}{H_0} \int_0^{z_i} \int_{\mathcal{M}=1}^{\infty} \frac{dn}{dm} \frac{\partial m}{\partial\mathcal{M}} \Big|_z \frac{J_1 dz d\mathcal{M}}{(1+z)\sqrt{\Omega_\Lambda + \Omega_m(1+z)^3}}, \end{aligned} \quad (3.25)$$

where H_0 is the Hubble parameter and z_i is the redshift corresponding to time t_i . We use $z_i = 10$.

Finally, the kinetic power distribution is

$$\frac{dP}{d\ln\mathcal{M}}(\mathcal{M}, z) = \mathcal{M} \frac{dn}{dm} \frac{\partial m}{\partial\mathcal{M}} \Big|_z P_1 \quad (3.26)$$

where $P_1(\mathcal{M}, z)$ is given by Eq. (3.10), while the integrated kinetic power is

$$P(z) = \int_{\mathcal{M}=1}^{\infty} \mathcal{M} \frac{dn}{dm} \frac{\partial m}{\partial\mathcal{M}} \Big|_z P_1 d\mathcal{M}, \quad (3.27)$$

and the cumulative processed kinetic energy is

$$\int_{t_i}^{t_0} P dt = \frac{1}{H_0} \int_0^{z_i} \int_{\mathcal{M}=1}^{\infty} \frac{dn}{dm} \frac{\partial m}{\partial \mathcal{M}} \Big|_z \frac{P_1 dz d\mathcal{M}}{(1+z)\sqrt{\Omega_\Lambda + \Omega_m(1+z)^3}}. \quad (3.28)$$

3.3.2 Accreted Material of Varying Temperature

In the second variation of our model, we wish to relax the assumption that the temperature of the accreted material is the same for all structures. Assuming that adiabatic heating or cooling is the only process that causes deviations of the temperature of the gas outside collapsed structures from its mean value, we can relate the local sound speed, c_s , to the local overdensity or underdensity, δ , where

$$\delta = \frac{\rho_{\text{local}} - \rho_m}{\rho_m}. \quad (3.29)$$

Since for adiabatic heating and cooling $c_s^2 \propto \rho_{\text{local}}^{\gamma-1}$, we get

$$c_s = c_{s,\text{avg}} (\delta + 1)^{(\gamma-1)/2}, \quad (3.30)$$

where $c_{s,\text{avg}}$ is the “cosmic average” sound speed (the sound speed of the intergalactic medium at a density equal to the cosmic mean at the epoch of interest). This formalism can accommodate the case where a process (such as reionization) heats the universe almost homogeneously, therefore increasing the average temperature (and consequently the cosmic average sound speed $c_{s,\text{avg}}$).

In order to make further progress and be able to calculate measures of the statistical properties of the population shocks in this approximation, we need an analytical model for the *environment* of collapsed structures. For this purpose, we will use the double distribution (DD) of collapsed structures with respect to mass and local overdensity which we derived and studied in the previous chapter. In the context of the double distribution, we defined the “local environment” of a collapsed structure

through the *clustering scale parameter*, β . The clustering scale parameter is a free parameter in the DD model, and is defined so that the “environment” of an object of mass m be a surrounding region in space which encompasses mass βm . The double distribution was found to be given by Eq. (2.22).

In Eq. (2.22), $\tilde{\delta}_\ell$ is the local linearly extrapolated overdensity (or underdensity), which is related to the true (calculated from the spherical evolution model) overdensity of the environment sphere *including the local object*, δ_ℓ through the exact relations given in chapter 2, or through the useful approximation represented by Eq. (2.83), which is accurate at a better than 2% level throughout its domain for all cosmologies of interest.

Because in the problem of cosmic accretion shocks we are interested in the properties (density and sound speed) of the material right outside the shock surface, we will adopt a small value for the clustering scale parameter, $\beta = 1.1$. Our results, however, are not sensitive to the exact value of β since, as we saw in chapter 2, the properties of the double distribution (when calculated as a function of δ rather than δ_ℓ) depend very mildly on β for small values of β .

Distribution of Sound Speeds

From the double distribution and Eq. (3.30), we can immediately calculate the number density of collapsed objects of mass $m > m_{\min}$ embedded in a medium of local sound speed between c_s and $c_s + dc_s$,

$$\frac{dn}{dc_s} dc_s = dc_s \frac{d\delta}{dc_s} \int_{m=m_{\min}}^{\infty} \frac{dn}{dm d\delta} dm, \quad (3.31)$$

Similarly, the density of matter in collapsed objects of mass $> m_{\min}$ embedded in a medium of local sound speed between c_s and $c_s + dc_s$ is

$$\frac{d\rho}{dc_s} dc_s = dc_s \frac{d\delta}{dc_s} \int_{m=m_{\min}}^{\infty} m \frac{dn}{dm d\delta} dm. \quad (3.32)$$

In Eqs. (3.31) and (3.32), $d\delta/dc_s$ can be found from Eq. (3.30),

$$\frac{d\delta}{dc_s} = \frac{2}{\gamma-1} \frac{1}{c_{s,\text{avg}}} \left(\frac{c_s}{c_{s,\text{avg}}} \right)^{\frac{3-\gamma}{\gamma-1}}. \quad (3.33)$$

Hence, if we use C_s to denote the sound speed in units of the cosmic average sound speed,

$$C_s \equiv \frac{c_s}{c_{s,\text{avg}}}, \quad (3.34)$$

Eq. (3.31) becomes

$$\frac{dn}{dC_s} = \frac{2}{\gamma-1} C_s^{\frac{3-\gamma}{\gamma-1}} \int_{m=m_{\min}}^{\infty} \frac{dn}{dm d\delta} dm, \quad (3.35)$$

and Eq. (3.32) becomes

$$\frac{d\rho}{dC_s} = \frac{2}{\gamma-1} C_s^{\frac{3-\gamma}{\gamma-1}} \int_{m=m_{\min}}^{\infty} m \frac{dn}{dm d\delta} dm. \quad (3.36)$$

Shock Properties

In this second variation of our model, the mass of a collapsed object with an associated accretion shock of Mach \mathcal{M} is also dependent on the local overdensity δ ,

$$\begin{aligned} m = m(\mathcal{M}, \delta, z) = & 4.2 \times 10^9 h^{-1} \text{M}_\odot \left(\frac{18\pi^2}{f_c \Omega_m} \right)^{1/2} \times \\ & \left(\frac{c_{s,\text{avg}}}{15 \text{ km s}^{-1}} \right)^3 (\delta + 1)^{3(\gamma-1)/2} \times \\ & \left[\frac{(5\mathcal{M}^2 - 1)(\mathcal{M}^2 + 3)}{16\mathcal{M}^2} \right]^{3/2} (1 + z)^{-3/2}. \end{aligned} \quad (3.37)$$

Note that, when $\delta = 0$, this equation is reduced to Eq. (3.17), as it should.

Hence, the number distribution of shocks with respect to Mach number is

$$\frac{dn}{d \ln \mathcal{M}} = \mathcal{M} \int_{\delta=-1}^{\delta_c} d\delta \frac{dn}{dm d\delta} [m(\mathcal{M}, \delta, z), \delta, z] \left. \frac{\partial m}{\partial \mathcal{M}} \right|_{\delta, z} \quad (3.38)$$

where $m(\mathcal{M}, \delta, z)$ is given by Eq. (3.37).

Similarly, the surface distribution with respect to Mach number is

$$\frac{dS}{d \ln \mathcal{M}} = \mathcal{M} \int_{\delta=-1}^{\delta_c} d\delta 4\pi r_v^2 \frac{dn}{dmd\delta} \frac{\partial m}{\partial \mathcal{M}} \Big|_{\delta,z}, \quad (3.39)$$

while the accretor mass distribution is

$$\frac{d\rho}{d \ln \mathcal{M}} = \mathcal{M} \int_{\delta=-1}^{\delta_c} d\delta m \frac{dn}{dmd\delta} \frac{\partial m}{\partial \mathcal{M}} \Big|_{\delta,z}. \quad (3.40)$$

The mass current distribution is

$$\frac{dJ}{d \ln \mathcal{M}} = \mathcal{M} \int_{\delta=-1}^{\delta_c} d\delta J_1 \frac{dn}{dmd\delta} \frac{\partial m}{\partial \mathcal{M}} \Big|_{\delta,z}, \quad (3.41)$$

where $J_1(\mathcal{M}, \delta, z)$ given by Eq. (3.9). In this case, $\delta_s = \delta$, the local overdensity outside the shock as given by the DD. The integrated mass current is then

$$J(z) = \int_{\mathcal{M}=1}^{\infty} \int_{\delta=-1}^{\delta_c} d\mathcal{M} d\delta J_1 \frac{dn}{dmd\delta} \frac{\partial m}{\partial \mathcal{M}} \Big|_{\delta,z}, \quad (3.42)$$

and the cumulative processed mass is

$$\begin{aligned} & \int_{t_i}^{t_0} J dt = \\ & \int_{z_1}^0 \int_{\mathcal{M}=1}^{\infty} \int_{-1}^{\delta_c} \frac{d\mathcal{M} d\delta dz J_1 \frac{dn}{dmd\delta} \frac{\partial m}{\partial \mathcal{M}} \Big|_{\delta,z}}{H_0(1+z)\sqrt{\Omega_\Lambda + \Omega_m(1+z)^3}}. \end{aligned} \quad (3.43)$$

Finally, the kinetic power distribution is

$$\frac{dP}{d \ln \mathcal{M}} = \mathcal{M} \int_{\delta=-1}^{\delta_c} d\delta P_1 \frac{dn}{dmd\delta} \frac{\partial m}{\partial \mathcal{M}} \Big|_{\delta,z}, \quad (3.44)$$

with $P_1(\mathcal{M}, \delta, z)$ given by Eq. (3.10), while the integrated kinetic power is

$$P(z) = \int_{\mathcal{M}=1}^{\infty} \int_{\delta=-1}^{\delta_c} d\mathcal{M} d\delta P_1 \frac{dn}{dmd\delta} \frac{\partial m}{\partial \mathcal{M}} \Big|_{\delta,z}, \quad (3.45)$$

and the cumulative processed kinetic energy is

$$\begin{aligned} & \int_{t_i}^{t_0} P dt = \\ & \int_{z_1}^0 \int_{\mathcal{M}=1}^{\infty} \int_{-1}^{\delta_c} \frac{d\mathcal{M} d\delta dz P_1 \frac{dn}{dmd\delta} \frac{\partial m}{\partial \mathcal{M}} \Big|_{\delta,z}}{H_0(1+z)\sqrt{\Omega_\Lambda + \Omega_m(1+z)^3}}. \end{aligned} \quad (3.46)$$

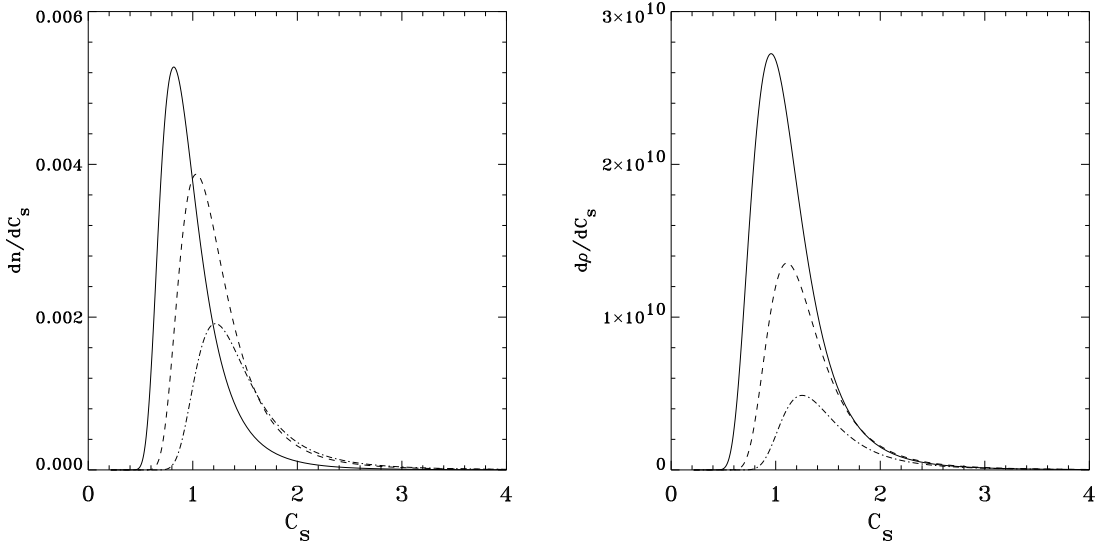


Figure 3.1: Distribution of number of objects (left panel, in units of objects per comoving Mpc^3) and mass density (right panel, in units of $\text{M}_\odot \text{Mpc}^{-3}$) per C_s interval, for objects with mass $> 10^{12} \text{ M}_\odot$, in a WMAP concordance universe. Solid line: $z = 0$; dashed line: $z = 1$; dot-dashed line: $z = 2$.

3.4 Results

3.4.1 Distribution of Environmental Sound Speeds

In Fig. 3.1 we plot the distribution of sound speeds of the material in which collapsed objects of mass greater than 10^{12} M_\odot are embedded, for different redshifts. The left panel shows the comoving number density of objects per interval of the dimensionless sound speed C_s , dn/dC_s , and the right panel shows the mass-density counterpart $d\rho/dC_s$. All curves correspond to a concordance *Wilkinson Microwave Anisotropy Probe* (WMAP) universe ($\sigma_8 = 0.84$, $h = 0.71$, $\Omega_m = 0.27$ and $\Omega_b = 0.04$, [24]). As expected from the results of chapter 2, which show that the most probable density contrast of the material surrounding collapsed structures decreases with time, the most probable sound speed of the material surrounding collapsed structures of mass $> 10^{12} \text{ M}_\odot$ increases with redshift. The overall suppression of the curves with increasing redshift is due to the fact that fewer structures more massive than a fixed cutoff have had enough time to collapse at large redshifts. At the present epoch, the

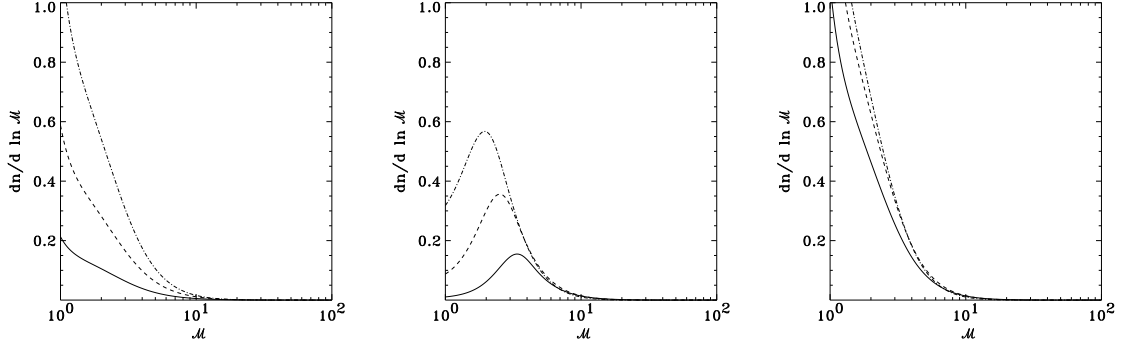


Figure 3.2: Number distribution of shocks per logarithmic Mach number interval for the Press-Schechter-based model (left panel) and the double-distribution-based models (middle and right panels). The middle panel models implement a halo mass cutoff identical to that of the Press-Schechter case, while the right panel model assumes no mass cutoff. The units of the vertical axes are number of objects per comoving Mpc^3 . Solid line: $z = 0$; dashed line: $z = 1$; dot-dashed line: $z = 2$.

most probable sound speed for the masses under consideration is only a fraction of the cosmic average sound speed, due to the fact that structures in this range of masses are more likely to be found inside underdensities. Note however that the picture presented here is incomplete, as shock heating in filaments will further modify the sound speed distribution, favoring higher values of the sound speed.

3.4.2 Properties of Accretion Shocks: Effects of the Local Environment

In this section we again assume a WMAP concordance universe. We focus on post-reionization redshifts, hence we assume a cosmic average sound speed of 15 km/s, corresponding to a temperature of $\sim 10^4 \text{ K}$, for a fully ionized plasma with $\mu = 0.59$ (25% He by mass).

In Fig. 3.2 we plot the number distribution of shocks with respect to Mach number, $dn/d \ln \mathcal{M}$, for the Press-Schechter-based (hereafter PS) model (left panel) and two implementations of the double-distribution-based (hereafter DD) model (middle and right panel).

The distribution in the PS model monotonically increases for decreasing \mathcal{M} since as we have discussed in this case there is a one-to-one correspondence between mass and Mach number, hence the number distribution of shocks simply follows the Press-Schechter mass function. The requirement $\mathcal{M} \geq 1$ imposes then a cutoff in the mass of the dark matter halos that can act as a host to an accretion shocks. This mass cutoff is the mass of the object whose virial temperature exactly equals the temperature of the diffuse gas, and it is $m_{\min} = 8.1 \times 10^9 M_{\odot}$ at $z = 0$, $m_{\min} = 3.8 \times 10^9 M_{\odot}$ at $z = 1$ and $m_{\min} = 2.2 \times 10^9 M_{\odot}$ at $z = 2$. The decrease of m_{\min} with increasing redshift is due to the fact that the virial temperature of an object of a fixed mass is larger if the object virializes at high redshift than if it virialized today. In an Einstein-deSitter Universe this is a simple result of the higher cosmic matter density in the past (the compression factor of a virialized object is constant in time, so since the cosmic density is larger in the past, the virial density which is the compression factor times the cosmic density is also larger in the past, resulting to a higher virial temperature). In the concordance universe, there are two competing factors mediating this effect. The cosmic matter density is still larger in the past, however the compression factor is now itself redshift-dependent, and increases with decreasing redshift. However, this increase of the compression factor is not steep enough to counteract the decrease in cosmic density, and still the virial density decreases with decreasing virialization redshift.

The middle panel of Fig. 3.2 shows a variation of our DD model which includes only objects of a mass larger than the mass cutoff of the PS model in the corresponding redshift. The mass cutoff, in combination with the double-distribution-imposed distribution of pre-shock sound speeds for each accretor mass, results in a \mathcal{M} number distribution which peaks at $\mathcal{M} \lesssim 4$, a position which is defined by the combination of the virial temperature at the mass cutoff (which is the most populated available mass bin) and the sound speed corresponding to the most probable environment (as

given by the double distribution) at that particular mass. If the additional constraint $\mathcal{M} \geq 1$ did not exist, then the area below the curves corresponding to the same redshift in the left and middle panels would be the same, as it would represent simply the total number of objects with mass larger than the mass cutoff. However, some of these objects are “lost” in the double distribution model because they are embedded in material of temperature equal or larger than their virial temperature and hence they cannot harbor shocks. This effect is more pronounced at higher redshifts, while at $z = 0$ where very few objects are “lost” from the distribution as described above, the areas below the two solid lines in the left and middle panels are almost equal.

The right panel of Fig. 3.2 shows the DD model where the only restriction in the participating objects is the requirement that $\mathcal{M} \geq 1$. In this case, the distribution does not turn over, and it is in fact at an overall higher level than the corresponding PS model. This is because the DD model tends to move smaller objects to higher \mathcal{M} bins, because in the double-distribution picture smaller objects preferentially reside inside underdense regions. Therefore, smaller objects accrete cooler gas and harbor shocks of higher \mathcal{M} than in the Press-Schechter case. When no mass cutoff is imposed, smaller objects (that are excluded in the Press-Schechter picture because their virial temperatures are below the cosmic mean temperature) “leak” inside the \mathcal{M} distribution, because in the double-distribution picture they can lie inside an underdense region (void) and accrete material cooler than the cosmic mean and cooler than their own confined gas. As a result, a larger total number of objects participate in the double distribution and the overall level of the curves is higher than in the PS model.

Note that the effect described above is moderated by the fact that some objects also “leak” out of the distribution, because they lie in overdense regions where the diffuse gas has a temperature larger than their virial temperature (it is this effect that caused the “loss of signal” that is observed in the middle-panel curves).

In all panels of Fig. 3.2 the amplitude of the distribution increases with increasing redshift. This is because the number distribution plotted here is dominated by the low-mass objects, which are merged into larger halos as time progresses. In Fig. 3.3 we plot the double distribution without cutoff model (right panel of Fig. 3.2) using a logarithmic scale for the vertical axis, so that the behavior of the large-mass (and consequently high- \mathcal{M}) objects can be better illustrated. At these high \mathcal{M} s, the behavior of the distribution with redshift is reversed, as more high-mass objects are formed as time progresses.

Figure 3.4 shows the distribution of spatial density of shock surface per logarithmic Mach number interval $dS/d\ln\mathcal{M}$, with $(dS/d\ln\mathcal{M})d\ln\mathcal{M}$ being the total surface of shocks in a certain comoving volume V with logarithmic Mach number between $\ln\mathcal{M}$ and $\ln\mathcal{M} + d\ln\mathcal{M}$ divided by that volume.

This quantity is frequently used to characterize the statistical properties of shocks in cosmological simulations as it can be calculated without need for identification of collapsed structures and assignment of shock-hosting gridpoints to specific structures. The left panel shows this distribution for the PS model while the middle and right panels correspond to the DD models, with (middle panel) and without (right panel) mass cutoffs. The behavior of this quantity is similar to the number distribution with respect to \mathcal{M} in that it is dominated by the low-mass structures, and therefore the existence of a low-mass cutoff significantly affects its qualitative behavior.

Although the number and surface distributions of shocks with respect to Mach number are dominated by the low-mass objects and their corresponding low-Mach-number shocks, the accretor mass, the mass accretion rate and the energetics of shocks are dominated by high-mass objects. This can be immediately verified by simple analytic arguments. We consider for simplicity the Press-Schechter-based variation of our model. For masses high enough that the primordial density fluctuation power spectrum can be regarded as a power law but low enough that the exponential mass

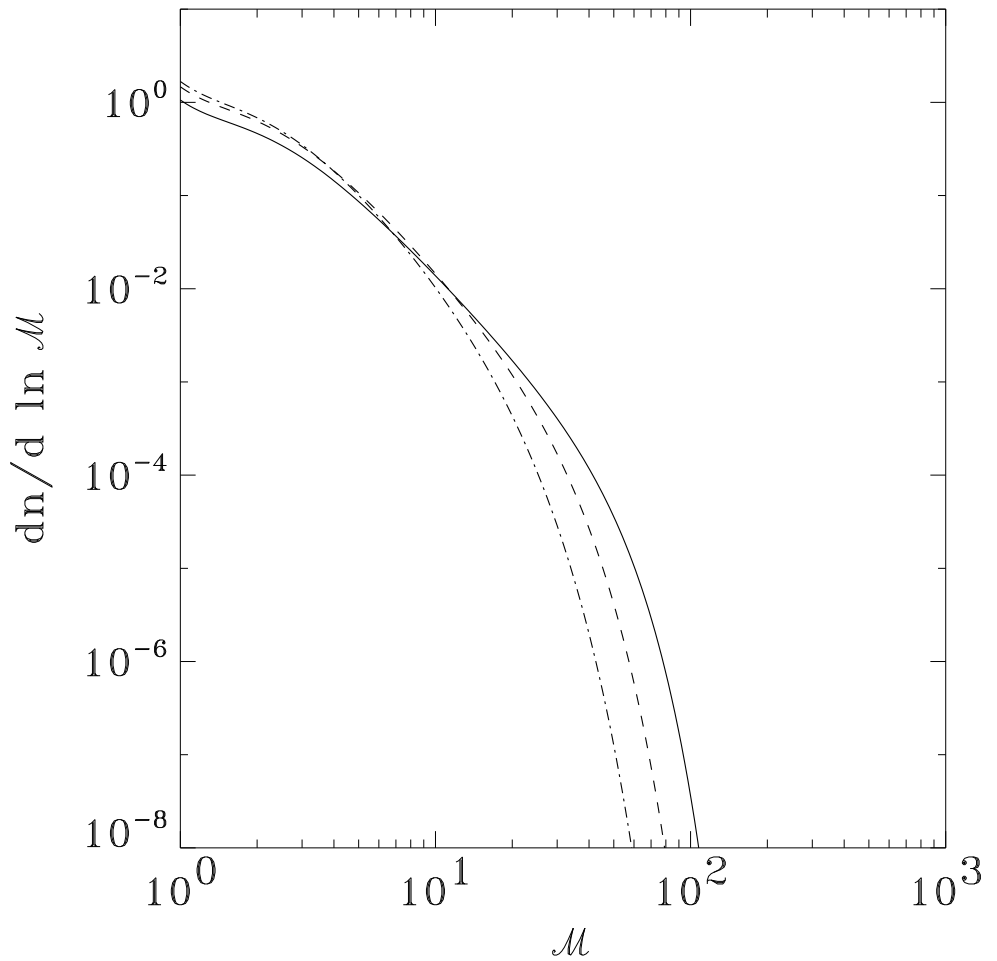


Figure 3.3: Distribution of number density of objects per logarithmic Mach number interval for the double-distribution-based model without a mass cutoff, plotted in logarithmic scale. The units of the vertical axes are number of objects per comoving Mpc^3 . Solid line: $z = 0$; dashed line: $z = 1$; dot-dashed line: $z = 2$.

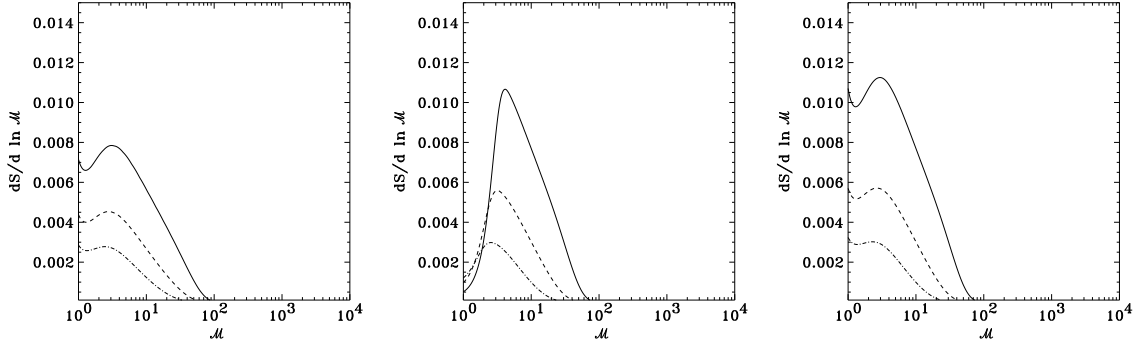


Figure 3.4: Distribution of spatial density of shock surface per logarithmic Mach number interval ($dS/d \ln \mathcal{M}$) for the Press-Schechter-based (left panel) and the double-distribution-based (right panel) models. The units of the vertical axes are comoving Mpc^{-1} . Solid line: $z = 0$; dashed line: $z = 1$; dot-dashed line: $z = 2$.

cutoff is not affecting the results, $dn/dm \propto m^{-2}$. In addition, $\mathcal{M} \propto m^{1/3}$ (in the high- \mathcal{M} limit), while $r_v \propto m^{1/3}$. Hence, $J_1 \propto m$ and $P_1 \propto m^{5/3}$. Equations (3.19)-(3.26) then give for the low-mass dependence of the various statistical properties of the shock population,

$$\begin{aligned}
 \frac{dn}{d \ln \mathcal{M}} &\propto m^{-1} \\
 \frac{dS}{d \ln \mathcal{M}} &\propto m^{-1/3} \\
 \frac{d\rho}{d \ln \mathcal{M}} &\propto m^0 \\
 \frac{dJ}{d \ln \mathcal{M}} &\propto m^0 \\
 \frac{dP}{d \ln \mathcal{M}} &\propto m^{2/3}
 \end{aligned} \tag{3.47}$$

accounting for the difference in the low-mass behavior of different distributions, in particular the divergent behavior of the number distribution and the convergent nature of the mass, mass current and kinetic power distributions. Note that the low-mass suppression is somewhat stronger than what is predicted by the simple arguments above, due to the deviation of $\mathcal{M}(m)$ from $m^{1/3}$ for $\mathcal{M} \rightarrow 1$.

In Fig. 3.5 we plot the accretor mass distribution with respect to Mach number, i.e. the mass in objects with accretion shocks of logarithmic Mach number between $\log \mathcal{M}$ and $\log \mathcal{M} + d \log \mathcal{M}$ versus \mathcal{M} . All models exhibit similar behavior, with the

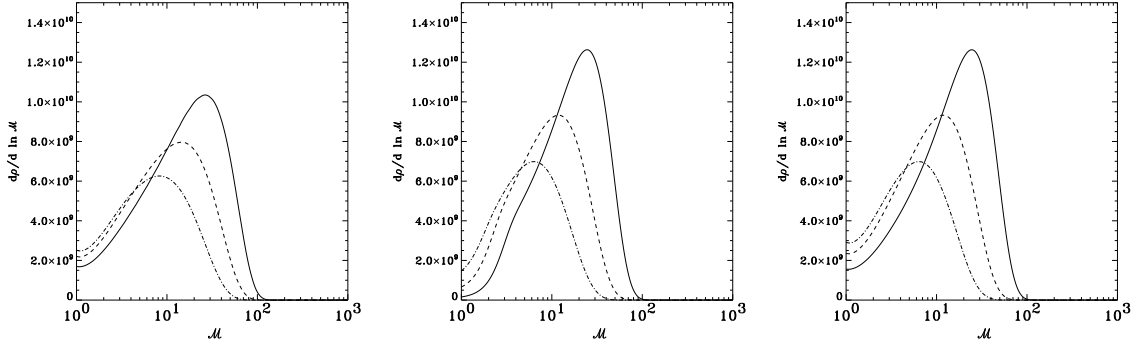


Figure 3.5: Accretor mass distribution (mass density in accretors per logarithmic Mach number interval of associated accretion shock, $d\rho/d \ln \mathcal{M}$) for the Press-Schechter-based (left panel) and the double-distribution-based models, with a Press-Schechter like mass cutoff (middle panel) and without an explicit mass cutoff (right panel). The units of the vertical axes are M_\odot comoving Mpc^{-3} . Solid line: $z = 0$; dashed line: $z = 1$; dot-dashed line: $z = 2$.

high- \mathcal{M} objects dominating the distribution. In this case, the presence or not of a mass cutoff in the DD models does not have a significant effect, as it only affects the low- \mathcal{M} end of the distribution. The location of the peak is at similar values of \mathcal{M} in all models, and is an effect of the high-mass exponential cutoff in collapsed accreting structures. The effect of a varying environmental overdensity and sound speed in this case is to increase the height as well as steepness of decline toward both higher and lower Mach numbers of the distribution peak. This is because the double distribution tends to move lower-mass objects (which generally reside in underdensities) towards higher \mathcal{M} s, and higher-mass objects (which reside in overdensities) towards lower \mathcal{M} s, causing a greater concentration of accretor mass close to the peak.

In Fig. 3.6 we plot the mass current distribution, $dJ/d \ln \mathcal{M}$. Again, the left panel shows the results for the PS model, the middle panel represents the DD model with a Press-Schechter mass cutoff and the right panel is the DD model without a mass cutoff and with the only restriction being $\mathcal{M} \geq 1$.

The environmental effects are more pronounced in this case, while the existence or not of a mass cutoff plays no significant role in the properties of the DD model, again due to the overwhelming dominance of high-mass objects in the total mass processing

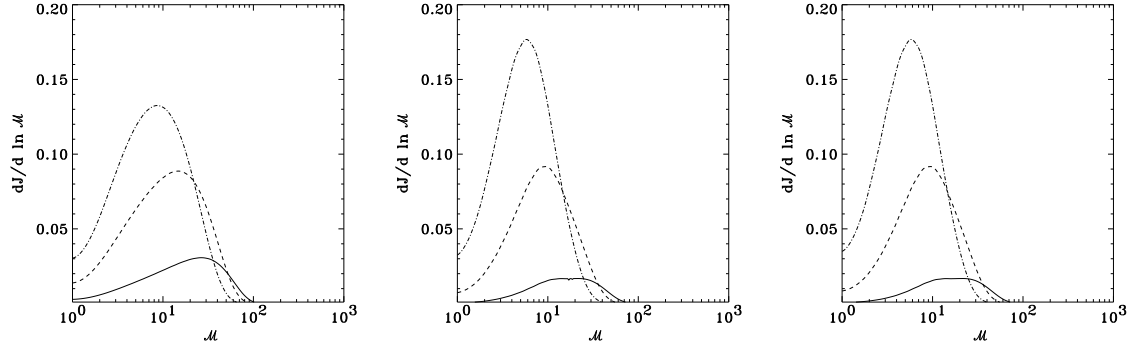


Figure 3.6: Mass current distribution (spatial density of mass current per logarithmic Mach number interval $dJ/d \ln \mathcal{M}$) for the Press-Schechter-based (left panel) and the double-distribution-based (right panel) models. The units of the vertical axes are M_\odot comoving Mpc^{-3} yr. Solid line: $z = 0$; dashed line: $z = 1$; dot-dashed line: $z = 2$.

rate through accretion shocks: the existence or not of a low-mass cutoff cannot affect the mass current distribution because the low- \mathcal{M} objects process only a very small fraction of the total accreted mass.

The effect of taking into account the environmental overdensity distribution using the DD in this case is two-fold: On the one hand, it spreads out every mass bin to a larger \mathcal{M} range as in the previous cases. On the other hand, it also adjusts the local density of the material just outside the object, which in turn affects the local value of the mass current.

The location of the mass current distribution peak and its evolution with redshift do not change appreciably between the two models. The location of the peak represents the high-mass exponential cutoff in the Press-Schechter mass function (the largest mass scale which has collapsed by a certain epoch), modulated by the nonlinear mass- \mathcal{M} relation. However, the DD model declines more sharply towards lower \mathcal{M} . This is because in the double-distribution picture, low-mass, low- \mathcal{M} objects reside inside underdensities and hence they can process less mass than in the Press-Schechter case.

Finally, the suppression of the distribution amplitude with decreasing redshift in all models is a result of the reduction of the mean cosmic density of the accreted

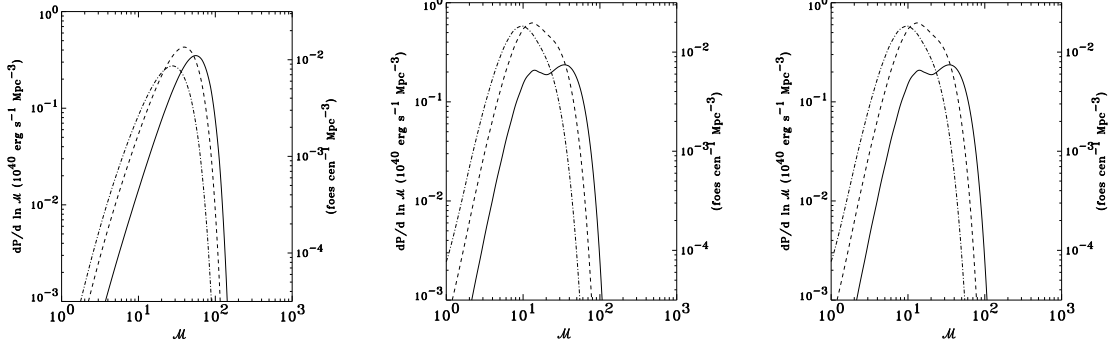


Figure 3.7: Kinetic power distribution (spatial density of kinetic power processed by accretion shocks per logarithmic Mach number interval, $dP/d \ln \mathcal{M}$) for the Press-Schechter-based (left panel) and the double-distribution-based (right panel) models. The units of the vertical axes are $10^{40} \text{ ergs s}^{-1} \text{ comoving Mpc}^{-3}$ (left axis) and $10^{51} \text{ ergs per century per comoving Mpc}^3$ (right axis). Solid line: $z = 0$; dashed line: $z = 1$; dot-dashed line: $z = 2$.

material. The result is more pronounced in the DD models since, in addition to the reduction of the mean density, there is also a shift of the most probable environmental density for structures of a given mass towards regions increasingly underdense with respect to the cosmic mean as time increases.

In Fig. 3.7 we plot the kinetic power distribution with respect to Mach number, for the PS model, and the two variations of the DD model. As in the case of the mass current distribution, the kinetic power distribution is also dominated by objects of high mass and Mach number, and the presence of a lower-mass cutoff does not have a significant effect on the DD models.

A most striking environmental effect in this case is that, as redshift decreases, a second peak separates out in the DD model, which is absent in the PS models. The presence of this second, high- \mathcal{M} peak is due to the gradual shift of increasingly massive structures towards underdense environments. To better demonstrate this effect, we plot in Fig. 3.8 the components of the distribution produced by structures in significantly overdense environments (dot-dashed line, $\delta > \delta_{ta}$, where δ_{ta} is the overdensity of a perturbation turning around at the specific epoch), and structures in environments of $\delta < \delta_{ta}$ (dashed line), for the DD model without a mass cutoff and

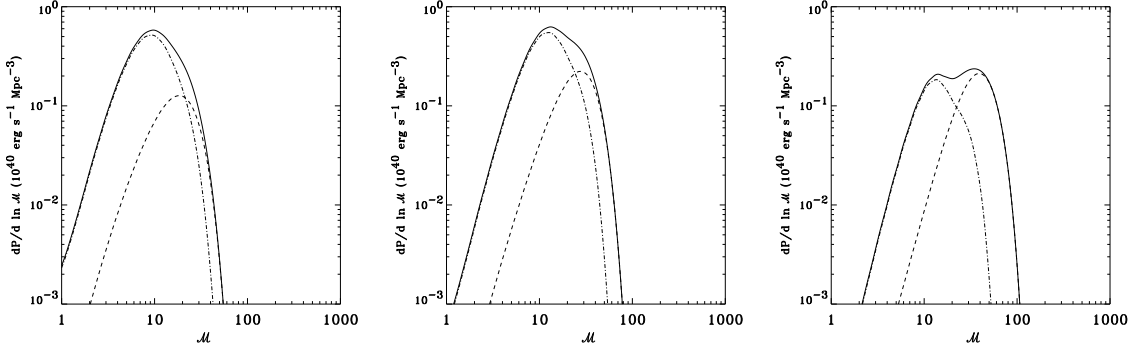


Figure 3.8: Distribution of spatial density of kinetic power per logarithmic Mach number interval ($dP/d \ln \mathcal{M}$) the double-distribution-based model without a mass cutoff. Left panel: $z = 2$; middle panel: $z = 1$; right panel: $z = 0$. Solid line: overall distribution; dot-dashed line: contribution from structures with environmental overdensities between δ_{ta} and δ_v (between turnaround and virialization overdensities); dashed line: contribution from structures with environmental overdensities $\delta < \delta_{ta}$.

for three different redshifts. The contribution from the low-density environments is distinct in \mathcal{M} space and increasing with decreasing redshift.

Figure 3.9 shows the evolution of the integrated kinetic power over shocks of any Mach number, P , for redshifts between 10 and 0. The solid line corresponds to the DD model and the dashed line to the Press-Schechter models. In the left panel, $P(z)$ is plotted as a function of z , and is seen to peak near $z \sim 1$ for both models, when the increase with time of the number and mass of collapsed structures is balanced by the decreasing mean density of the accreted material due to cosmic expansion. The effect is more pronounced and the peak occurs at a slightly higher redshift in the DD model where environmental effects are accounted for, since the decrease in the cosmic mean density is accompanied by a decrease in the most probable overdensity *with respect to cosmic mean*. The overall level of the curve in the DD model is also a factor of ~ 2 higher compared to the PS model at redshifts $\gtrsim 1$, because environmental effects further enhance the contribution of the larger structures which are already favored due to their size and accelerating potential. However, at lower redshifts, when in the DD model the contribution of the smaller structures becomes comparable to that of the larger structures, the integrated kinetic power predicted by the two models tends

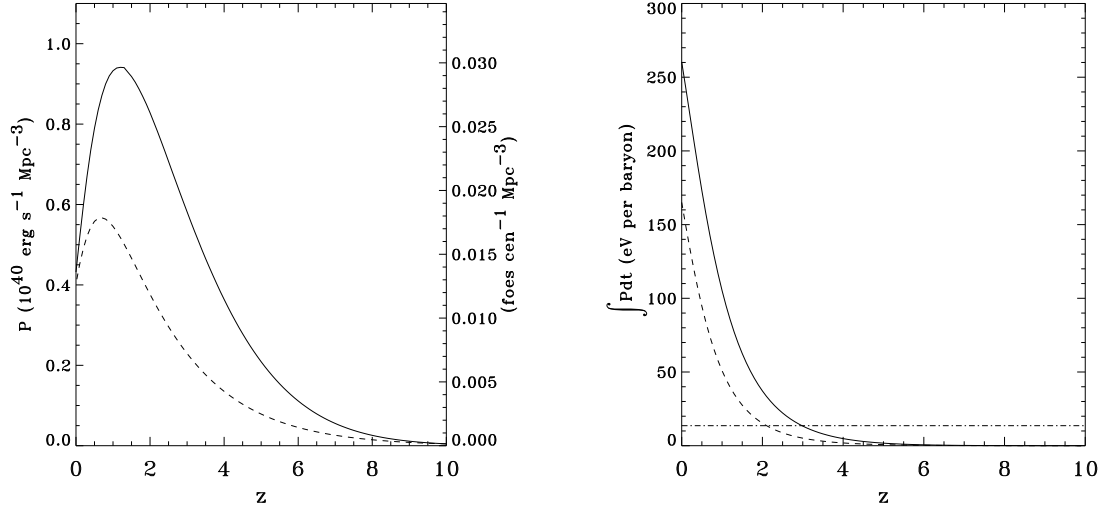


Figure 3.9: Integrated kinetic power over shocks of any Mach number, P , for the Double-Distribution (solid line) and the Press-Schechter (dashed line) models. Left panel: redshift history of P for $z < 10$. Right panel: $\int P dt$ in units of eV per baryon. The horizontal line in the right-panel plot corresponds to 13.6 eV per baryon.

to converge.

The right panel shows the redshift history of $\int P dt$ (the cumulative processed kinetic energy) in units of eV per baryon *in the universe* (as opposed to per shocked baryon). Again, the solid line is the DD model while the dashed line is the PS model. The horizontal line in this plot corresponds to 13.6 eV per baryon. From the location of the intersection of the horizontal line with the $\int P dt$ curve, we can conclude that the energy processed by accretion shocks *alone* by redshift $z \sim 3$ (~ 2 in the PS model) is of order of magnitude comparable to the energy required to reionize the universe even in absence of other sources of energy ².

Finally, in Fig. 3.10 we plot the integrated mass current over shocks of any Mach number, J , for the DD (solid line) and the PS (dashed line) models. The left panel shows the redshift history of J for $z < 10$, while the right panel shows the redshift his-

²Note that this order-of-magnitude argument is meant to give a feeling about the amount of energy processed by shocks as compared to other energy inputs in the IGM. If one wanted to consider shocks as an actual reionization mechanism, a detailed modelling of the reionization process would be required.

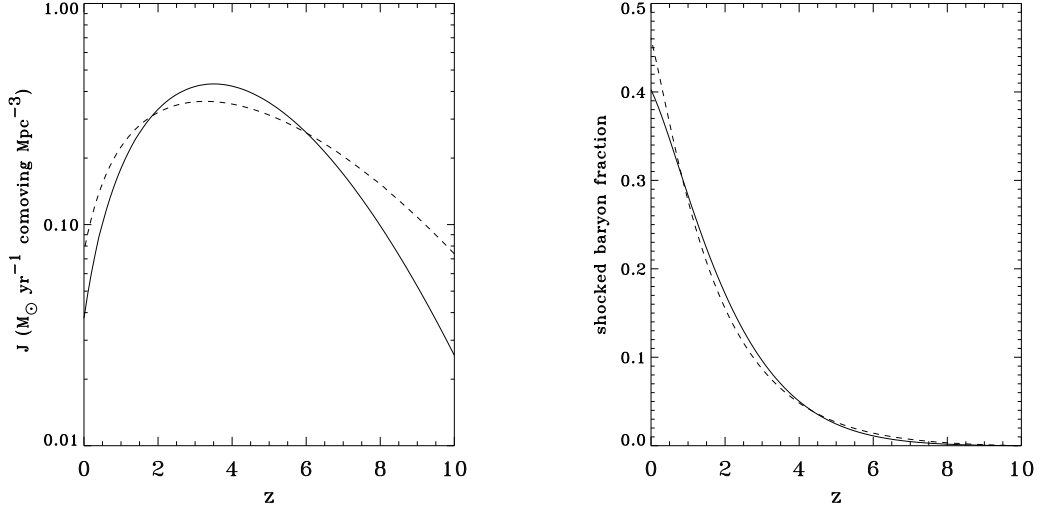


Figure 3.10: Integrated mass current over shocks of any Mach number, J , for the Double-Distribution (solid line) and the Press-Schechter (dashed line) models. Left panel: redshift history of J for $z < 10$. Right panel: $\int J dt$ expressed as the fraction of baryons in the universe which have been processed by accretion shocks.

tory of $\int J dt$, the cumulative shocked gas mass, expressed as the fraction of baryons in the universe which have been processed by accretion shocks. By the current cosmic epoch, a fraction between 40 – 50% of baryons have already been processed by accretion shocks, while $\sim 10\%$ of the baryons have already been processed by shocks by $z \sim 3$.

3.4.3 Comparison with Cosmological Simulations

Caution should be exercised when comparing these calculations to results of cosmological simulations studying the properties of cosmic shocks, to ensure that corresponding quantities are being compared. One should keep in mind that the shocks studied in this chapter (a) are accretion shocks only, while effects of merger and filament shocks and their contribution to shock statistics and energetics have not been included and (b) are all considered to be external shocks, accreting material which has never been shocked before.

In [63], the cosmological simulation results are presented by classifying shocks

as external or internal, depending on the temperature of the accreted material. In both the kinetic and surface distributions with respect to Mach number, used by the authors to describe the statistical properties of cosmic shocks, external shocks are dominated by filament shocks, while internal shocks are dominated by merger shocks. The population of accretion shocks is presumably divided between these two categories, depending on whether structures accrete void or filament material. Accretion shocks are expected to lie in the high Mach number end of both internal and external shock distributions. Hence, no direct comparison between our model and these results is possible without the inclusion of a detailed model of filament-shocked material and the way it modifies the properties of the accretion shock population. However, properly adjusting our model to the [63] simulation parameters, we find that if we consider the entire population of accretion shocks to be either external (as in the results of the previous section) or internal with mean density and temperature values for the filament gas taken from the [63] results, our curves lie, as expected, *below* their overall curves for external or internal shocks, respectively, for all relevant quantities, although they constitute an appreciable fraction of them.

In [61], the simulated shocks are instead divided in accretion and merger shocks, the accretion shocks being assigned to specific structures. The principal quantity used to statistically describe the shock population itself is the number distribution of shocks with respect to Mach number. However, a direct comparison is not appropriate in this case either, because part of the simulated population of accretion shocks resides inside filaments, which introduces a bi-modality in the number distribution, especially pronounced in the $\Omega_m = 1$ simulation. In addition, the properties of the shocks even around structures which accrete principally pristine material are modified by lateral accretion of hotter gas from the filaments. Finally, the combination of selection criteria for the collapsed structures inhibits the identification of a sharp mass cutoff to use in our analytical models.

Overall, although the models we have used here can reveal the effect of a certain class of environmental factors (local overdensity and associated change in temperature) on the statistics of cosmic accretion shocks, it becomes clear that for a detailed comparison with simulations and observations, a treatment of the second important environmental factor, i.e. the filamentary structure of the universe, is needed.

A result of this work with direct relevance to the interpretation of cosmological simulations studying the properties of cosmic shocks is the effect of the existence of an explicit mass cutoff to the properties of different shock distributions, since mass cutoffs are always present in simulations as a result of finite mass resolution. We have seen that the number distribution as well as surface distribution of shocks with respect to Mach number are dominated by the contribution of low-mass objects and hence they are appreciably affected by the presence of a mass cutoff. The rest of our shock distributions however, such as the mass current distribution and the kinetic power distribution are dominated by high-mass objects and are unaffected by the presence of a mass cutoff. This is consistent with the findings of [63], who performed a series of simulations with increasing mass and spatial resolution, and found convergence for their results on kinetic power distribution but not for the surface distribution. However, the physical impact of shocks to their environment is better represented by the latter class of distributions, which are unaffected by the value of the mass cutoff, and hence the lack of convergence in the number-dominated distributions need not decrease confidence in the relevance and robustness of the physical output of such cosmological simulations.

Chapter 4

Discussion

In this thesis, we have derived and explored a new tool for the analytical study of hierarchical structure formation: a double distribution of the number density of cosmic collapsed structures with respect to mass and local overdensity. We have done so by introducing a clustering scale parameter $\beta > 1$, which we use to associate with each collapsed object of mass m a larger environment of mass βm . The scale parameter β can be expressed as a function of the number of virial radii included in the local environment of each structure. We found that for reasonable values $\beta \sim 2$, the shape of the distribution does not depend sensitively on this parameter. Integration over linearly extrapolated overdensity returns the original Press-Schechter mass function, independently of the value of β .

We have presented the double distribution in terms of the true, physical, nonlinear density contrast δ . However, in calculating the distribution it is useful to identify regions using instead the overdensity obtained via linear analysis, $\tilde{\delta}$, extrapolated to the present epoch. A useful fitting function was given for the $\delta - \tilde{\delta}$ conversion.

The double distribution is useful because it allows us to have an explicit analytical if approximate description of the environment in which collapsed objects of all masses reside. Using the tools we have developed, it can be readily calculated for any flat cosmology, and evaluated at any epoch. Consequently, it offers new insight into the

growth of structure as well as the present distribution of collapsed objects.

We have evaluated the double distribution and some of its integral moments for both a concordance cosmology and an Einstein-de Sitter universe. Some key results are that at any redshift, the double distribution is dominated by a peak which shifts in mass but is always at a relatively low value of $|\delta|$. For each mass, there is a most probable δ , which increases with structure mass. Moreover, at the present epoch in the concordance universe, the most probable environment is a modest *underdensity*, for all objects below about $10^{14} M_\odot$; thus, underdensities are preferentially populated by low-mass objects. Finally, the fraction of mass in underdensities increases with time, and in the concordance cosmology the present underdense mass fraction in objects of $M > 10^{12} M_\odot$ is about 40%. These trends can be understood in terms of hierarchical clustering in which overdense regions are the site of vigorous merging that clears out low-mass objects, which then find their last refuge in voids.

In addition, we have utilized the double distribution of cosmic structures to investigate analytically the effect of environmental factors on the properties of cosmic accretion shocks around collapsed structures. For this purpose, we have explored two different models for the cosmic shock population. The first used the Press-Schechter mass function to describe the underlying population of collapsed, accreting objects. All such objects were assumed to accrete material of the same density and temperature. This was our “control” model, which did not include any environmental effects. The second model used the double distribution of collapsed structures [75] to describe the distribution of accreting objects with respect to both their mass and local environment overdensity or underdensity. The overall mass distribution of objects is the same as in the first model, as the double distribution integrates to the Press-Schechter mass function.

We found that the number and surface distributions of shocks with respect to Mach number are dominated by the contribution from low-mass objects and hence peak at

low Mach numbers for both models. The contrary is true for distributions describing the physical impact of accretion shocks on their environment, such as the mass current and kinetic power distributions, which are dominated by the properties of primarily high-mass objects, and hence peak at high Mach numbers. The distribution peaks are more pronounced when environmental effects are taken into account, as they tend to move objects of both high and low masses towards the peak.

Perhaps the most striking effect of accounting for the environmental factor is the separation of a second, high Mach number peak in the kinetic power distribution at low redshifts, due to an increasing number of higher-mass structures concentrating inside underdensities. This double-peaked behavior is present despite the fact that the effect of filament heating of the accreted gas was not included in our calculation. The latter process is expected to further complicate the features of the kinetic power distribution.

The integrated kinetic power processed by shocks peaks at a redshift of ~ 1 , and the effect of the local environment is to increase the overall level of the processed energy at high redshifts by a factor of ~ 2 as well as to move the peak of the kinetic power history towards slightly higher redshifts. We found that accretion shocks alone have processed by $z \sim 3$ energy comparable to that required to reionize the universe.

The integrated mass current history (i.e., the net baryonic mass processed through shocks) peaks at earlier epochs compared to the kinetic power redshift, with the peak in both models occurring at $z \sim 3$. By the current epoch, the baryon fraction shocked in accretion shocks alone is between 40 – 50%. Since this material represents baryons which can condense to form galaxies and stars, this fraction represents an upper limit to the baryon fraction in galaxies.

The population study of cosmic accretion shocks presented in the second part of this thesis is only one of many possible applications of the double distribution of cosmic structures. With its capability to treat both underdensities and overdensities,

and collapsed as well as diffuse regions, the double distribution can be used to build analytical models for many problems which are currently attracting much interest in the context of cosmological structure formation. The filamentary structure of the universe and the dependence of merger histories on environmental factors are only two such problems that we are currently pursuing using the tools developed in this thesis.

Appendix A

Limits of the Double Distribution

In this appendix, we examine the behavior of the double distribution in the limiting cases $\beta \rightarrow \infty$ and $\beta \rightarrow 1$.

A.1 Behavior of the Double Distribution in the limit $\beta \rightarrow \infty$

In order to find the behavior the double distribution as $\beta \rightarrow \infty$, we recall that, because $S(m)$ decreases monotonically with m , its limit in the infinite β regime will be

$$\lim_{\beta \rightarrow \infty} S(\beta m) = 0. \quad (\text{A.1})$$

Then, using the notation of the previous section,

$$\lim_{\beta \rightarrow \infty} \frac{dn}{dm d\tilde{\delta}_\ell} (m, \tilde{\delta}_\ell, \beta, a) = \lim_{S_2 \rightarrow 0} \frac{dn}{dm d\tilde{\delta}_\ell} (S_1, S_2, \tilde{\delta}_\ell, a, m). \quad (\text{A.2})$$

The limit of a unit-area Gaussian when its width vanishes is the Dirac delta-function δ_D ,

$$\lim_{\lambda \rightarrow 0} \frac{1}{\sqrt{2\pi}\lambda} \exp \left[-\frac{(x - x_0)^2}{2\lambda^2} \right] = \delta_D(x - x_0). \quad (\text{A.3})$$

Using this result, we get

$$\begin{aligned}
\lim_{S_2 \rightarrow 0} \frac{dn}{dmd\tilde{\delta}_\ell} &= \frac{\rho_m}{m} \left| \frac{dS_1}{dm} \right| \frac{\tilde{\delta}_{0,c} - \tilde{\delta}_\ell}{2\pi} \times \\
&\quad \lim_{S_2 \rightarrow 0} \left\{ \exp \left[-\frac{(\tilde{\delta}_{0,c} - \tilde{\delta}_\ell)^2}{2(S_1 - S_2)} \right] \frac{\exp \left[-\frac{\tilde{\delta}_\ell^2}{2S_2} \right] - \exp \left[-\frac{(\tilde{\delta}_\ell - 2\tilde{\delta}_{0,c})^2}{2S_2} \right]}{S_2^{1/2}(S_1 - S_2)^{3/2}} \right\} \\
&= \frac{\rho_m}{m} \left| \frac{dS_1}{dm} \right| \frac{\tilde{\delta}_{0,c} - \tilde{\delta}_\ell}{\sqrt{2\pi}} \frac{\exp \left[-\frac{(\tilde{\delta}_{0,c} - \tilde{\delta}_\ell)^2}{2S_1} \right]}{S_1^{3/2}} \times \\
&\quad \left\{ \lim_{S_2 \rightarrow 0} \frac{\exp \left[-\frac{\tilde{\delta}_\ell^2}{2S_2} \right]}{\sqrt{2\pi S_2}} - \lim_{S_2 \rightarrow 0} \frac{\exp \left[-\frac{(\tilde{\delta}_\ell - 2\tilde{\delta}_{0,c})^2}{2S_2} \right]}{\sqrt{2\pi S_2}} \right\} \\
&= \frac{\rho_m}{m} \left| \frac{dS_1}{dm} \right| \frac{\tilde{\delta}_{0,c} - \tilde{\delta}_\ell}{\sqrt{2\pi}} \frac{\exp \left[-\frac{(\tilde{\delta}_{0,c} - \tilde{\delta}_\ell)^2}{2S_1} \right]}{S_1^{3/2}} \left[\delta_D(\tilde{\delta}_\ell) - \delta_D(\tilde{\delta}_\ell - 2\tilde{\delta}_{0,c}) \right] \quad (A.4)
\end{aligned}$$

However, the $\tilde{\delta}_\ell$ -domain of the double distribution is between $-\infty$ and $\tilde{\delta}_{0,c}$, and therefore the value $\tilde{\delta}_\ell = 2\tilde{\delta}_{0,c}$ is outside its domain. Hence the second Dirac delta-function is always zero, and

$$\lim_{\beta \rightarrow \infty} \frac{dn}{dmd\tilde{\delta}_\ell} = \frac{\rho_m}{m} \left| \frac{dS_1}{dm} \right| \frac{\tilde{\delta}_{0,c} - \tilde{\delta}_\ell}{\sqrt{2\pi}} \frac{\exp \left[-\frac{(\tilde{\delta}_{0,c} - \tilde{\delta}_\ell)^2}{2S_1} \right]}{S_1^{3/2}} \delta_D(\tilde{\delta}_\ell), \quad (A.5)$$

proportional, as expected, to a Dirac delta-function centered at $\tilde{\delta}_\ell = 0$.

A.2 Behavior of the Double Distribution in the limit $\beta \rightarrow 1$

Denoting $S(\beta m)$ by S_2 and letting $\phi = S(m)/S(\beta m)$, we seek the behavior of the double distribution in the limit $\beta \rightarrow 1$ or $\phi \rightarrow 1$. Defining

$$\mathcal{C} = \frac{\rho_m}{m} \frac{\tilde{\delta}_{0,c} - \tilde{\delta}_\ell}{\sqrt{2\pi}} \left| \frac{dS}{dm} \right| \frac{\exp \left[-\frac{\tilde{\delta}_\ell^2}{2S_2} \right] - \exp \left[-\frac{(\tilde{\delta}_\ell - 2\tilde{\delta}_{0,c})^2}{2S_2} \right]}{S_2^{1/2}}, \quad (A.6)$$

we can write

$$\begin{aligned}
\lim_{\phi \rightarrow 1} \frac{dn}{dm d\tilde{\delta}_\ell} &= \mathcal{C} \lim_{\phi \rightarrow 1} \frac{\exp \left[-\frac{(\tilde{\delta}_{0,c} - \tilde{\delta}_\ell)^2}{2S_2(\phi-1)} \right]}{\sqrt{2\pi} S_2^{3/2} (\phi-1)^{3/2}} \\
&= \mathcal{C} \lim_{\phi \rightarrow 1} \frac{(\phi-1)^{-3/2}}{\sqrt{2\pi} S_2^{3/2} \exp \left[\frac{(\tilde{\delta}_{0,c} - \tilde{\delta}_\ell)^2}{2S_2(\phi-1)} \right]} \\
&\stackrel{\infty/\infty}{=} \mathcal{C} \lim_{\phi \rightarrow 1} \frac{-\frac{3}{2}(\phi-1)^{-5/2}}{\exp \left[\frac{(\tilde{\delta}_{0,c} - \tilde{\delta}_\ell)^2}{2S_2(\phi-1)} \right] \left[-\frac{\sqrt{2\pi} S_2^{3/2} (\tilde{\delta}_{0,c} - \tilde{\delta}_\ell)^2}{2S_2(\phi-1)^2} \right]} \\
&= \mathcal{C} \lim_{\phi \rightarrow 1} \frac{3 \exp \left[-\frac{(\tilde{\delta}_{0,c} - \tilde{\delta}_\ell)^2}{2S_2(\phi-1)} \right]}{\sqrt{2\pi} S_2^{1/2} (\phi-1)^{1/2} (\tilde{\delta}_{0,c} - \tilde{\delta}_\ell)^2} \\
&= \mathcal{C} \frac{3}{(\tilde{\delta}_{0,c} - \tilde{\delta}_\ell)^2} \delta_D(\tilde{\delta}_{0,c} - \tilde{\delta}_\ell) \tag{A.7}
\end{aligned}$$

proportional, as expected, to a Dirac delta-function around $\tilde{\delta}_{0,c}$.

Appendix B

Derivation of the Press-Schechter Mass Function From the Double Distribution

Using S_1 to denote $S(m)$ and S_2 for $S(\beta m)$ we have:

$$\int_{-\infty}^{\tilde{\delta}_{0,c}} d\tilde{\delta} \frac{dn}{dm d\tilde{\delta}} = \frac{\rho_m}{m} \left| \frac{dS_1}{dm} \right| \frac{1}{2\pi S_2^{1/2} (S_1 - S_2)^{3/2}} \times \quad (B.1)$$

$$\left\{ \int_{-\infty}^{\tilde{\delta}_{0,c}} d\tilde{\delta} (\tilde{\delta}_{0,c} - \tilde{\delta}) \exp \left[-\frac{\tilde{\delta}^2}{2S_2} \right] \exp \left[-\frac{(\tilde{\delta}_{0,c} - \tilde{\delta})^2}{2(S_1 - S_2)} \right] - \right. \\ \left. \int_{-\infty}^{\tilde{\delta}_{0,c}} d\tilde{\delta} (\tilde{\delta}_{0,c} - \tilde{\delta}) \exp \left[-\frac{(\tilde{\delta} - 2\tilde{\delta}_{0,c})^2}{2S_2} \right] \exp \left[-\frac{(\tilde{\delta}_{0,c} - \tilde{\delta})^2}{2(S_1 - S_2)} \right] \right\}$$

$$\stackrel{\tilde{\delta}' = \tilde{\delta}_{0,c} - \tilde{\delta}}{=} \frac{\rho_m}{m} \left| \frac{dS_1}{dm} \right| \frac{1}{2\pi S_2^{1/2} (S_1 - S_2)^{3/2}} \times \quad (B.2)$$

$$\left\{ \int_0^{\infty} d\tilde{\delta}' \tilde{\delta}' \exp \left[-\frac{(\tilde{\delta}_{0,c} - \tilde{\delta}')^2}{2S_2} \right] \exp \left[-\frac{\tilde{\delta}'^2}{2(S_1 - S_2)} \right] - \right. \\ \left. \int_0^{\infty} d\tilde{\delta}' \tilde{\delta}' \exp \left[-\frac{(\tilde{\delta}_{0,c} + \tilde{\delta}')^2}{2S_2} \right] \exp \left[-\frac{\tilde{\delta}'^2}{2(S_1 - S_2)} \right] \right\} \quad (B.3)$$

Then, performing the transformation $\tilde{\delta}' \rightarrow -\tilde{\delta}'$ in the second integral, we get

$$\begin{aligned}
\int_{-\infty}^{\tilde{\delta}_{0,c}} d\tilde{\delta} \frac{dn}{dm d\tilde{\delta}} &= \frac{\rho_m}{m} \left| \frac{dS_1}{dm} \right| \frac{1}{2\pi S_2^{1/2} (S_1 - S_2)^{3/2}} \times & (B.4) \\
&\quad \left\{ \int_0^\infty d\tilde{\delta}' \tilde{\delta}' \exp \left[-\frac{(\tilde{\delta}_{0,c} - \tilde{\delta}')^2}{2S_2} \right] \exp \left[-\frac{\tilde{\delta}'^2}{2(S_1 - S_2)} \right] + \right. \\
&\quad \left. \int_{-\infty}^0 d\tilde{\delta}' \tilde{\delta}' \exp \left[-\frac{(\tilde{\delta}_{0,c} - \tilde{\delta}')^2}{2S_2} \right] \exp \left[-\frac{\tilde{\delta}'^2}{2(S_1 - S_2)} \right] \right\} \\
&= \frac{\rho_m}{m} \frac{1}{2\pi S_2^{1/2} (S_1 - S_2)^{3/2}} \left| \frac{dS_1}{dm} \right| \times \\
&\quad \int_{-\infty}^\infty \tilde{\delta}' d\tilde{\delta}' \exp \left[-\frac{(\tilde{\delta}_{0,c} - \tilde{\delta}')^2}{2S_2} \right] \exp \left[-\frac{\tilde{\delta}'^2}{2(S_1 - S_2)} \right] \\
&= \frac{\rho_m}{m} \frac{|dS_1/dm|}{2\pi S_2^{1/2} (S_1 - S_2)^{3/2}} \tilde{\delta}_{0,c} \left(\frac{S_1 - S_2}{S_1} \right)^{3/2} \sqrt{2\pi S_2} \exp \left[-\frac{\tilde{\delta}_{0,c}^2}{2S_1} \right] \\
&= \sqrt{\frac{2}{\pi}} \frac{\rho_m}{m^2} \frac{\tilde{\delta}_{0,c}}{\sqrt{S_1}} \left| \frac{d \ln \sqrt{S_1}}{d \ln m} \right| \exp \left[-\frac{\tilde{\delta}_{0,c}^2}{2S_1} \right] & (B.5)
\end{aligned}$$

The final result is the Press-Schechter mass function formula, independently of the value of β .

Appendix C

Vacuum Integrals

C.1 The incomplete vacuum integral of the first kind \mathcal{V}_1

C.1.1 Definition

We define the incomplete vacuum integral of the first kind as

$$\mathcal{V}_1(r, \mu) = \frac{3}{2} \int_0^r \frac{\sqrt{x} dx}{\sqrt{(1-x)(-x^2-x+\mu)}}, \quad (\text{C.1})$$

with domain $0 \leq r \leq 1$ and $\mu \geq 2$.

C.1.2 Properties

Physically, $\mathcal{V}_1(r, \mu)$ is proportional to the time required by a perturbation of normalized curvature parameter $\kappa/\omega^{1/3} = (\mu+1)/\mu^{2/3}$ to achieve a size $a_p = r a_{p,ta}(\kappa/\omega^{1/3})$ *before turnaround*. Its asymptotic behavior for $r \ll 1$ is

$$\mathcal{V}_1(r, \mu) \stackrel{r \ll 1}{\approx} \frac{1}{\sqrt{\mu}} r^{3/2} \quad (\text{C.2})$$

while for $\mu \gg 1$ it is

$$\mathcal{V}_1(r, \mu) \stackrel{\mu \gg 1}{\approx} \frac{1}{\sqrt{2\mu}} \left[\frac{\pi}{2} - \sqrt{r(1-r)} - \sin^{-1} \sqrt{1-r} \right] \quad (\text{C.3})$$

In the case of the Eddington perturbation ($\mu = 2$), we can derive a closed-form expression for \mathcal{V}_1 :

$$\begin{aligned}\mathcal{V}_1(r, 2) &= \frac{3}{2} \int_0^r \frac{\sqrt{x} dx}{(1-x)\sqrt{x+2}} \\ &= \frac{\sqrt{3}}{2} \left[\ln \frac{1+\sqrt{r}}{1-\sqrt{r}} - 2\sqrt{3} \sinh^{-1} \sqrt{\frac{r}{2}} \right. \\ &\quad \left. + \ln \frac{2\sqrt{3} + \sqrt{3r} + 3\sqrt{2+r}}{2\sqrt{3} - \sqrt{3r} + 3\sqrt{2+r}} \right].\end{aligned}\quad (\text{C.4})$$

When $r = 1$, the value of $\mathcal{V}_1(1, \mu)$ is the *complete* vacuum integral of the first kind, which is a function of μ alone. Physically, the complete vacuum integral of the first kind is proportional to the time required for a perturbation of curvature parametrized by μ to reach turnaround. The derivative of $\mathcal{V}_1(1, \mu)$ appears in the calculation of the derivative $\partial \tilde{\delta}_o / \partial \delta$, in the 3rd line of Table 2.4, and it is

$$\frac{d}{d\mu} \mathcal{V}_1(1, \mu) = -\frac{3}{4} \int_0^1 \frac{\sqrt{x} dx}{\sqrt{1-x}(-x^2 - x + \mu)^{3/2}}. \quad (\text{C.5})$$

C.2 The hyperbolic vacuum integral of the first kind \mathcal{H}_1

C.2.1 Definition

We define the hyperbolic vacuum integral of the first kind as

$$\mathcal{H}_1(r, \varpi) = \frac{3}{2} \int_0^r \frac{\sqrt{x} dx}{\sqrt{(1+x)(x^2 - x + \varpi)}}, \quad (\text{C.6})$$

with domain $0 \leq r < \infty$ and $\varpi > 1/4$.

C.2.2 Properties

Physically, $\mathcal{H}_1(r, \varpi)$ is proportional to the time required by a perturbation of normalized curvature parameter $\kappa/\omega^{1/3} = (1 - \varpi)/\varpi^{2/3}$ to achieve a size $a_p =$

$ra_{\text{p,R}}(\kappa/\omega^{1/3})$. Its asymptotic behavior for $r \ll 1$ is

$$\mathcal{H}_1(r, \varpi) \stackrel{r \ll 1}{\approx} \frac{1}{\sqrt{\varpi}} r^{3/2} \quad (\text{C.7})$$

while for $r \gg 1$ it is

$$\mathcal{H}_1(r, \varpi) \stackrel{r \gg 1}{\approx} C(\varpi) + \frac{3}{2} \ln \left(2\sqrt{r^2 - r + \varpi} + 2r - 1 \right) \quad (\text{C.8})$$

where $C(\varpi)$ is a function dependent only on ϖ . In the case of a flat ($\varpi = 1$) perturbation, \mathcal{H}_1 can be integrated immediately to give

$$\mathcal{H}_1(r, 1) = \frac{3}{2} \int_0^r \frac{\sqrt{x} dx}{\sqrt{x^3 + 1}} = \sinh^{-1} \sqrt{x^3}. \quad (\text{C.9})$$

C.3 The incomplete vacuum integral of the second kind \mathcal{V}_2

C.3.1 Definition

We define the incomplete vacuum integral of the second kind as

$$\mathcal{V}_2(r, \mu) = \frac{3}{4} \int_0^r \frac{x^{3/2} dx}{(1-x)^{3/2}(-x^2-x+\mu)^{3/2}}, \quad (\text{C.10})$$

with domain same as for $\mathcal{V}_1(r, \mu)$.

C.3.2 Properties

The incomplete vacuum integral of the second kind is related to $\mathcal{V}_1(r, \mu)$ through

$$\frac{\partial}{\partial(\kappa/\omega^{1/3})} \mathcal{V}_1(r, \mu) = \mu^{2/3} \mathcal{V}_2(r, \mu), \quad (\text{C.11})$$

with

$$\kappa/\omega^{1/3} = (1+\mu)/\mu^{2/3}. \quad (\text{C.12})$$

In the case of the Eddington perturbation ($\mu = 2$), we can derive closed-form expressions for \mathcal{V}_2 :

$$\begin{aligned}
\mathcal{V}_2(r, 2) &= \frac{3}{4} \int_0^r \frac{x^{3/2} dx}{(1-x)^3(x+2)^{3/2}} \\
&= \frac{\sqrt{3}}{72} \left[\frac{\sqrt{3r}(2-3r+4r^2)}{\sqrt{2+r}(1-r)^2} \right. \\
&\quad \left. + \log \frac{1-r}{1+2r+\sqrt{3r(2+r)}} \right]. \tag{C.13}
\end{aligned}$$

C.4 The hyperbolic vacuum integral of the second kind \mathcal{H}_2

C.4.1 Definition

We define the hyperbolic vacuum integral of the second kind as

$$\mathcal{H}_2(r, \varpi) = \frac{3}{4} \int_0^r \frac{x^{3/2} dx}{(1+x)^{3/2}(x^2-x+\varpi)^{3/2}}, \tag{C.14}$$

and its domain is that of $\mathcal{H}_1(r, \varpi)$.

C.4.2 Properties

The hyperbolic vacuum integral of the second kind is related to $\mathcal{H}_1(r, \varpi)$ through

$$\frac{\partial}{\partial(\kappa/\omega^{1/3})} \mathcal{H}_1(r, \varpi) = \varpi^{2/3} \mathcal{H}_2(r, \varpi), \tag{C.15}$$

with

$$\kappa/\omega^{1/3} = (1+\varpi)/\varpi^{2/3}. \tag{C.16}$$

In the case of a flat ($\varpi = 1$) perturbation, \mathcal{H}_2 takes the form

$$\mathcal{H}_2(r, 1) = \frac{3}{2^{4/3}} \int_0^{2^{1/3}r} \left(\frac{u}{u^3+2} \right)^{3/2} du, \tag{C.17}$$

which is the integral entering the linear growth factor in the $\Omega_m + \Omega_\Lambda = 1$ universe. Hence, the linear growth factor function $A(x)$ can be written as

$$A(x) = \frac{2^{4/3}(x^3 + 2)^{1/2}}{3x^{3/2}} \mathcal{H}_2(2^{-1/3}x, 1). \quad (\text{C.18})$$

Appendix D

Comparison to Bertschinger Similarity Solution

In this appendix, we compare the Mach number as derived from the temperature jump across the accretion shock surrounding a collapsed structure (presented in chapter 3) to the similarity solution derived by Bertschinger [59] for the case of a single, spherically symmetric collapsed structure accreting matter in an otherwise homogeneous $\Omega_m = 1$ universe. According to the Bertschinger solution, the accretion shock is positioned at a constant fraction $\lambda_s \approx 0.347$ of the radius r_{ta} of the matter shell turning around at a given cosmic time t ,

$$r_s(m, t) = \lambda_s r_{ta}(m, t) = 0.347 \left(\frac{9}{14} m G t^2 \right)^{1/3} \quad (D.1)$$

where m is the mass of the structure at the specific time t . The velocity of the infalling gas in the lab frame at the shock position is

$$v_g = -1.43 \frac{r_{ta}(m, t)}{t} . \quad (D.2)$$

The shock surface itself is propagating outwards, with a velocity $v_s = (8/9)\lambda_s r_{\text{ta}}/t^1$.

Then, the absolute value of the gas velocity *in the shock frame*, v_1 , is

$$v_1 = |v_g - v_s| = \left| -1.43 - \frac{8}{9}\lambda_s \right| \frac{r_{\text{ta}}}{t} \quad (\text{D.3})$$

$$= 1.74 \left(\frac{27GH_0}{14} \right)^{1/3} (1+z)^{1/2} m^{1/3}. \quad (\text{D.4})$$

If now the pre-shock material has an adiabatic sound speed c_{s1} , the Mach number of the accretion shock is

$$\begin{aligned} \mathcal{M}(m, z, c_{s1}) &= \frac{v_1}{c_{s1}} \\ &= \frac{1.74}{c_{s1}} \left(\frac{27GH_0}{14} \right)^{1/3} (1+z)^{1/2} m^{1/3} \\ &= 92 \left(\frac{15 \text{ km s}^{-1}}{c_{s1}} \right) (1+z)^{1/2} \\ &\quad \times \left(\frac{m}{m_8} \right)^{1/3}. \end{aligned} \quad (\text{D.5})$$

Note that the Bertschinger solution was derived in the limit $\mathcal{M} \rightarrow \infty$, and therefore it is only valid for $\mathcal{M} \gg 1$.

We can compare Eq. (D.5) with the result we derived using the temperature jump across the surface of the shock. Combining Eq.s (3.3) (for the temperature jump in the high- \mathcal{M} limit) and (3.6) we get

$$\begin{aligned} \mathcal{M} &\approx 93 \left(\frac{15 \text{ km s}^{-1}}{c_s} \right) (1+z)^{1/2} \left(\frac{f_c}{18\pi^2} \right)^{1/6} \\ &\quad \times \left(\frac{m}{m_8} \right)^{1/3}, \end{aligned} \quad (\text{D.6})$$

in excellent agreement with Eq. (D.5). The small ($\sim 1\%$) deviation arises because, in obtaining \mathcal{M} from T_2/T_1 , we have ignored any temperature structure within the collapsed object, and have instead assumed that the virial temperature of the structure is representative of the temperature right behind the shock, while the Bertschinger analysis calculates and takes into account the temperature structure inside the shock surface.

¹if the time dependence of m is written out explicitly, the turnaround radius varies as $r_{\text{ta}}(t) \propto t^{8/9}$

References

- [1] W. Press and P. Schechter, *ApJ* **187**, 425 (1974).
- [2] J. Bond, S. Cole, G. Efstathiou, and N. Kaiser, *ApJ* **379**, 440 (1991).
- [3] C. Lacey and S. Cole, *MNRAS* **262**, 627 (1993).
- [4] J. Peacock and A. Heavens, *MNRAS* **243**, 133 (1990).
- [5] K. Jedamzik, *ApJ* **448**, 1 (1995).
- [6] R. Bower, *MNRAS* **248**, 332 (1991).
- [7] S. White, G. Efstathiou, and C. Frenk, *MNRAS* **262**, 1023 (1993).
- [8] C. Lacey and S. Cole, *MNRAS* **271**, 676 (1994).
- [9] R. Eke, S. Cole, and C. Frenk, *MNRAS* **282**, 263 (1996).
- [10] J. Lee and S. Shandarin, *ApJ* **500**, 14 (1998).
- [11] R. Sheth, H. Mo, and G. Tormen, *MNRAS* **323**, 1 (2001).
- [12] R. Sheth and G. Tormen, *MNRAS* **329**, 61 (2002).
- [13] H. Mo and S. White, *MNRAS* **282**, 347 (1996).
- [14] G. Kaufmann, A. Nusser, and M. Steinmetz, *MNRAS* **286**, 795 (1997).
- [15] R. Sheth, *MNRAS* **300**, 1057 (1998).
- [16] M. Tegmark and P. Peebles, *ApJ* **500**, L79 (1998).
- [17] G. Lemson and G. Kaufmann, *MNRAS* **302**, 111 (1999).
- [18] R. Sheth and G. Tormen, *MNRAS* **308**, 119 (1999).
- [19] U. Seljak, *MNRAS* **318**, 203 (2000).
- [20] A. Cooray and R. Sheth, *Phys.R.* **372**, 1 (2002).
- [21] J. Jing, *ApJ* **503**, L9 (1998).
- [22] D. Hegyi and K. Olive, *ApJ* **303**, 56 (1986).

- [23] M. Fukugita, C. Hogan, and P. Peebles, *ApJ* **503**, 518 (1998).
- [24] D. S. *et al.*, *ApJS* **148**, 175 (2003).
- [25] R. Cyburt, B. Fields, and K. Olive, *PhLB* **567**, 227 (2003).
- [26] F. N. *et al.*, *ApJ* **573**, 157 (2002).
- [27] S. Mathur, D. Weinberg, and X. Chen, *ApJ* **582**, 82 (2003).
- [28] A. Finoguenov, U. Briel, and J. Henry, *A&A* **410**, 777 (2003).
- [29] F. N. *et al.*, *Nature* **433**, 495 (2005).
- [30] U. Hellsten, N. Gnedin, and J. Miralda-Escudé, *ApJ* **509**, 56 (1998).
- [31] R. Perna and A. Loeb, *ApJ* **503**, L135 (1998).
- [32] T. Fang, G. Bryan, and C. Canizares, *ApJ* **564**, 604 (2002).
- [33] R. Cen and J. Ostriker, *ApJ* **514**, 1 (1999).
- [34] R. D. *et al.*, *ApJ* **552**, 473 (2001).
- [35] S. R. Furlanetto and A. Loeb, *ApJ* **611**, 642 (2004).
- [36] H. Kang, D. Ryu, R. Cen, and D. Song, *ApJ* **620**, 21 (2005).
- [37] F. Miniati, T. Jones, H. Kang, and D. Ryu, *ApJ* **562**, 233 (2001).
- [38] F. Miniati, D. Ryu, H. Kang, and T. Jones, *ApJ* **559**, 59 (2001).
- [39] G. Brunetti, G. Setti, L. Feretti, and G. Giovannini, *New Astron.* **6**, 1 (2001).
- [40] R. Berrington and C. Dermer, *ApJ* **594**, 709 (2003).
- [41] S. Gabici and P. Blasi, *ApJ* **583**, 695 (2003).
- [42] G. Brunetti, P. Blasi, R. Cassano, and S. Gabici, *MNRAS* **350**, 1174 (2004).
- [43] H. Kang and T. Jones, *ApJ* **620**, 44 (2005).
- [44] A. Loeb and E. Waxman, *Nature* **405**, 156 (2000).
- [45] T. Totani and T. Kitayama, *ApJ* **545**, 572 (2000).
- [46] F. Miniati, *MNRAS* **337**, 199 (2002).
- [47] C. Scharf and R. Mukherjee, *ApJ* **580**, 154 (2002).
- [48] T. Suzuki and S. Inoue, *ApJ* **573**, 168 (2002).
- [49] T. Totani and S. Inoue, *APh* **17**, 79 (2002).

- [50] S. Gabici and P. Blasi, APh **19**, 679 (2003).
- [51] U. Keshet, E. Waxman, A. Loeb, V. Springel, and L. Hernquist, ApJ **585**, 128 (2003).
- [52] F. Miniati, MNRAS **342**, 1009 (2003).
- [53] O. Reimer, M. Pohl, P. Sreekumar, and J. Mattox, ApJ **588**, 155 (2003).
- [54] S. Gabici and P. Blasi, APh **20**, 579 (2004).
- [55] T. Prodanović and B. Fields, ApJ **616**, L115 (2004).
- [56] T. Prodanović and B. Fields, ApJ **in press** (2005).
- [57] T. K. Suzuki and S. Inoue, PASA **21**, 148 (2004).
- [58] P. Kuo, S. Bowyer, and C.-Y. Hwang, ApJ **618**, 675 (2005).
- [59] E. Bertschinger, ApJS **58**, 39 (185).
- [60] D. Ryu and H. Kang, MNRAS **284**, 416 (1997).
- [61] F. Miniati, D. Ryu, H. Kang, T. Jones, R. Cen, and J. Ostriker, ApJ **542**, 608 (2000).
- [62] E. Bertschinger, ApJS **58**, 1 (1985).
- [63] D. Ryu, H. Kang, E. Hallman, and T. Jones, ApJ **593**, 599 (2003).
- [64] S. Inoue and M. Nagashima (2005).
- [65] S. Chandrasekhar, Rev. Mod. Phys. **15**, 2 (1943).
- [66] P.J.E. Peebles, ApJ **284**, 439 (1984).
- [67] G. Lemaître, Compt. Rend. **196**, 903 (1933).
- [68] G. Lemaître, Compt. Rend. **196**, 1085 (1933).
- [69] O. Lahav, P. Lilje, J. Primack, and M. Rees, MNRAS **251**, 128 (1991).
- [70] P. Peebles, *The Large Scale Structure of the Universe* (Princeton Univ. Press, Princeton, N.J., 1980).
- [71] F. Bernardeau, A&A **291**, 697 (1994).
- [72] J. Bardeen, J. Bond, N. Kaiser, and A. Szalay, ApJ **304**, 15 (1986).
- [73] H. Mo and S. White, MNRAS **336**, 112 (2002).
- [74] L. Landau and E. Lifshitz, *Fluid Mechanics* (Butterworth-Heinemann, Boston, 1999).
- [75] V. Pavlidou and B. Fields, PhysRevD **71**, 043510 (2005).

Author's Biography

Vasiliki Pavlidou was born in Thessaloniki, Greece in 1977. She received her B.S. in Physics from the Aristotle University of Thessaloniki in 1999, and her M.S. in Astronomy from the University of Illinois in 2001. She is married to Kostas Tassis, and they have had several house plants, three of which are currently alive.